

Anomalies in spectrum
of two-dimensional Hubbard model:
Exact Diagonalization
and Dual Fermion study

Dissertation
zur Erlangung des Doktorgrades
an der Fakultät für Mathematik, Informatik und Naturwissenschaften
des Fachbereichs Physik
der Universität Hamburg

vorgelegt von
Mikhail Danilov

Hamburg
2021

Weitere Identifier: urn:nbn:de:gbv:18-ediss-95611

Gutachter der Dissertation: Prof. Dr. Alexander I. Lichtenstein
Prof. Dr. Michael Potthoff

Zusammensetzung der
Prüfungskommission: Prof. Dr. Alexander I. Lichtenstein
Prof. Dr. Michael Potthoff
Prof. Dr. Daniela Pfannkuche
Dr. Frank Lechermann
Dr. Jens Wiebe

Vorsitzende der
Prüfungskommission: Prof. Dr. Daniela Pfannkuche

Datum der Disputation: 23.09.2021

Vorsitzender Fach-
Promotionsausschusses Physik: Prof. Dr. Wolfgang Hansen

Leiter des Fachbereichs Physik: Prof. Dr. Günter H.W. Sigl

Dekan der Fakultät MIN: Prof. Dr. Heinrich Graener

Zusammenfassung

Diese Dissertation stellt zwei robuste numerische Ansätze vor, Exakte Diagonalisierung (ED) und Dual Fermion (DF) Ansatz, zur Modellierung von Systemen mit starken Elektronenkorrelationen. Exakte Diagonalisierung, die den Vorteil hat, Werte direkt aus den niedrigen Ergiezzustande des Hamiltonian zu berechnen und reellen Frequenzen für dynamische Werte zu verwenden, wird mit dem Dual Fermion kombiniert, der durchs Erstellen einer diagrammatischen Expansion um die Ergebnisse der Exakte Diagonalisierung, ein unendliches System annähern kann.

Der erste Teil der Dissertation erklärt beide Methoden mit ausreichend technischem Detail für ihre effiziente Verwendung. Die Methoden wurden als Open-Source-Software implementiert und für diese Studie verwendet.

Im zweiten Teil wird, der in dem ersten Teil beschriebener, numerischer Werkzeugsatz verwendet, um Varianten von 2×2 Hubbard-Plaquette – das minimale Modell der Hochtemperatur-Supraleitfähigkeit in Materialien auf Kupferoxidbasis – zu studieren, für die experimentelle Ergebnisse deutlich auf das Vorhandensein eines quantenkritischen Punkts um das Lochendotieren von $\delta \approx 0,24$ zeigen, unter denen ein supraleitender Übergang aufgetreten sein kann. Die Eigenschaften dieses Systems wurden für verschiedene Werte der folgenden Parameter berechnet: Loch-Dotierung δ , Coulomb-Wechselwirkung U und Nächste-Nachbarn-Hüpfen t' .

Exakte Diagonalisierung wird auch allein in dem Hubbard-Modell mit 4×4 Gitterplätze verwendet, das aus 4 2×2 Plaquettes besteht, um seine elektronische Struktur, die ein Pseudogap in einigen Regimen aufweist, Loch-Loch-Bindungsenergie, die einen Minimum mit Bezug auf U zeigt, welche sich mit t' verschiebt und vergrößert, und verschiedene Korrelatoren, die die Unterdrückung des Antiferromagnetismus durch t' zeigen, zu berechnen. All das deutet auf das Vorhandensein eines quantenkritischen Punkts. Innerhalb des neuartigen komplexen Netzwerk-Theory-Ansatzes wird die von ED berechnete Dichtematrix zur Berechnung der Werte der Quantenverschränkung verwendet, deren Abhängigkeit von δ , U , t' , ein Feature aufweist, das das Vorhandensein des kritischen Punkts weiter unterstützt.

Abstract

This thesis presents two robust numerical approaches to modelling the properties of systems with strong electron-electron correlation. The Exact Diagonalization method (ED), whose advantages are the ability to calculate quantities directly from low-energy states of the Hamiltonian and to use real frequencies for dynamical quantities, is combined with the Dual Fermion approach (DF) that by constructing a diagrammatic expansion around the results of Exact Diagonalization is able to approximate an infinite system.

The first part of the thesis explains both methods with enough technical detail for their efficient use. The methods were implemented as open-source software packages and used for this study.

In the second part, the numerical toolchain that was described in the first part is used to study the variants of 2×2 Hubbard plaquette – the minimal model of high-temperature superconductivity in copper oxide based materials, for which experimental findings clearly point to the existence of a quantum critical point around hole doping of $\delta \approx 0.24$, below which a superconducting transition may occur. The properties of this system were calculated for different values of the following parameters: hole doping δ , Coulomb interaction U and next nearest neighbour hopping t' .

Exact Diagonalization is also used alone on the 4×4 -site Hubbard model that is made up of 4 2×2 plaquettes to calculate its electronic structure that experiences a pseudogap in some regimes, hole-hole binding energy that has a minimum with relation to U which shifts and scales with t' , and different correlators that show the suppression of antiferromagnetism by t' – all of which indicate the presence of a quantum critical point. Within the novel Complex Network Theory approach, the density matrix calculated by ED is used to calculate quantum entanglement measures, whose dependence on δ , U , t' has a feature that further supports the existence of the critical point.

Contents

Introduction	1
I Methods	5
1 Exact Diagonalization	7
1.1 Hamiltonian	8
1.2 Arnoldi diagonalization	13
1.3 Dynamical properties	14
1.3.1 Green's function	14
1.3.2 Susceptibilities	17
1.3.3 Lanczos algorithm	19
1.3.4 Other properties	21
1.4 Static correlators	21
1.5 Solution of large Hubbard clusters	23
1.6 Implementation: EDLib	25
1.6.1 Storage formats	25
Spin-resolved Hamiltonian storage format	25
Signs-only Compressed Row storage format	27
1.6.2 Program description	30
Class diagram	30
Library usage	31
Observables	31
Description of the input data	32
1.6.3 Examples	32
Finite Hubbard cluster diagonalization	33
The Co adatom on the Pt(111) surface	34
1.6.4 Extension	35
2 Cluster Dual Fermion	39
2.1 Dual Fermion approach with a general reference system	39
2.2 Perturbation in dual space	45

2.3	Exact relation for Green's function	46
2.4	Plaquette periodization	48
2.5	Implementation: Multiorbital DF	49
II	Study of the two-dimensional Hubbard model	51
3	Exact Diagonalization of 2×2 Hubbard plaquette	53
3.1	Phase diagrams	55
3.2	Dynamical averages in momentum space	56
4	Dual Fermion study of 2×2 plaquette	59
4.1	Results for plaquette dual scheme	62
4.1.1	Vertex and Bethe–Salpeter Equation	64
4.2	Results of the Multiorbital DF solver	67
5	Exact Diagonalization of 4×4 Hubbard cluster	75
5.1	Phase diagrams	77
5.2	Pairing mechanism in real space. Comparison with Dual Fermion . .	78
5.3	Spectral information	79
5.4	Ground state properties	80
5.5	Hole-hole correlation	83
5.6	Dynamical averages in momentum space	92
6	Complex network theory study of 4×4 Hubbard cluster	99
6.1	Results	102
6.2	Discussion	106
6.3	Additional results	106
	Summary and outlook	117
	Bibliography	121
	List of Publications	139
	Acknowledgments	143

Introduction

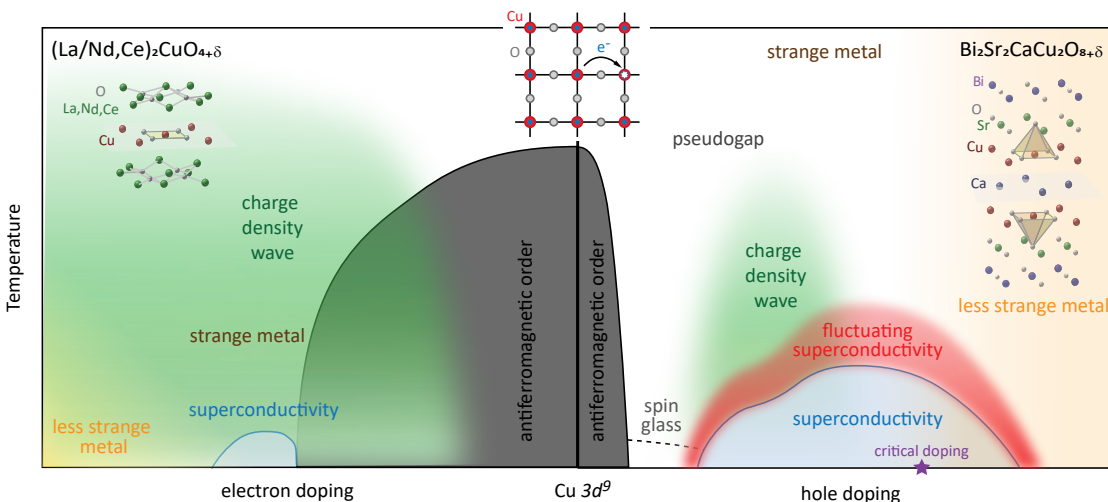


FIGURE 1: Schematic temperature-doping phase diagram of electron and hole-doped cuprate superconductors. Top left inset: lattice arrangement for one unit-cell of electron-doped cuprate $(\text{La/Nd,Ce})_2\text{CuO}_4$ ($T_c^{\text{max}} \sim 30$ K). Top right inset: lattice arrangement for one half unit-cell of $\text{Bi}_2\text{Sr}_2\text{CaCu}_2\text{O}_8$ ($T_c^{\text{max}} \sim 96$ K). Middle inset: top view of the CuO_2^{n-} plane in real space. Red circle - copper, grey circle - oxygen, blue circle - electron, white circle - doped hole. Purple star - the critical doping that separates two different metallic regimes. Figure taken from [118].

High-temperature superconductivity (HTSC) in cuprates still remains a puzzling phenomenon since the 1986 discovery by Bednorz and Muller of superconductivity with T_c an order of magnitude higher than of conventional superconductors, in a material that at room temperature is a good insulator. [18]. The well-established Bardeen-Cooper-Schriffer (BCS) [17] theory of superconductivity does not seem to be able to explain the origin of this effect. Despite a lot of effort having been made by the scientific community to understand the physics behind HTSC, the key ingredients are still to be found. The complex variety of CuO_2 -based material behaviours at different dopings and temperatures was summarized by [118] as a phase diagram (Fig. 1). Experimental studies of those complex materials have many problems due

to other effects such as phonons, antiferromagnetism etc. competing with superconductivity in the interesting regimes. While the many theories that have been proposed can not meet an agreement due to the lack of reliable calculation tools, with many methods being unable to include strong electron-electron correlations that are present in copper oxide based materials.

One of the possible explanations of HTSC proposed by Anderson [9] is that HTSC can occur in a Mott insulator doped with small number of charge carriers. The mechanism of this transition and its links to strongly correlated electrons are still an open question.

The two-dimensional Hubbard model, proposed in 1964 [60], can be used for strongly correlated materials and is considered the simplest model of cuprates. Despite its simplicity, behaviour of this model has only been well determined in the one- [79] and infinite-dimensional [94] limits, finite dimension that corresponds to real materials still having not reached consensus, therefore it is not clear whether Hubbard model can explain the mechanism of HTSC. On the other hand, the two-dimensional Hubbard model seems to reproduce the various stripe-type orders occurring near the superconducting phase in cuprate superconductors [125, 39], transition metal oxides [62] and organic conductors [123, 69, 58, 95, 23, 32].

Dynamical mean-field theory [42, 94] is a self-consistent mapping of the lattice to an impurity site connected with a bath of non-interacting electrons, which becomes exact in the limit of infinite dimensions. It can successfully treat both high and low energy physics, capturing both the Mott insulator and metal states, and has provided results that agree well with experiments on numerous 3-dimensional compounds.[72] However, it breaks down in superconducting cuprates due to being a purely local theory which is unable to reproduce momentum dependency of properties captured in ARPES experiments [30].

The Cluster DMFT (or Cellular DMFT) method addresses that problem by replacing the single-site impurity with a cluster, introducing short-ranged spatial correlations and allowing for momentum dependency and spatially-dependent effects such as antiferromagnetism (AF) and d-wave superconductivity (d-SC). One of the possibilities for the cluster impurity is the 2×2 Hubbard plaquette, which has been studied in [78, 86], showing AF, pseudogap and superconductivity. Some studies ([84, 85, 116]) suggest using larger clusters, however in that case it is not yet known if Mott insulating regime is correct for such system.

It is possible to employ CDMFT with a variety solution schemes, and in this thesis it will be used with Exact Diagonalization and Dual Fermion methods. The advantage of those methods is that they obtain results on real frequencies, which are easier to interpret, and Exact Diagonalization extracts unbiased information from the Hamiltonian of the system. However, the exponential growth of the problem

size with the number of sites restricts our implementation of the Exact Diagonalization method to a maximum of 16 sites on common hardware. Dual Fermion approach can improve the situation by performing a diagrammatic expansion of a larger momentum-space system in terms of Exact Diagonalization results.

Angle-resolved photoemission spectroscopy (ARPES) is an experimental technique that measures spectral density $A(\mathbf{k}, \omega)$ of a material by probing the electronic structure in momentum space by means of photoelectric effect. It has been used extensively to study superconducting, metallic, pseudogap and other electronic properties of copper oxide based materials, for example $Bi_2Sr_2CaCu_2O_8$ visualized in [118] (Fig. 2, 3). The results of this method can be directly compared to the results of theoretical modelling, which makes it an important source of experimental checks.

The goal of this thesis is to implement an efficient numerical scheme that would facilitate the study of Hubbard model in the context of modeling HTSC in cuprates, with the focus on the critical hole-doped model of CuO_2 -based superconductor that is near the separation of two metallic regimes (marked by a purple star on the phase diagram Fig. 1). Among other properties $A(\mathbf{k}, \omega)$ will be calculated, which could later be useful for experimental verification of the modelling.

The thesis has the following structure.

Part I presents the methods that were used in the study, along with useful implementation detail. **Chapter 1** discusses the Exact Diagonalization method, which calculates properties of the model from the low-energy states of its Hamiltonian, and introduces a means of increasing the model size accessible to the study. **Chapter 2** explains the Dual Fermion approach, which applies a diagrammatic perturbation expansion to a system of auxiliary fermions that represents the original model.

Part II examines properties of the Hubbard model for possible indicators of high-temperature superconductivity. **Chapter 3** introduces the 2×2 Hubbard plaquette, the basic building block of the systems studied in this work. **Chapter 4** studies by means of the Dual Fermion method a system of 2×2 plaquettes connected in the momentum space. **Chapter 5** calculates properties of the 4×4 Hubbard cluster constructed from 4 2×2 plaquettes with the Exact Diagonalization method. **Chapter 6** presents the complex network theory approach based on Exact Diagonalization data, which can be used to search for the critical point in the 4×4 cluster.

A summary of the results and the outlook on further research conclude the thesis.

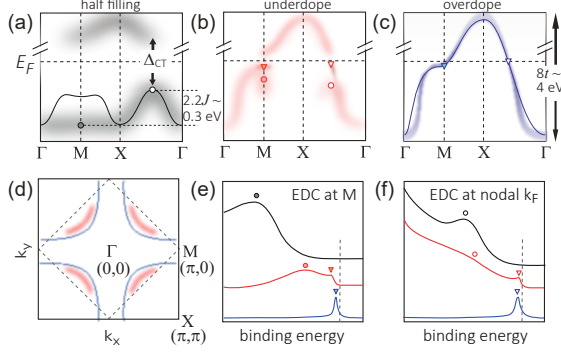


FIGURE 2: Schematic evolution of the electronic structure in hole-doped cuprate. (a)-(c) Idealized normal state spectral function evolution with hole-doping along high symmetry directions. Solid black line - t - J model band calculation at half filling. Solid blue line - tight binding band calculation at heavy hole doping. (d) Fermi surface in underdoped (red) and overdoped (blue) cuprates. The dashed diamond is the AFM zone boundary. (e) $(\pi,0)$ and (f) $(\pi/2,\pi/2)$ or nodal k_F EDC evolution with hole doping. Circles - high energy spectral feature associated with Mott physics. Triangles - low energy spectral features that are, or will evolve into, quasiparticles. Black - half filling. Red - underdoped. Blue - overdoped. Note that the definition of X and M differs here from the $X = (\pi, 0)$, $M = (\pi, \pi)$ used in the rest of the figures in the thesis. Figure taken from [118].

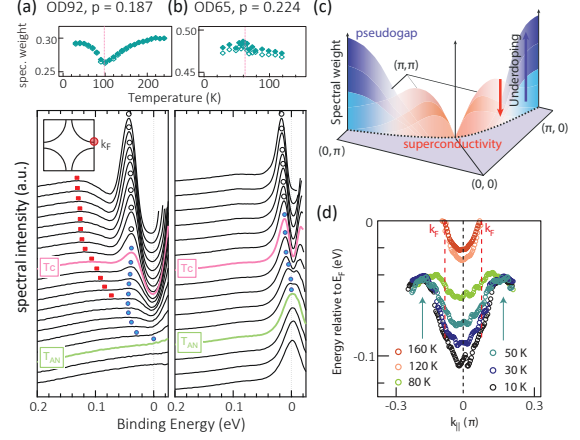


FIGURE 3: Spectral characters of the pseudogap (red squares) and its relation to superconducting quasiparticle peaks (blue dots). Temperature dependent, Fermi-function divided antinodal spectra for (a) near optimally doped (b) heavily overdoped $\text{Bi}_2\text{Sr}_2\text{CaCu}_2\text{O}_8$. T_{AN} is the gap closing temperature at the antinode. Adapted from [55]. Top panels show the spectral weight evolution within $[0,70]$ meV binding energy with temperature, normalized by total spectral weight over $[0,250]$ meV binding energy. (c) Momentum and doping dependent spectral weight competition between superconducting coherent peak (red) and pseudogap (blue) in $\text{Bi}_2\text{Sr}_2\text{CuO}_6$. Graduated shades correspond to the marked direction of doping. Adapted from [71]. (d) Particle-hole asymmetry for the pseudogap in optimally doped $\text{Bi}_2\text{Sr}_2\text{CuO}_6$. Adapted from [54]. Figure taken from [118].

Part I

Methods

Chapter 1

Exact Diagonalization

Exact Diagonalization (ED), also referred to as *Lanczos method*, is one of the most straightforward approaches to numerically solving models of strongly correlated particles, such as the Hubbard model[60] and the Anderson impurity model[8], for different geometries of lattice cluster or with different forms of the on-site Coulomb matrix [63, 89], which are inherently many-body quantum systems. Because analytical methods of solving such systems do not always exist, ED has often been employed to obtain static and dynamical properties of various models for: searching for novel phenomena specific for systems with strong electronic correlations, checking of theoretical and analytical results, use as a reference for more advanced numerical methods.

In its essence, Exact Diagonalization method is the solving of the Schrödinger's equation for the model $H|n\rangle = E_n|n\rangle$, by representing its Hamiltonian as a matrix, diagonalizing it and calculating the properties of the system from the results. Despite its limitations it is popular due its good applicability to all families of correlated electron models, although with a small cluster size that would be further limited if the sites' number of freedoms is increased. The method is flexible and obtains exact properties of those models, as opposed to their crude approximations. ED is typically used to detect spin, charge or orbital order tendencies in the small cluster, before using other methods or mean-field approximations to solve a larger system. It can also be used to confirm ideas, such as variational states, or to benchmark other computational methods. An important advantage of the scheme is that it can also obtain spectral functions and real-time evolution of states, the latter being used in studies of non-equilibrium systems. [2] Another advantage of the Exact Diagonalization method is that it provides a natural way to calculate real-frequency correlation functions such as one- and two-particle Green's functions at finite temperatures.

The approach that will be discussed here is called Finite Temperature Lanczos Method (FTLM). It is performed in two steps.

1. Low-energy states $|n\rangle$, E_n of the Hamiltonian are extracted.

2. The states are used to calculate quantities: some directly from the eigenvectors, others by applying another variant of Lanczos algorithm to the vector and the Hamiltonian.

The following input data is used:

- Hamiltonian parameters for Hubbard model: Coulomb interaction U_i , hopping integrals t_{ij} , chemical potential μ or for Anderson model: impurity and bath energy levels ε_i ε_p , hopping between impurity and bath states V_{ip} , matrix element of Coulomb interaction U_{ijkl} .
- Inverse temperature $\beta = 1/(k_B T)$ (k_B is chosen = 1 here) and the cutoff value of $e^{\beta(E_0 - E_n)}$, below which contributions of eigenstates are not calculated.
- Optionally: fixed total numbers of electrons (N_\uparrow, N_\downarrow) to consider, the site indices for which to evaluate dynamical averages to evaluate reduced density matrix etc.

1.1 Hamiltonian

The *Hamiltonian* H is the operator of the system's total energy. The solutions of Schrödinger's equation

$$\mathcal{H} |n\rangle = E_n |n\rangle, \quad (1.1)$$

are pairs of eigenvalues E_n and eigenvectors $|n\rangle$ (together referred to as *eigenstates*) of \mathcal{H} , which characterize the system's energy levels and corresponding superpositions of basis states.

Within the ED approach, eigenstates are obtained by diagonalizing the Hamiltonian matrix in second quantization basis, that is a Hilbert space of occupation number vectors, also called

$$|n_{1\uparrow}, \dots, n_{N_s\uparrow} |n_{1\downarrow}, \dots, n_{N_s\downarrow}\rangle, \quad (1.2)$$

where n_i is number of particles on i-th site, N_s is number of sites. The vectors are defined as

$$|n_1, n_2, \dots\rangle = \prod_i (c_i^+)^{n_i} |0\rangle, \quad (1.3)$$

and the creation and annihilation operators

$$c_i^+ |n_1, \dots, n_i, \dots\rangle = (-1)^{\sum_{j=1}^{i-1} n_j} |n_1, \dots, (n_i + 1), \dots\rangle. \quad (1.4)$$

The Hamiltonian of many quantum electron models can be expressed as the sum of “local” term \mathcal{H}_{loc} , which is on the diagonal of the Hamiltonian matrix, and “hopping” term \mathcal{H}_{hop} , which is off-diagonal (the rest of the matrix):

$$\mathcal{H} = \mathcal{H}_{\text{loc}} + \mathcal{H}_{\text{hop}}. \quad (1.5)$$

For example, in Hubbard model

$$\begin{aligned} \mathcal{H}_{\text{loc}} &= \sum_i U_i n_{i\uparrow} n_{i\downarrow} - \mu \sum_{is} n_{is}, \\ \mathcal{H}_{\text{hop}} &= \sum_{i \neq j, s} t_{ij} c_{is}^+ c_{js}. \end{aligned} \quad (1.6)$$

where U_i is Coulomb interaction on site i , t_{ij} is the hopping integral between sites i and j , μ is chemical potential, $c_{is}^{(+)}$ and $n_{is} = c_{is}^+ c_{is}$ are, correspondingly, electron annihilation (creation) and number of particles operators on site i with the spin s .

Another model often used with Exact Diagonalization is the Anderson model with multi-orbital impurity:

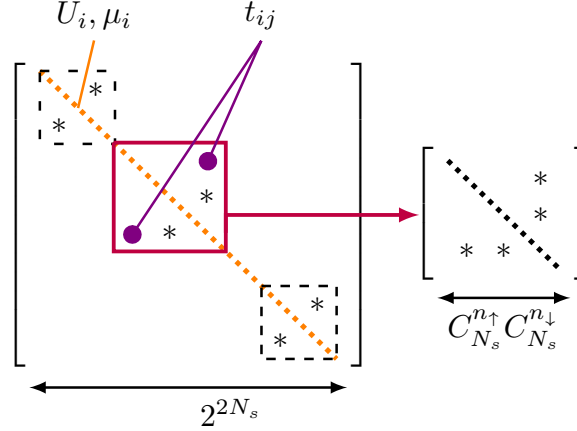
$$\begin{aligned} \mathcal{H}_{\text{loc}} &= \frac{1}{2} \sum_{\substack{ijkl \\ ss'}} U_{ijkl} d_{is}^+ d_{js'}^+ d_{ls'} d_{ks}, \\ \mathcal{H}_{\text{hop}} &= \sum_{ps} \varepsilon_p c_{ps}^+ c_{ps} + \sum_{is} (\varepsilon_i - \mu) n_{is} + \sum_{ips} (V_{ip} d_{is}^+ c_{ps} + H.c.), \end{aligned} \quad (1.7)$$

where $d_{is}^{(+)}$ and $c_{ps}^{(+)}$ are the annihilation (creation) operators for electrons on impurity sites and bath states, ε_i and ε_p are the energy levels of impurity and bath states, V_{ip} is hopping between impurity and bath states, U_{ijkl} is the matrix element of Coulomb interaction and the impurity orbital index i (j, k, l) runs over the impurity sites. Depending on the problem being solved, the bath can correspond to either an effective Weiss field (DMFT) or, for instance, metallic surface states (adatom on a substrate). Since the general Coulomb interaction contains non density-density terms the local part of Hamiltonian matrix is no longer diagonal and needs additional effort.

The Hilbert space dimension N_{st} of the Hamiltonian matrix is

$$N_{\text{st}} = K^{N_s}, \quad (1.8)$$

where N is the number of sites and K is the number of possible states for each site. For Hubbard and Anderson models $K=4$, because each site can be in 4 states: empty, occupied by one electron with the spin up, by one electron with the spin down and occupied by two electrons of different spins. By using commutation relations for

FIGURE 1.1: Block structure of the S^z -symmetric model Hamiltonian matrix.

fermions $\{c_i, c_j\} = 0$ and $\{c_i^+, c_j\} = \delta_{ij}$ it can be shown that

$$[\mathcal{H}, N] = 0$$

where $N = \sum_{is} n_{is}$ is total number of particles and

$$[\mathcal{H}, S_z] = 0,$$

where $S_z = \frac{1}{2} \sum_i (n_{i\uparrow} - n_{i\downarrow})$ is total spin of the system, which means quantities $\langle N \rangle$ and $\langle S_z \rangle$ are conserved.

Hamiltonian in the occupation number representation is thus block-diagonal, which allows for separate treatment of $(N_s + 1)^2$ blocks, so called *sectors* (Fig. 1.1) with total number of particles per spin $(N_{\uparrow}, N_{\downarrow})$, whose Hilbert space has the dimension

$$N_{\text{st.}(N_{\uparrow}, N_{\downarrow})} = C_{N_s}^{N_{\uparrow}} C_{N_s}^{N_{\downarrow}}, \quad (1.9)$$

where $C_n^k = \frac{n!}{k!(n-k)!}$ is the number of k -combinations out of n elements.

Basis states of a Hamiltonian sector $(N_{\uparrow}, N_{\downarrow})$ are pairs of a N_{\uparrow} - and a N_{\downarrow} -combination out of N_s , which are generated by the algorithm (Alg. 1) explained in [80]. An example of basis vectors is shown on Fig.1.2.

The representation that has been described can be illustrated on a two-site Hubbard model, whose Hamiltonian and all Hilbert space vectors $|n_{1\uparrow}, n_{2\uparrow} | n_{1\downarrow}, n_{2\downarrow} \rangle$ are shown on Fig. 1.3, where one can see a block-diagonal structure.

Hamiltonian sectors for models with more sites become large but very sparse because of most $t_{ij} c_{is}^+ c_{js}$ being zero. Specialized sparse matrix formats are used to store them efficiently, such as Compressed Row Storage (CRS).

```

First k-combination:
for  $i$  from 1 to  $k$  do
  |  $A_i \leftarrow k$ ;
end
 $p \leftarrow k$ ;
while  $p \geq 1$  do
  | print  $A_1, \dots, A_k$ ;
  | if  $A_k = n$  then
  | |  $p \leftarrow p - 1$ ;
  | end
  | else
  | |  $p \leftarrow k$ ;
  | end
  | if  $p \geq 1$  then
  | | for  $i$  from  $k$  to  $p$  do
  | | |  $A_i \leftarrow A_p + i - p + 1$ ;
  | | | end
  | end
end

```

Algorithm 1: k -combinations of n

```

1, 2, 3, 4 : |1, 1, 1, 1, 0, 0⟩,
1, 2, 3, 5 : |1, 1, 1, 0, 1, 0⟩,
1, 2, 3, 6 : |1, 1, 1, 0, 0, 1⟩,
1, 2, 4, 5 : |1, 1, 0, 1, 1, 0⟩,
1, 2, 4, 6 : |1, 1, 0, 1, 0, 1⟩,
1, 2, 5, 6 : |1, 1, 0, 0, 1, 1⟩,
1, 3, 4, 5 : |1, 0, 1, 1, 1, 0⟩,
1, 3, 4, 6 : |1, 0, 1, 1, 0, 1⟩,
1, 3, 5, 6 : |1, 0, 1, 0, 1, 1⟩,
1, 4, 5, 6 : |1, 0, 0, 1, 1, 1⟩,
2, 3, 4, 5 : |0, 1, 1, 1, 1, 0⟩,
2, 3, 4, 6 : |0, 1, 1, 1, 0, 1⟩,
2, 3, 5, 6 : |0, 1, 1, 0, 1, 1⟩,
2, 4, 5, 6 : |0, 1, 0, 1, 1, 1⟩,
3, 4, 5, 6 : |0, 0, 1, 1, 1, 1⟩.

```

FIGURE 1.2: Example basis states (only the spin up part shown for simplicity) of a Hubbard a model $N_s = 6$ Hamiltonian sector $N_\uparrow = 4$, generated by Alg. 1.

Compressed Row Storage[21], also known as Compressed Storage Row (CSR), is the basic format that does not make any assumptions about structure of the matrix and is suitable for any Hamiltonian. It consists of three arrays, for example a $M \times M$ -size matrix a_{ij} with N non-zero elements is stored as ¹

- `val` of length N storing non-zero elements of a_{ij} continuously, row by row.
- `col_ind` of length N contains column indices j of their corresponding matrix elements.
- `row_ptr` of length $M+1$ stores index in `val` and `col_ind` of the first element of each row. For convenience its last element is N , i.e. the index one place past the end of `val` and `col_ind`.

An example matrix stored in CRS format is shown on Fig. 1.4.

The matrix-vector multiplication with CRS is ideally suited for parallelization, because each thread can store a horizontal strip of the Hamiltonian and multiply the

¹Zero-based indices are used here.

which are two much smaller sparse matrices of dimensions

$$N_{st.N_{\uparrow(\downarrow)}} = C_{N_s}^{N_{\uparrow(\downarrow)}}. \quad (1.11)$$

1.2 Arnoldi diagonalization

The first step of Exact Diagonalization solution is to extract the eigenstates of the Hamiltonian matrix. At finite temperature T only a very small subset of those is required to calculate the system's properties with good precision, because a state's contribution to averages is proportional to $e^{\beta(E_0 - E_n)}$ (e.g. in Green's function Eq. 1.18, 1.19), where $\beta \propto T^{-1}$ is the inverse temperature, E_0 is the ground state energy and E_n is the state's energy, which decreases rather quickly with $E_0 - E_n$.

Krylov subspace methods, such as Lanczos or Arnoldi iteration, which work by projecting the Hamiltonian \mathcal{H} onto its Krylov subspace

$$\mathcal{K}^m(\mathcal{H}, v) = \{\mathcal{H}^m v, \dots, \mathcal{H}^2 v, \mathcal{H} v, v\}.$$

They are especially well-suited for such partial diagonalization or large sparse matrices, because the matrix-vector product procedure used to construct the subspace can be implemented efficiently with parallel computation.

The basic Arnoldi algorithm[14, 109] is shown here as a simplified example. First, the initial vector $|v_0\rangle$ should be chosen, with the norm $\langle v_0 | v_0 \rangle = 1$. New vectors are then produced by the iterative procedure Alg. 2. where N_{cv} is the number of Krylov space vectors.

```

for  $i$  from 1 to  $N_{cv} - 1$  do
   $|v_i\rangle \leftarrow \mathcal{H} |v_{i-1}\rangle;$ 
  for  $j$  from 0 to  $i - 1$  do
     $h_{j,i-1} \leftarrow \langle v_j | v_i \rangle;$ 
     $|v_i\rangle \leftarrow |v_i\rangle - h_{j,i-1} |v_j\rangle;$ 
  end
   $h_{i,i-1} \leftarrow \langle v_i | v_i \rangle;$ 
   $|v_i\rangle \leftarrow |v_i\rangle / h_{i,i-1};$ 
  if  $|v_i\rangle = 0$  then
    | converged, exit
  end
end

```

Algorithm 2: Arnoldi algorithm for m iterations

The resulting set of vectors is the Krylov subspace basis, which ideally should be orthogonal, but in numerical computation new vectors lose orthogonality. The Arnoldi method tries to preserve it by orthogonalizing each new vector against all previous vectors using modified Gram-Schmidt process, unlike Lanczos method (Section 1.3) which only orthogonalizes against the two previous vectors, but additional techniques, such as implicit restart[14, 77, 87], are still required for this task. For example, the ARPACK-NG[11] library’s implementation of implicitly restarted Arnoldi method can be used.

1.3 Dynamical properties

1.3.1 Green’s function

The *Green’s function* of the system is a propagator – an object containing information about the system’s evolution and physical behaviour. It is defined as the following average [1]:

$$G_{ij}(\tau) = -\langle T_\tau(c_i(\tau)c_j^\dagger(0)) \rangle,$$

where τ is imaginary time, $c_i(\tau)$, $c_j^\dagger(\tau)$ are annihilation and creation operators in Heisenberg representation, which act on sites i and j and T_τ is time-ordering operator, averaging “ $\langle \rangle$ ” is over grand canonical ensemble. Exact Diagonalization calculates dynamical averages, such as Green’s function, using Lehmann representation.

For a system represented by Hamiltonian \mathcal{H} with Schrödinger’s equation

$$\mathcal{H} |n\rangle = E_n |n\rangle,$$

the average of an operator A , such as $c_i(\tau)c_j^\dagger(0)$ of the Green’s function, can be written in terms of the solutions of E_n , $|n\rangle$ of Eq. 1.3.1:

$$\langle A \rangle = \text{Tr}(\rho A) = \frac{1}{Z} \text{Tr}(e^{-\beta\mathcal{H}} A) = \frac{1}{Z} \sum_n \langle n | A | n \rangle e^{-\beta E_n},$$

with partition function $Z = \text{Tr}(e^{-\beta\mathcal{H}})$ and density matrix $\rho = \frac{1}{Z} e^{-\beta\mathcal{H}}$ and inverse temperature β .

The Green’s function can then be evaluated in these terms [83]:

$$G_{ij}(\tau) = -\frac{1}{Z} \text{Tr} [e^{-\beta\mathcal{H}} c_i(\tau) c_j^\dagger(0)], \quad (1.12)$$

$$A(\tau) = e^{\mathcal{H}\tau} A e^{-\mathcal{H}\tau},$$

we can express Green's function in terms of the Hamiltonian's eigenpairs:

$$G_{ij}(\tau) = -\frac{1}{Z} \sum_{m,n} e^{-\beta E_n} e^{-\tau(E_n - E_m)} \langle n | c_i | m \rangle \langle m | c_j^\dagger | n \rangle. \quad (1.13)$$

To get the spectral representation it is more practical to evaluate Green's function on the frequency domain, to which we can transform the equation with the Fourier transform:

$$\begin{aligned} G_{ij}(z) &= \int_0^\beta d\tau G_{ij}(\tau) e^{z\tau}. \\ G_{ij}(z) &= -\frac{1}{Z} \sum_{m,n} \langle n | c_i | m \rangle \langle m | c_j^\dagger | n \rangle e^{-\beta E_n} \int_0^\beta d\tau e^{\tau(z + E_n - E_m)} \\ &= -\frac{1}{Z} \sum_{m,n} \langle n | c_i | m \rangle \langle m | c_j^\dagger | n \rangle e^{-\beta E_n} \frac{e^{\beta z} e^{\beta(E_n - E_m)} - 1}{z + E_n - E_m}, \end{aligned} \quad (1.14)$$

where z are fermionic Matsubara frequencies $z = i\omega_n = i(2n + 1)\pi/\beta$ with $n \in \mathbf{Z}$, then $e^{\beta z} = -1$ and

$$\begin{aligned} G_{ij}(z) &= -\frac{1}{Z} \sum_{m,n} \langle n | c_i | m \rangle \langle m | c_j^\dagger | n \rangle e^{-\beta E_n} \frac{(-1)e^{\beta(E_n - E_m)} - 1}{z + E_n - E_m} \\ &= \frac{1}{Z} \sum_{m,n} \frac{\langle n | c_i | m \rangle \langle m | c_j^\dagger | n \rangle}{z + E_n - E_m} [\exp(-\beta E_n) + \exp(-\beta E_m)]. \end{aligned} \quad (1.15)$$

To evaluate the Green's function with the Lanczos method instead of full diagonalization we have to make the formula use only a subset of all eigenpairs of the Hamiltonian. We will be able to truncate the sum if we replace the two exponents under the sum with one by swapping m and n in one of the terms:

$$G_{ij}(z) = \frac{1}{Z} \sum_{m,n} e^{-\beta E_n} \left[\frac{\langle n | c_i | m \rangle \langle m | c_j^\dagger | n \rangle}{z + E_n - E_m} + \frac{\langle n | c_j^\dagger | m \rangle \langle m | c_i | n \rangle}{z + E_m - E_n} \right] \quad (1.16)$$

Direct evaluation of $\sum_m \frac{|m\rangle\langle m|}{z \pm (E_n - E_m)}$ is not possible in general, since it would require a full set of $|m\rangle$. To numerically evaluate Eq. 1.16 we transform the traces

$$\sum_m \frac{\langle n | c_i | m \rangle \langle m | c_j^\dagger | n \rangle}{z + E_n - E_m} = \langle n | c_i \frac{1}{z + E_n - \mathcal{H}} c_j^\dagger | n \rangle$$

and

$$\sum_m \frac{\langle n | c_j^+ | m \rangle \langle m | c_i | n \rangle}{z + E_m - E_n} = \langle n | c_j^+ \frac{1}{z - E_n + \mathcal{H}} c_i | n \rangle,$$

which can now be approximated by a continued fraction (Eq. 1.32) with a much smaller number of $|m\rangle$.

$$G_{ij}(z) = \frac{1}{Z} \sum_n e^{-\beta E_n} \left[\langle n | c_i \frac{1}{z + E_n - \mathcal{H}} c_j^+ | n \rangle + \langle n | c_j^+ \frac{1}{z - E_n + \mathcal{H}} c_i | n \rangle \right]. \quad (1.17)$$

Finally, we can rewrite the local Green's function ² as

$$G_{ii}(z) = \frac{1}{Z} \sum_n e^{-\beta E_n} \left[\frac{\| |c_i^+ | n \rangle \|^2}{z + E_n - \mathcal{H}} + \frac{\| |c_i | n \rangle \|^2}{z - E_n + \mathcal{H}} \right] \quad (1.18)$$

and non-local Green's function as

$$G_{i \neq j}(z) = \frac{1}{2} \left\{ \frac{1}{Z} \sum_n e^{-\beta E_n} \left[\frac{\| |(c_i^+ + c_j^+) | n \rangle \|^2}{z + E_n - \mathcal{H}} + \frac{\| |(c_i + c_j) | n \rangle \|^2}{z - E_n + \mathcal{H}} \right] - G_{ii} - G_{jj} \right\}, \quad (1.19)$$

which was obtained with the following relations

$$\begin{aligned} \langle n | c_i c_j^+ | n \rangle &= \\ \langle n | ((c_i + c_j) - c_j) ((c_i^+ + c_j^+) - c_i^+) | n \rangle &= \\ \langle n | (c_i + c_j) (c_i^+ + c_j^+) - c_j c_j^+ - c_i c_i^+ - c_j c_i^+ | n \rangle &= \quad , \\ \langle n | (c_i + c_j) (c_i^+ + c_j^+) - c_j c_j^+ - c_i c_i^+ - c_i c_j^+ | n \rangle &= \\ \langle n | (c_i + c_j) (c_i^+ + c_j^+) | n \rangle - \langle n | c_j c_j^+ | n \rangle - \langle n | c_i c_i^+ | n \rangle - \langle n | c_i c_j^+ | n \rangle &= \\ \langle n | c_i c_j^+ | m \rangle &= \frac{1}{2} [\langle n | (c_i + c_j) (c_i^+ + c_j^+) | m \rangle - \langle n | c_j c_j^+ | m \rangle - \langle n | c_i c_i^+ | m \rangle]. \end{aligned}$$

Using Eq. 1.18 and 1.19 with real frequencies $\omega = \omega + i\delta$, we can obtain *density of states (DoS)* $A(\omega)$, alternatively called *spectral function*, which characterizes transitions between energy levels of the system:

$$A(\omega)_{ij} = -\frac{1}{\pi} \Im G_{ij}(\omega). \quad (1.20)$$

²The final expressions can be evaluated for either fermionic Matsubara frequencies $z = i\omega_n = i(2n+1)\pi/\beta$ with $n \in \mathbf{Z}$ or real frequencies $z = \omega + i\delta$, In the latter case a small imaginary shift δ is required to avoid poles of the fraction [83], the usual choice being $\delta = \pi/\beta$.

Additionally in the case of real frequencies, for $i = j$ we can calculate *lesser* and *greater* Green's function by breaking up Eq. 1.18 into contributions of c_i and c_i^+ :

$$\begin{aligned} G_{ii}^<(\omega) &= \frac{1}{Z} \sum_n e^{-\beta E_n} \frac{\|c_i |n\rangle\|^2}{\omega + i\delta - E_n + \mathcal{H}}, \\ G_{ii}^>(\omega) &= \frac{1}{Z} \sum_n e^{-\beta E_n} \frac{\|c_i^+ |n\rangle\|^2}{\omega + i\delta - E_n - \mathcal{H}}, \end{aligned} \quad (1.21)$$

whose corresponding spectral function components can be viewed as the system's *photoemission (PES)* and *inverse photoemission (IPES)* spectra

$$\begin{aligned} A_i^{\text{PES}}(\omega) &= -\frac{1}{\pi} \Im G_{ii}^<(\omega), \\ A_i^{\text{IPES}}(\omega) &= -\frac{1}{\pi} \Im G_{ii}^>(\omega), \end{aligned} \quad (1.22)$$

which characterize transitions that occur when the system emits or absorbs a photon of energy ω .

1.3.2 Susceptibilities

The *spin susceptibility* χ_{S_z} and *charge susceptibility* χ_N describe the system's response to magnetic and electrical fields.

$$\begin{aligned} \chi_{Nij}(\tau) &= -\langle T_\tau(n_i(\tau)n_j(0)) \rangle, \\ \chi_{S_zij}(\tau) &= -\langle T_\tau(s_i(\tau)s_j(0)) \rangle, \end{aligned}$$

where $s_i = \frac{1}{2}(n_{i\uparrow} - n_{i\downarrow})$ is the spin operator.

These observables can be calculated by following the same scheme as Green's function, the main difference being that s_i and n are bosonic operators, as opposed to fermionic c_i of Green's function, the other one is that they do not change the occupation numbers of $|v\rangle$ when acting upon it. Only derivation for χ_N is shown here, because for χ_{S_z} expressions have the same form.

Starting with Eq. 1.14

$$\begin{aligned} \chi_{Nij}(z) &= -\frac{1}{Z} \sum_{m,n} \langle n | n_i | m \rangle \langle m | n_j | n \rangle e^{-\beta E_n} \int_0^\beta d\tau e^{\tau(z+E_n-E_m)} \\ &= -\frac{1}{Z} \sum_{m,n} \langle n | n_i | m \rangle \langle m | n_j | n \rangle e^{-\beta E_n} \frac{e^{\beta z} e^{\beta(E_n-E_m)} - 1}{z + E_n - E_m}, \end{aligned} \quad (1.23)$$

we use bosonic Matsubara frequencies $z = i\omega_n = i2n\pi/\beta$, $n \in \mathbf{Z}$. Then $e^{\beta z} = 1$, and the sign between exponents $\exp(-\beta E_n)$ and $\exp(-\beta E_m)$ will be the opposite of that in Green's function:

$$\begin{aligned}\chi_{Nij}(z) &= -\frac{1}{Z} \sum_{m,n} \langle n | n_i | m \rangle \langle m | n_j | n \rangle e^{-\beta E_n} \frac{(-1)e^{\beta(E_n - E_m)} - 1}{z + E_n - E_m} \\ &= \frac{1}{Z} \sum_{m,n} \frac{\langle n | n_i | m \rangle \langle m | n_j | n \rangle}{z + E_n - E_m} [\exp(-\beta E_n) - \exp(-\beta E_m)].\end{aligned}\quad (1.24)$$

$$\chi_{Nij}(z) = \frac{1}{Z} \sum_n e^{-\beta E_n} \left[\sum_m \frac{\langle n | n_i | m \rangle \langle m | n_j | n \rangle}{z + E_n - E_m} - \frac{\langle n | n_j | m \rangle \langle m | n_i | n \rangle}{z + E_m - E_n} \right]. \quad (1.25)$$

Following the same derivation as for 1.18, local susceptibilities are ³

$$\begin{aligned}\chi_{Nii}(z) &= \frac{1}{Z} \sum_n e^{-\beta E_n} \left[\frac{1}{z + E_n - \mathcal{H}} - \frac{1}{z - E_n + \mathcal{H}} \right] \| |n_i \rangle | n \rangle \|^2, \\ \chi_{S_z ii}(z) &= \frac{1}{Z} \sum_n e^{-\beta E_n} \left[\frac{1}{z + E_n - \mathcal{H}} - \frac{1}{z - E_n + \mathcal{H}} \right] \| |s_i \rangle | n \rangle \|^2,\end{aligned}\quad (1.26)$$

and non-local susceptibilities

$$\begin{aligned}\chi_{Ni \neq j}(z) &= \\ \frac{1}{2} \left\{ \frac{1}{Z} \sum_n e^{-\beta E_n} \left[\frac{1}{z + E_n - \mathcal{H}} - \frac{1}{z - E_n + \mathcal{H}} \right] \| |(n_i + n_j) \rangle | n \rangle \|^2 - \chi_{Nii} - \chi_{Njj} \right\}, \\ \chi_{S_z i \neq j}(z) &= \\ \frac{1}{2} \left\{ \frac{1}{Z} \sum_n e^{-\beta E_n} \left[\frac{1}{z + E_n - \mathcal{H}} - \frac{1}{z - E_n + \mathcal{H}} \right] \| |(s_i + s_j) \rangle | n \rangle \|^2 - \chi_{S_z ii} - \chi_{S_z jj} \right\}.\end{aligned}\quad (1.27)$$

Using the numerical scheme Eq. 1.32 to evaluate Lehmann expression Eq. 1.24 at bosonic Matsubara frequency $iz_0 = 0$ would lead to a division by zero. This energy

³Here z can be either bosonic Matsubara $z = i\omega_n = i2n\pi/\beta$ with $n \in \mathbf{Z}$ or real frequency $z = \omega + i\delta$.

point can be calculated with an alternate method proposed by [90]:

$$\chi(i\omega_0) = \beta\chi(\tau = 0) - \sum_{n=-\infty, n \neq 0}^{\infty} \chi(i\omega_n), \quad (1.28)$$

where $\chi(\tau = 0) = \langle OO \rangle$ is 1 for operator $O = n_i$ and 0 for $O = s_i$, and the infinite sum over all Matsubara frequencies is approximated by sum over the calculated frequencies^{4 5}

$$\begin{aligned} \sum_{n=-\infty, n \neq 0}^{\infty} \chi(i\omega_n) &\approx 2 \sum_{n=1}^{N_\omega} \left(\chi(i\omega_n) - \frac{c_2}{\omega_n^2} - \frac{c_4}{\omega_n^4} \right) + 2 \left(\frac{\beta^2}{24} c_2 + \frac{\beta^4}{1440} c_4 \right), \\ c_2 &= - \frac{\chi(\omega_{N_\omega-1}) \omega_{N_\omega-1}^2 - \chi(\omega_{N_\omega}) \omega_{N_\omega}^2}{\omega_{N_\omega}^2 - \omega_{N_\omega-1}^2}, \\ c_4 &= - \frac{\chi(\omega_{N_\omega}) \omega_{N_\omega}^2 \omega_{N_\omega-1}^2 - \chi(\omega_{N_\omega-1}) \omega_{N_\omega-1}^2 \omega_{N_\omega}^2}{\omega_{N_\omega}^2 - \omega_{N_\omega-1}^2}, \end{aligned} \quad (1.29)$$

where $\frac{\beta^2}{24} c_2 + \frac{\beta^4}{1440} c_4$ is the analytic tail for $n = \pm\infty$. One must check that the number of frequencies N_ω is sufficient for the sum to converge, for example by comparing the tail $\frac{\beta^2}{24} c_2 + \frac{\beta^4}{1440} c_4$ against the value it would have for $(N_\omega - 1)$ frequencies.

1.3.3 Lanczos algorithm

Evaluation of the contribution to a dynamical average of each eigenstate $|n\rangle$

$$\langle v_0 | \frac{1}{z + E_n - \mathcal{H}} | v_0 \rangle \quad (1.30)$$

requires inversion of the Hamiltonian \mathcal{H} , which can be approximated from the projection of \mathcal{H} onto Krylov subspace $\mathcal{K}^m(\mathcal{H}, v)$ with the initial vector $|v_0\rangle$:

$$|v_0\rangle = \frac{a |n\rangle}{\sqrt{\langle n | a^+ a | n \rangle}},$$

where $a = c_i^{(+)}$, n_i or s_i for G_{ii} , χ_{Nii} and $\chi_{S_z ii}$ and $a = (c_i^{(+)} + c_j^{(+)})$, $(n_i + n_j)$ or $(s_i + s_j)$ for $G_{i \neq j}$, $\chi_{Ni \neq j}$ and $\chi_{S_z i \neq j}$, and we take for \mathcal{H} the sector of Hamiltonian corresponding to the result of $a |n\rangle$, for example, a sector with $N \pm 1$ electrons

⁴The “2” in front comes from the summation going only over positive frequencies.

⁵Odd powers of $i\omega_n$ (that would have the coefficients c_1, c_3, \dots) are omitted because they are imaginary and do not contribute to χ , which is real.

neighbouring the one with N electrons of $|n\rangle$ when $a = c_i^{(+)}$ and or same sector when $a = n_i$ and $a = s_i$.

The Krylov subspace is constructed with the Lanczos algorithm[14] Alg. 3, with the number of iterations $N_{cv} \sim 100$ typically being enough for the continued fraction Eq. 1.32 to give accurate results [16, 28].

```

 $|w'_0\rangle \leftarrow \mathcal{H} |v_0\rangle;$ 
 $\alpha_0 \leftarrow \langle w'_0 | v_0\rangle;$ 
 $|w_0\rangle \leftarrow |w'_0\rangle - \alpha_0 |v_0\rangle;$ 
for  $i$  from 1 to  $N_{cv} - 1$  do
   $\beta_i \leftarrow \sqrt{\langle w_{i-1} | w_{i-1}\rangle};$ 
  if  $\beta_i = 0$  then
    | converged, exit
  end
   $|v_j\rangle = |w_{i-1}\rangle / \beta_i;$ 
   $|w'_i\rangle \leftarrow \mathcal{H} |v_i\rangle;$ 
   $\alpha_i \leftarrow \langle w'_i | v_i\rangle;$ 
   $|w_i\rangle \leftarrow |w'_i\rangle - \alpha_i |v_i\rangle - \beta_i |v_{i-1}\rangle;$ 
end

```

Algorithm 3: Lanczos algorithm for N_{cv} iterations

Using the coefficients α and β that make up the tridiagonal matrix

$$K = \begin{bmatrix} \alpha_0 & \beta_1 & 0 & 0 & \dots & 0 \\ \beta_1 & \alpha_1 & \beta_2 & 0 & \dots & 0 \\ 0 & \beta_2 & \alpha_2 & \beta_3 & \dots & 0 \\ 0 & 0 & \beta_3 & \alpha_3 & \dots & 0 \\ \vdots & \vdots & \vdots & \vdots & \ddots & \vdots \\ 0 & 0 & 0 & 0 & \dots & \alpha_{N_{cv}} \end{bmatrix}, \quad (1.31)$$

a continued fraction that approximates the contribution of $|n\rangle$ [42, 98] is computed

$$\langle v_0 | \frac{1}{z + E_n - \mathcal{H}} | v_0 \rangle \approx \frac{1}{z - \alpha_0 - \frac{\beta_1^2}{z - \alpha_1 - \frac{\beta_2^2}{z - \alpha_2 - \dots}}}, \quad (1.32)$$

which is done for each z starting from the last denominator $z - \alpha_{N_{cv}}$, in which $\beta_{N_{cv}+1} = 0$.

1.3.4 Other properties

The *bare (or non-interacting) Green's function* G_0 of the model can be calculated by matrix inversion

$$G_{ij}^0(z) = [t + (z + \mu)I]_{ij}^{-1}, \quad (1.33)$$

where t_{ij} is the hopping matrix and I is the identity matrix. On real frequencies this function characterizes spectrum of the system without electron-electron interactions $A_0(\omega)_i = -\frac{1}{\pi} \Im G_{0i}(\omega)$.

Self-energy Σ , which contains electron-electron correlations, can be calculated from the Dyson equation ⁶

$$\Sigma_{ij}(z) = G_{0ij}^{-1}(z) - G_{ij}^{-1}(z). \quad (1.34)$$

1.4 Static correlators

Static correlators, the averages of operators that have no time dependency, can be computed directly from the wave function $\Psi \approx \sum_n e^{-\beta E_n} |v_n\rangle$, with the following examples.

Number of particles on site i :

$$\langle N_i \rangle = \frac{1}{Z} \sum_n e^{-\beta E_n} \langle v_n | n_{i\uparrow} + n_{i\downarrow} | v_n \rangle. \quad (1.35)$$

Number of particles on site i with the spin σ :

$$\langle N_{i\sigma} \rangle = \frac{1}{Z} \sum_n e^{-\beta E_n} \langle v_n | n_{i\sigma} | v_n \rangle. \quad (1.36)$$

Hole density on site i :

$$\langle N_{ih} \rangle = \frac{1}{Z} \sum_n e^{-\beta E_n} \langle v_n | (1 - n_{i\uparrow})(1 - n_{i\downarrow}) | v_n \rangle. \quad (1.37)$$

Double occupancy on site i :

$$\langle N_{i\uparrow} N_{i\downarrow} \rangle = \frac{1}{Z} \sum_n e^{-\beta E_n} \langle v_n | n_{i\uparrow} n_{i\downarrow} | v_n \rangle. \quad (1.38)$$

⁶For some conventions in which one of $(G^0)^{-1}$ and G^{-1} does not include μ , it has to be respectively added or subtracted from this expression.

Magnetic moment on site i :

$$\langle M_i \rangle = \frac{1}{Z} \sum_n e^{-\beta E_n} \langle v_n | n_{i\uparrow} - n_{i\downarrow} | v_n \rangle. \quad (1.39)$$

Product of number of particles on sites i and j :

$$\langle N_i N_j \rangle = \frac{1}{Z} \sum_n e^{-\beta E_n} \begin{cases} \langle v_n | (n_{i\uparrow} + n_{i\downarrow})(n_{j\uparrow} + n_{j\downarrow}) | v_n \rangle, & i \neq j, \\ \langle v_n | (n_{i\uparrow} + n_{i\downarrow}) | v_n \rangle, & i = j, \end{cases} \quad (1.40)$$

Product of hole density on sites i and j :

$$\langle N_{ih} N_{jh} \rangle = \frac{1}{Z} \sum_n e^{-\beta E_n} \begin{cases} \langle v_n | (1 - n_{i\uparrow})(1 - n_{i\downarrow})(1 - n_{j\uparrow})(1 - n_{j\downarrow}) | v_n \rangle, & i \neq j, \\ \langle v_n | (1 - n_{i\uparrow} - n_{i\downarrow} + n_{j\uparrow} n_{j\downarrow}) | v_n \rangle, & i = j, \end{cases} \quad (1.41)$$

Product of magnetic moments on sites i and j :

$$\langle M_i M_j \rangle = \frac{1}{Z} \sum_n e^{-\beta E_n} \langle v_n | (n_{i\uparrow} - n_{i\downarrow})(n_{j\uparrow} - n_{j\downarrow}) | v_n \rangle. \quad (1.42)$$

Product of number of particles with opposite spins on sites i and j :

$$\langle N_{i\uparrow} N_{j\downarrow} \rangle = \frac{1}{Z} \sum_n e^{-\beta E_n} \langle v_n | n_{i\uparrow} n_{j\downarrow} | v_n \rangle. \quad (1.43)$$

It is also possible to calculate the averages of operators that “move” particles between sites, for example

$$\langle c_{is}^+ c_{js} \rangle = \frac{1}{Z} \sum_n e^{-\beta E_n} \langle v_n | c_{is}^+ c_{js} | v_n \rangle. \quad (1.44)$$

Additionally, density matrix ρ of the model can be calculated:

$$\rho = \frac{1}{Z} \sum_n e^{-\beta E_n} |v_n\rangle \langle v_n| \quad (1.45)$$

Some tasks, such as the calculation of site pairs’ entanglement entropy for our studies (Section 6), only require the reduced density matrix $\rho_A = \text{Tr}_B \rho$ of subset A of sites from the model M , which can be obtained directly without calculation of the full density matrix. This is achieved by running external loop over states of B and thus only calculating the contributions which survive the tracing Tr_B . Matrix

element of ρ_A is

$$\begin{aligned}
& (\rho_A)_{n_{A1\uparrow}n_{A2\uparrow}\dots n'_{A1\uparrow}n'_{A2\uparrow}\dots} = \\
& \frac{1}{Z} \sum_n e^{-\beta E_n} \sum_{n_{B1\uparrow}n_{B2\uparrow}\dots} m_{n_{A1\uparrow}n_{A2\uparrow}\dots n_{B1\uparrow}n_{B2\uparrow}\dots} v_{n_{A1\uparrow}n_{A2\uparrow}\dots n_{B1\uparrow}n_{B2\uparrow}\dots} \cdot \\
& \cdot m_{n'_{A1\uparrow}n'_{A2\uparrow}\dots n_{B1\uparrow}n_{B2\uparrow}\dots} v_{n'_{A1\uparrow}n'_{A2\uparrow}\dots n_{B1\uparrow}n_{B2\uparrow}\dots},
\end{aligned} \tag{1.46}$$

where $B = M - A$ are the rest of the sites, subsystems A and B consist of respective sites $A1, A2, \dots$ and $B1, B2, \dots$. Indices $n_{A(B)is}$ are the Hilbert space vectors of corresponding subsystems and $n_{A1\uparrow}n_{A2\uparrow}\dots n_{B1\uparrow}n_{B2\uparrow}\dots$ are Hilbert space vectors of the whole model. Fermionic signs $m_{n_{A1\uparrow}n_{A2\uparrow}\dots n_{B1\uparrow}n_{B2\uparrow}\dots}$ appear in this sum due to the moving of occupation numbers n_{Ais} to the left in Hilbert space vectors, (for simplicity n_{Ais} were already shown here in the beginning of vectors, but in practice they are scattered across the vector according to current selection of sites for A):

$$\begin{aligned}
& |n_i, n_1, \dots, n_{i-1}, n_{i+1}, \dots, n_N\rangle = m |n_1, \dots, n_{i-1}, n_i, n_{i+1}, \dots, n_N\rangle = \\
& = (-1)^{\sum_{j=1}^{i-1} n_j} |n_1, \dots, n_{i-1}, n_i, n_{i+1}, \dots, n_N\rangle,
\end{aligned}$$

due to the creation and annihilation operators defined in Eq. 1.4.

1.5 Solution of large Hubbard clusters

The inherent challenge of Exact Diagonalization method is that in many-body quantum lattice models of interacting particles, the Hilbert space dimension N_{st} – the number of basis states of the Hamiltonian – grows exponentially as $N_{\text{st}} = K^{N_s}$, where N is the number of sites and K is the number of possible states for each site. This important characteristic restricts possible K and N_s to quite modest numbers. The Hilbert space dimension of the Hubbard model, in which a site has $K=4$ possible states, is only $4^4 = 256$ for $N_s=4$ sites, but already grows to $N_{\text{st.}} = 4^{16} = 4.3 \cdot 10^9$ for $N_s=16$ sites, which would require storing and diagonalizing a prohibitively large matrix of $N_{\text{st.}}^2 = (4.3 \cdot 10^9)^2 = 1.8 \cdot 10^{19}$ elements, which alone would be an order of 10^{11} GiB in double precision floating point numbers.

However, by exploiting the symmetries of the Hamiltonian and properties of the values being calculated from the solution, Exact Diagonalization can be applied to systems such as Hubbard model with $N_s=16$ – and on state-of-the-art hardware it has even been used to study clusters of up to $N_s = 22..24$ sites, albeit away from half-filling: [134, 133].

The symmetries of the Hamiltonian and the choice of occupation number basis allow to separately consider its sectors (see Section 1.1 and Fig. 1.1) with total

number of particles per spin (N_\uparrow, N_\downarrow) of dimension $N_{\text{st.}(N_\uparrow, N_\downarrow)} = C_{N_s}^{N_\uparrow} C_{N_s}^{N_\downarrow}$, where $C_n^k = \frac{n!}{k!(n-k)!}$ is the number of k -combinations out of n elements. This is smaller than dimension of the full Hamiltonian, for example the largest sector $(8_\uparrow, 8_\downarrow)$ of Hubbard Hamiltonian with $N_s = 16$ has the dimension $N_{\text{st.}(8_\uparrow, 8_\downarrow)} = 1.7 \cdot 10^8$, which is $N_{\text{st.}}/N_{\text{st.}(8_\uparrow, 8_\downarrow)} \approx 26$ times smaller.

Secondly, 99.999% of the off-diagonal elements $t_{ij}c_{is}^+c_{js}$ of the Hamiltonian are zeros, making the off-diagonal part a large sparse matrix with density (ratio of non-zero elements to the total number of elements) of ca. $d = (1 - 0.99999) = 0.00001$. Specialized formats exist for compact storage of such matrices, one of the most commonly used ones being Compressed Row Storage (CRS). An approximate memory footprint of matrix with dimension D stored in CRS is $(8+4)dD^2 + 4D$ bytes, where d is the matrix density. It is made up of a double precision (8-byte) value and 4-byte integer column index per element and a 4-byte integer per row. Opposite to that, all diagonal elements U_i and μ are non-zero, and it is more efficient to store them in a separate vector, whose memory footprint is $8D$ bytes with double precision. Resulting memory requirement of Hamiltonian (sub-)sector is

$$12dD^2 + 12D = 0.00012D^2 + 12D$$

bytes. Although 0.00012 may seem small at first glance, the quadratic component grows to considerable sizes at typical dimensions, which can create a problem with large number of hoppings t_{ij} . A solution exists to mitigate the quadratic tendency (see Section 1.6.1).

And finally, only a few low-energy states of the Hamiltonian are required at finite temperature because of $e^{\beta(E_0 - E_n)}$. For most calculations it is enough to use ca. $N_{\text{ev}} = 5$ eigenvectors, which would require memory of

$$8N_{\text{ev}}D = 40D$$

bytes. To extract those states of the Hamiltonian, a partial diagonalization algorithm can be used instead of full diagonalization. Variants of the Arnoldi or Lanczos algorithms work well for this purpose, because they construct Krylov space of $N_{\text{cv}} < D$ vectors by repeated matrix-vector multiplication $\mathcal{H}|v\rangle$, which can be implemented very efficiently for sparse storage formats such as CRS. Typical size of the Krylov space used is $N_{\text{cv}} = 2N_{\text{ev}} + 2$ vectors. The Krylov space with two additional work arrays for the algorithm would then require

$$8(N_{\text{cv}} + 2) = 8(2N_{\text{ev}} + 2 + 2) = 112D$$

bytes of memory, which together with the storage of eigenvectors amounts to $152D$ bytes.

Total estimated memory footprint of a Lanczos-based solver using CRS is then

$$0.00012D^2 + 12D + 152D = 0.00012D^2 + 164D$$

bytes, and solving Hubbard Hamiltonian sector $(8_\uparrow, 8_\downarrow)$ for $N_s = 16$, $D = N_{\text{st.}(8_\uparrow, 8_\downarrow)} = 1.7 \cdot 10^8$ for the low 5 eigenstates would require 3 TiB of memory, which is very large but already possible on a high-end computing node.

Memory requirement of Hubbard model's Hamiltonian can be reduced dramatically by splitting it into two spin subsectors with much smaller dimensions $N_{\text{st.}N_{\uparrow(\downarrow)}} = C_{N_s}^{N_{\uparrow(\downarrow)}}$, For example, $N_{\text{st.}N_{\uparrow(\downarrow)}=8} = 1.3 \cdot 10^4$, which is $N_{\text{st.}(8_\uparrow, 8_\downarrow)} / N_{\text{st.}N_{\uparrow(\downarrow)}=8} = 1.3 \cdot 10^4$ times smaller than the dimension of sector $(8_\uparrow, 8_\downarrow)$. Memory required by solver using this modified storage scheme would be

$$0.00012(N_{\text{st.}N_\uparrow=8}^2 + N_{\text{st.}N_\downarrow=8}^2) + 12(N_{\text{st.}N_\uparrow=8} + N_{\text{st.}N_\downarrow=8}) + 152N_{\text{st.}(8_\uparrow, 8_\downarrow)},$$

or 23 GiB, which would run on a typical computing node.

1.6 Implementation: EDLib

This section discusses technical details of the parallel Exact diagonalization library “EDLib” introduced in [65], that solves the eigenvalue problem of Hubbard model or Anderson impurity model on distributed and shared-memory computing systems. It played an essential part in this study by calculating the properties of 2×2 plaquette and 4×4 Hubbard cluster (Sections 3, 5) and generating input data for the other methods. The library is available at [36].

1.6.1 Storage formats

Spin-resolved Hamiltonian storage format

Usually interaction part of the hamiltonian is diagonal and does not require additional effort to compute matrix vector product in this subsection we will consider the matrix representation of the hopping term of the Hamiltonian (1.6) only. Since the hopping Hamiltonian does not contain hopping between different spins it can be decomposed into two parts for each spin. In the matrix representation the hopping Hamiltonian in this case can be expressed as follows:

$$\mathcal{H}_{hop} = \mathcal{H}_\uparrow \oplus \mathcal{H}_\downarrow = \mathcal{H}_\uparrow \otimes I_\downarrow + I_\uparrow \otimes \mathcal{H}_\downarrow, \quad (1.47)$$

where I_σ is the identity matrix with the same dimension as \mathcal{H}_σ , and Hamiltonian matrices for each spin can be stored separately. Since dimension of \mathcal{H}_σ is much smaller than the original Hamiltonian matrix, the only problem is to store the eigenvectors since the Hilbert space still grows exponentially. To deal with this issue in this library we implement the distributed storage of the vector as will be described in the next subsection.

MPI parallelization In this library for solving the eigenvalue problem we use a parallel version of the implicitly restarted Arnoldi algorithm library [77], which requires implementation of the matrix-vector products. In the case of a matrix decoupled into diagonal and two (for each spin) off-diagonal matrices parts (See Eq. 1.47) we can decompose initial vector of size $\dim(\mathcal{H}_\uparrow) \dim(\mathcal{H}_\downarrow)$ into set of $\dim(\mathcal{H}_\uparrow)$ vectors of size $\dim(\mathcal{H}_\downarrow)$ to compute the contribution of the off-diagonal parts of Hamiltonian matrix.

Let's, for example, consider Hubbard dimer at the half-filling. It has four possible basis states in occupation number basis ($|-, \uparrow\downarrow\rangle, |\downarrow, \uparrow\rangle, |\uparrow, \downarrow\rangle, |\uparrow\downarrow, -\rangle$). And the corresponding hopping Hamiltonian matrix will have the following structure:

$$\mathcal{H}_{hop} = \begin{pmatrix} 0 & t_\downarrow & t_\uparrow & 0 \\ t_\downarrow & 0 & 0 & t_\uparrow \\ t_\uparrow & 0 & 0 & t_\downarrow \\ 0 & t_\uparrow & t_\downarrow & 0 \end{pmatrix},$$

where t_σ is the hopping integral for spin σ . Since there is no hopping between different spins the basis set can be separated into two basis sets for spin- \uparrow ($|-, \uparrow\rangle, |\uparrow, -\rangle$) and spin- \downarrow ($|-, \downarrow\rangle, |\downarrow, -\rangle$) parts:

$$\mathcal{H}_\uparrow = \begin{pmatrix} 0 & t_\uparrow \\ t_\uparrow & 0 \end{pmatrix}, \mathcal{H}_\downarrow = \begin{pmatrix} 0 & t_\downarrow \\ t_\downarrow & 0 \end{pmatrix}. \quad (1.48)$$

And for some arbitrary vector $x = (x_1, x_2, x_3, x_4)^T$ the matrix-vector product $|y\rangle = \mathcal{H}_{hop}|x\rangle$ can be computed separately for spin- \uparrow and spin- \downarrow part of the Hamiltonian matrix as follows:

$$|y\rangle = \mathcal{H}_{hop} \begin{pmatrix} x_1 \\ x_2 \\ x_3 \\ x_4 \end{pmatrix} = \begin{pmatrix} t_\downarrow x_2 + t_\uparrow x_3 \\ t_\downarrow x_1 + t_\uparrow x_4 \\ t_\downarrow x_4 + t_\uparrow x_1 \\ t_\downarrow x_3 + t_\uparrow x_2 \end{pmatrix} = \begin{pmatrix} \mathcal{H}_\downarrow & \\ & \mathcal{H}_\uparrow \end{pmatrix} \begin{pmatrix} x_1 \\ x_2 \\ x_3 \\ x_4 \end{pmatrix} + \mathcal{H}_\uparrow \begin{pmatrix} x_1 \\ x_2 \\ x_3 \\ x_4 \end{pmatrix} = \quad (1.49)$$

$$= \begin{pmatrix} \mathcal{H}_\downarrow x_1^{(\downarrow)} \\ \mathcal{H}_\downarrow x_2^{(\downarrow)} \end{pmatrix} + \mathcal{H}_\uparrow \begin{pmatrix} x_1^{(\downarrow)} \\ x_2^{(\downarrow)} \end{pmatrix}. \quad (1.50)$$

This can be generalized for the whole matrix of arbitrary dimension for the Hamiltonian 1.6, and matrix-vector product can be performed by three separate operations:

$$\mathcal{H} \begin{pmatrix} x_1 \\ x_2 \\ \dots \\ x_3 \end{pmatrix} = \mathcal{H}_{loc} \begin{pmatrix} x_1 \\ x_2 \\ \dots \\ x_3 \end{pmatrix} + \begin{pmatrix} \mathcal{H}_\downarrow x_1^{(\downarrow)} \\ \mathcal{H}_\downarrow x_2^{(\downarrow)} \\ \dots \\ \mathcal{H}_\downarrow x_3^{(\downarrow)} \end{pmatrix} + \mathcal{H}_\uparrow \begin{pmatrix} x_1^{(\downarrow)} \\ x_2^{(\downarrow)} \\ \dots \\ x_3^{(\downarrow)} \end{pmatrix}, \quad (1.51)$$

where $x_i^{(\downarrow)}$ is an i -sub-vector of initial vector x with a dimension of $\dim(\mathcal{H}_\downarrow)$. It is clear to see vector can be simply distributed along different processors by integer numbers of $x_i^{(\downarrow)}$ sub-vectors. The only operation that needs to perform inter-processor communication is the last term in the right part of the Eq. 1.51. In this case we can overlap communications and computations by using one-sided MPI communications:

```
// Perform initial synchronization 1
MPI_Win_fence(MPI_MODE_NOPRECEDE, _win); 2
// Initiate remote data transfer for up-spin term 3
MPI_Get(...) 4
// Compute diagonal contribution. 5
... 6
// Compute down-spin contribution 7
... 8
// Perform final synchronization 9
MPI_Win_fence(MPI_MODE_NOSUCCEED | MPI_MODE_NOPUT | MPI_MODE_NOSTORE, _win); 10
// Compute up-spin contribution and off-diagonal interactions contribution. 11
12
```

This strategy make able to perform only a single inter-process communication for each matrix-vector product to reduce a network overhead.

Scaling properties Fig. 1.5 shows how the program scales with the number of MPI processes for doped 16 sites Hubbard cluster on the NERSC Edison Cray high-performance cluster. We see that the actual speedup behaves proportionally to $N_p^{0.9}$. The principal reason for this behavior is that a larger number of processes leads to more inter-node communication compared to mostly intra-node communication for a small number of processes. One way to improve the scalability is to dedicate a single core for communications. Work in this direction is currently in progress.

Signs-only Compressed Row storage format

In the other sparse matrix format – “*Signs Only Compressed Row Storage*” (SOCRS) – we attempt to reduce the memory footprint of the Hamiltonian matrix without relying on spin conservation, which would allow to solve models with inter-spin hopping.

Since the off-diagonal elements of the Hamiltonian matrix stored in the Compressed Row Storage (CRS) format make up most of its memory footprint, and their values are already stored in the hopping matrix t_{ij} , it is straightforward to remove them. However, for Fermi-Dirac statistics there is an additional sign which is negative

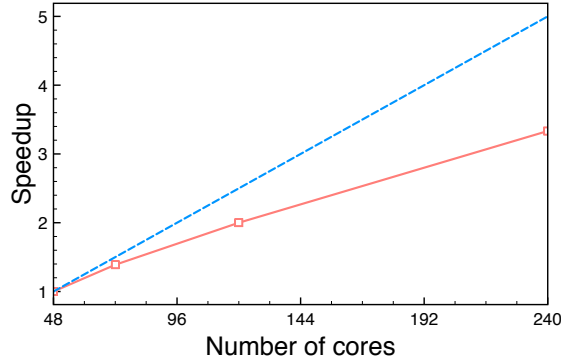


FIGURE 1.5: Parallel speed-up in comparison to ideal speedup for the 16-site Hubbard cluster.

if the number of electrons between the creation and annihilation sites is odd:

$$\hat{c}_j |m\rangle = (-1)^{s_j} |\dots\rangle,$$

$$s_j = \sum_{i < j} n_i,$$

The time penalty of calculating these signs on-the-fly is prohibitive. We propose the following scheme (illustrated on Fig. 1.6), which seems to be a good compromise.

First the Hamiltonian matrix is initialized in the following steps.

1. The diagonal is filled and stored separately.
2. For each Fock state, corresponding to a row in the matrix, all possible hoppings (from orbital i to j) are generated, and for each of them:
 - (a) if $t_{ij} = 0$, skip the rest of this step;
 - (b) the column index of the new Fock state is calculated;
 - (c) the fermionic sign is calculated and stored as a single bit in CRS-like format.

The `row_ptr` is redundant, because the number of offdiagonal elements in each row is known from the number of hoppings.

The SpMV procedure is then the following.

1. The output vector is filled with the result of element-by-element multiplication of the input vector and the diagonal.

- The hopping matrix is traversed in the same order as the second step of the initialization procedure to retrieve the sign and the column index from the storage, which are used together with corresponding values t_{ij} .

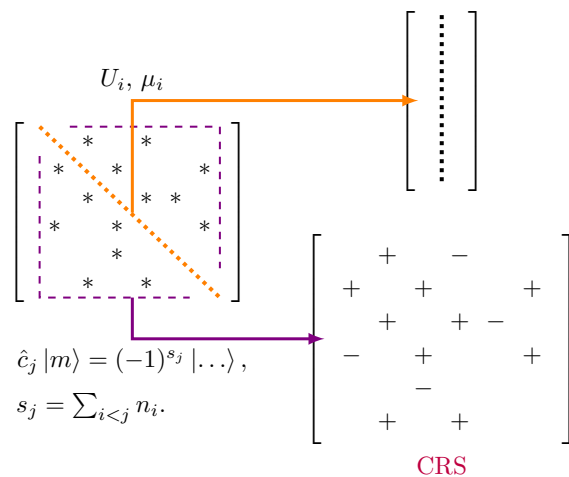


FIGURE 1.6: SOCRS – the suggested improvement of CRS format. Signs of the off-diagonal elements are stored in the compressed format, the diagonal is stored separately.

While the reduction of memory requirement should not be expected to match that of Spin Resolved Storage, the format improves considerably over plain CRS. The comparison of memory footprint is shown on Fig. 1.7.

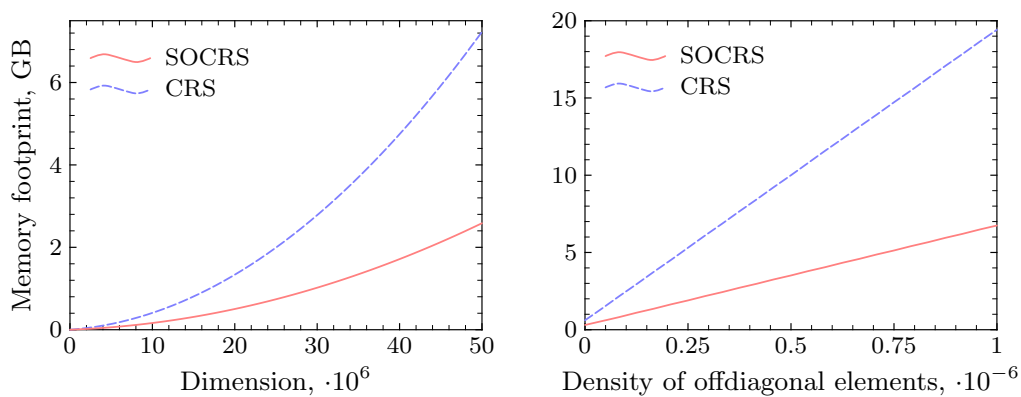


FIGURE 1.7: Memory footprint of SOCRS and CRS. Density of the offdiagonal elements is defined $\rho = N_{od}/D^2$, where N_{od} is the number of nonzero offdiagonal elements, D – matrix dimension.

1.6.2 Program description

The EDLib library is designed to solve the exact diagonalization problem for electronic quantum Hamiltonians. For large matrix cases we use parallelization by means of MPI or OpenMP (depending on a storage type). The program is written in standard C++11 and distributed as a template library. The program has been checked using GNU, Intel and Clang C++ compilers. The test run has also been checked on the University of Michigan high-performance computing (HPC) cluster and on the NERSC Edison Cray machine.

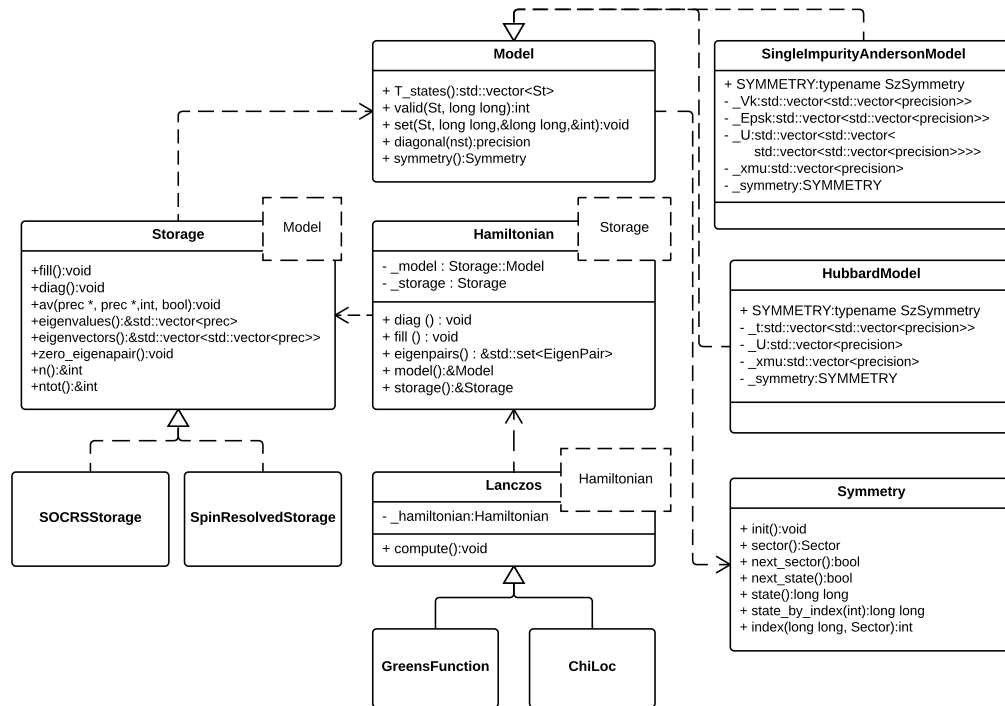


FIGURE 1.8: UML diagram of classes implemented in EDLib library.

Class diagram

The structure of the EDLib library can be represented by the UML diagram shown at Fig. 1.8. The main class of the presented library is the `Hamiltonian` which is parametrized by a type of `Storage` for a chosen `Model`. The main method for exact diagonalization is `diag` that mostly delegates the work to the specified `Storage` class. The Green's functions (`GreenFunction` class) are computed by the Lanczos continued fraction method (`Lanczos` class).

Library usage

To start using library one should define and read parameters and initialize the Hamiltonian class instance. For example, for the Hubbard cluster this can be done as follows:

```
// Define Hamiltonian type 1
typename EDLib::Hamiltonian < EDLib::Storage::SRSSStorage < EDLib::Model:: 2
    HubbardModel < double > > > HamType;
// Define and read parameters 3
alps::params params(argc, argv); 4
EDLib::define_parameters(params); 5
// Hamiltonian object initialization 6
HamType ham(params, comm); 7
```

The Hamiltonian diagonalization can be simple done by the method `diag` call on the Hamiltonian class instance. The resulting eigenpairs can be obtained by the `eigenpairs` method, that returns an ordered set of `EigenPair` class instances. Each eigenpair object has `eigenvalue` and `eigenvector` methods and as well the method `sector` that contains symmetry properties for a current eigenvalue. After the Hamiltonian diagonalization one can use eigen-pairs that have been found to calculate different static and dynamic observables.

Observables

The EDLib library can compute various static and dynamic observables. The following static observables for each orbital can be calculated:

- total occupancy;
- double occupancy;
- occupancy per spin;
- magnetic moment.

To compute static observables one should call the `calculate_static_observables` method of a `StaticObservables` class instance. Another important static observable that can be calculated is a major electronic configuration for each eigenvalue. It returns a set of basis functions that give the major contribution to the eigenstate with the correspondent weight for each basis function. This can be done by the `print_major_electronic_configuration` method call on a `StaticObservables` class instance.

The following dynamic observables can be computed:

- single particle Green's function ($G(z)$);
- charge-charge susceptibility ($\chi_{NN}(z)$);

- longitudinal spin-spin susceptibility ($\chi_{zz}(z)$);

All dynamic observables can be computed either on a Matsubara frequency mesh or on a real frequency mesh. In the current version of the EDLib library only local dynamic observables can be computed. For interoperability we use ALPSCore Green's functions[40] as the containers for dynamic observables. To compute one of the the dynamical observables one can simply follow the example below:

```

// Init and diagonalize Hamiltonian
HamType ham(params, comm);
ham.diag();
// Create Green's function object
// It should be parametrized by Hamiltonian type and by grid type
EDLib::gf::GreensFunction < HamType, alps::gf::real_frequency_mesh >
    greensFunction(params, ham);
// compute Green's function
greensFunction.compute();
// save results to HDF5 file
greensFunction.save(ar, "results");

```

To choose a frequency grid type one should parametrize a GreensFunction class instance with either type:

- `alps::gf::real_frequency_mesh`
- `alps::gf::matsubara_positive_mesh`

and proper Matsubara statistics as shown in the listing below:

```

// Real frequency Green's function
EDLib::gf::GreensFunction < HamType, alps::gf::real_frequency_mesh > realfreqGF(
    params, ham);
// Matsubara frequency fermionic Green's function
EDLib::gf::GreensFunction < HamType, alps::gf::matsubara_positive_mesh, alps::gf
    ::statistics::statistics_type > matsubaraGF(params, ham, alps::gf::statistics
    ::statistics_type::FERMIONIC);

```

The detailed examples are located in `examples` subdirectory of the main EDLib source directory.

Description of the input data

Input data to the EDLib library take the form of two separate files. One is the parameter file and `onethr` is the model specific HDF5 file. Table 1.1 represents the complete list of the parameters that can be defined in the parameter file. The structure of HDF5 files is model specific and for its generation we provide Python scripts for each represented model.

1.6.3 Examples

To show the ability of the presented library we consider two problems. The first problem is groundstate calculation of the 16-site Hubbard model. And the second

Parameter name	Description
NSITES	Number of sites
NSPINS	Number of spins
INPUT_FILE	HDF5 input file
Storage parameters	
storage.MAX_SIZE	Number of eigenvalues to find
storage.MAX_DIM	Number of eigenvalues to find
storage.EIGENVALUES_ONLY	Compute only eigenvalues
spinstorage.ORBITAL_NUMBER	Number of orbitals with interaction
ARPACK parameters	
arpack.SECTOR	Read symmetry sectors from file
arpack.NEV	Number of eigenvalues to find
arpack.NCV	Number of convergent values
Lanczos parameters	
lanc.NOMEGA	Number of Matsubara frequencies
lanc.NLANC	100, "Number of Lanczos iterations
lanc.BETA	10.0, "Inverse temperature
lanc.BOLTZMANN_CUTOFF	Cutoff for Boltsman factor
single impurity Anderson Model	
siam.NORBITALS	Number of impurity orbitals

TABLE 1.1: Input parameters description

one is the ground state properties of the single *Co* impurity adsorbed on the *Pt*(111) surface.

Finite Hubbard cluster diagonalization

The isolated 16-site cluster we study is a system of four identical plaquettes with periodic boundary conditions. Its schematic representation is shown on the Fig. 1.9. The solid and dashed lines correspond to nearest neighbour hopping t and second nearest neighbour hopping t' respectively. The 4-site plaquette is a minimal and generic electronic-structure model of cuprate superconductors proposed in [53] – which demonstrates a triple degenerate point that merges two singlets and two doublets. Its properties have previously been studied in isolation, in the bath and in the Bethe lattice. For the present calculation the following parameters have been chosen: $t = 1.0eV$, $t' = -0.3eV$, $U = 6.0eV$ and $\mu = 0.54eV$. The resulting lowest energy is $E_0 = -22.6421eV$. Fig. 1.10 shows the local single-particle Green's function and the spin susceptibility on Matsubara frequencies for the parameters indicated below at the ground state.

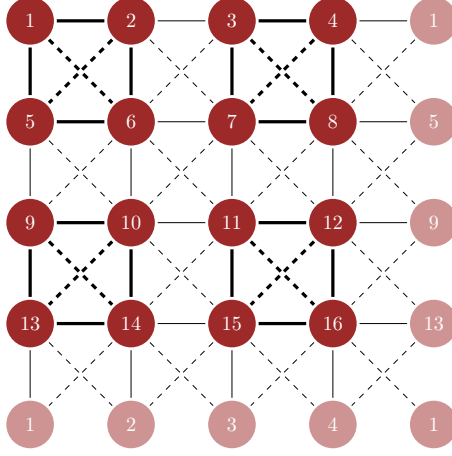


FIGURE 1.9: Schematic representation of the 16-site cluster with periodic boundary condition.

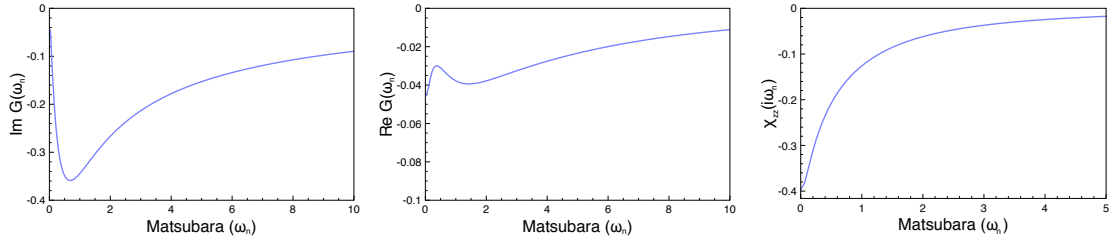


FIGURE 1.10: Local Matsubara Green's functions for the 16-site cluster. (left) Imaginary part of single-particle Green's function, (center) real part of single-particle Green's function, (right) spin susceptibility.

The Co adatom on the Pt(111) surface

The electronic and transport properties of the single transition metal adsorbed on the various types of surface play a crucial role in the proper description of giant magnetic anisotropy [41] or Kondo physics [97, 136, 91]. In this simulation we present results for electronic configuration of the ground state of the single cobalt adatom adsorbed on the Pt(111) surface by means of the Anderson impurity model. The model parameters are obtained from first principles calculation. The experimental value of lattice constant for the bulk fcc Pt is 3.92 \AA [38, 88]. Since the relaxation for different stackings, *fcc* and *hcp*, as shown in previous study [15] does not show much difference, we perform simulation for *hcp* position of the cobalt adatom as presented in Fig. 1.11.

For the Anderson Impurity model we choose 5 orbitals for *d*-states of the cobalt adatom, two orbitals in the bath for each *xz, yz* and $3z^2 - r^2$ cobalt orbitals and

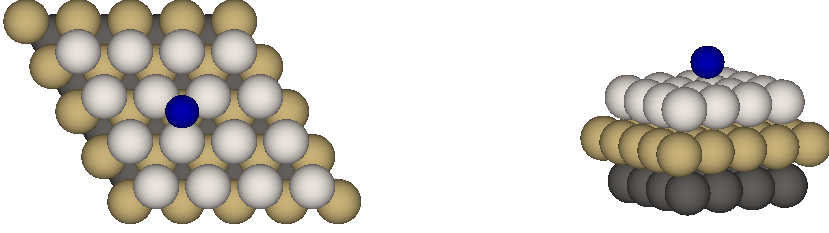


FIGURE 1.11: The schematic representation of *hcp* position of the Co adatom adsorbed on the Pt(111) surface. The blue sphere shows the cobalt atom and gray spheres correspond to the Pt surface.

Orbital	V_k , eV	ε_k , eV
$xy, x^2 - y^2$	0.56434; 0.68392; 0.29519	-2.37325; -0.87328; 2.01265
xz, yz	0.81892; 0.99136	-3.15496; -1.69066
$3z^2 - r^2$	0.77347; 0.79785	-5.59842; -2.95325

TABLE 1.2: Discretized bath parameters for orbitals of different symmetries.

three orbitals in the bath for each xy and $x^2 - y^2$ cobalt orbitals. Based on the spin symmetries and block-diagonal structure of the Hamiltonian matrix the dimension of the largest block is about $\approx 590 \times 10^6$. For the present calculations we choose the following parameters: $U = 6.6$ eV, $J_H = 0.9$ eV, $\mu = 44.44$ eV, and the bath parameters are presented in the Table 1.2. The interaction part of the Hamiltonian is expressed by using Slater integral representation of the full rotational invariant Coloumb interaction tensor [117] with $F^0 = U$, $F^2 = 14J_H/(1 + 0.625)$ and $F^4 = 0.625F^2$ [43]. We perform diagonalization of each symmetry sector to find the electronic configuration of the ground state.

The simulation is performed on the Edison Cray machine and takes about 1600 core-hours on 10 nodes with maximum memory requirement about 10 Gb per node. The resulting electronic configuration is presented in Table 1.3, in addition we present the lowest energy for the half-filled states. The partial densities of states and spin-spin correlation functions for cobalt d -shell are shown in Fig. 1.12

1.6.4 Extension

The EDLib is designed to be extensible for different electron models. One of the possible extension is the Holstein-Anderson impurity model. This model in addition to electron bath contains bosonic bath and can be expressed by the following

ΔE , eV	n_\uparrow	n_\downarrow	Sector size	Major contribution to the g.s.
0.0	12	15	841568	$\downarrow \uparrow\downarrow \downarrow \uparrow\downarrow \downarrow$
0.0	13	14	1618400	$\uparrow \uparrow\downarrow \downarrow \uparrow\downarrow \downarrow + \downarrow \uparrow\downarrow \downarrow \uparrow\downarrow \uparrow + \downarrow \uparrow\downarrow \uparrow \uparrow\downarrow \downarrow$
0.0	14	13	1618400	$\downarrow \uparrow\downarrow \uparrow \uparrow\downarrow \uparrow + \uparrow \uparrow\downarrow \uparrow \uparrow\downarrow \downarrow + \uparrow \uparrow\downarrow \downarrow \uparrow\downarrow \uparrow$
0.0	15	12	841568	$\uparrow \uparrow\downarrow \uparrow \uparrow\downarrow \uparrow$
.....				
13.471	9	8	590976100	
13.471	8	9	590976100	

TABLE 1.3: The resulting electronic configuration for exact diagonalization study of the Co adatom adsorbed on the Pt(111).

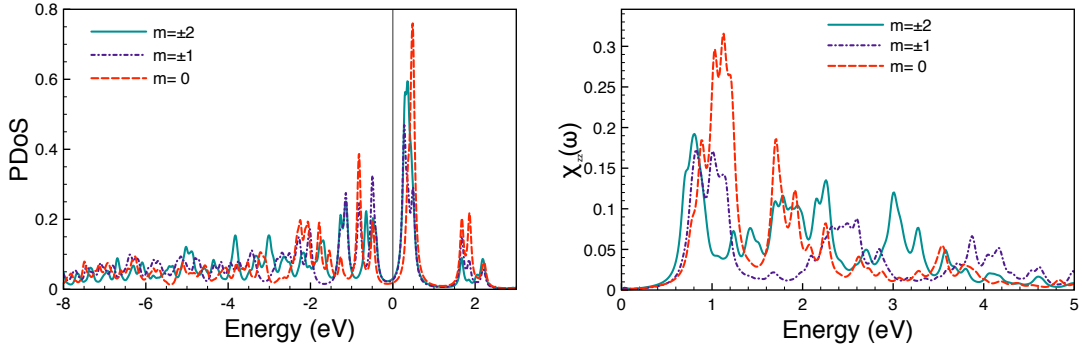


FIGURE 1.12: (left) The partial densities of states for d -shell and (right) spin-spin correlation functions of a single Co adatom adsorbed on the Pt(111) surface.

Hamiltonian:

$$\begin{aligned}
\mathcal{H}_{imp} = & \sum_{\sigma} \varepsilon_d d_{\sigma}^{\dagger} d_{\sigma} + U n_{\uparrow} n_{\downarrow} + \sum_{k\sigma} (\hat{V}_k d_{\sigma}^{\dagger} c_{k\sigma} + h.c.) + \sum_{k,\sigma} \varepsilon_k c_{k\sigma}^{\dagger} c_{k\sigma} + \\
& \sum_p \Omega_p b_p^{\dagger} b_p + \sum_p \hat{W}_p (b_p^{\dagger} + b_{-p})(n_{\uparrow} + n_{\downarrow} - \langle N \rangle), \quad (1.52)
\end{aligned}$$

where the first four terms correspond to the single impurity Anderson model and the last two terms describe bosonic bath and its coupling to the impurity, respectively. It can be useful to study non-local interaction in lattices within Extended DMFT [121]. To solve this Hamiltonian by means of exact diagonalization we need to make an assumption that the occupancy of the bosonic states is finite within some cut-off. To extend the EDLib library for this model according to the UML diagram (Fig. 1.8) the first two things we need to define is the class that will describe this model and the class that make it able to iterate over all possible basis sets.

The model definition should contain the contribution to the Hamiltonian matrix diagonal and off-diagonal terms. For this case methods `diagonal`, `valid` and `set` should be implemented. For the basis set iterator we should extend the `Symmetry` class. The detailed class definition for model and the basis set class can be found in the `include/ext` directory in the root source folder.

Chapter 2

Cluster Dual Fermion

The *Dual Fermion* (DF) approach introduced by Rubtsov et al. in [108] allows to account for spatial correlations beyond dynamical mean-field theory. It expands around an arbitrary impurity problem (which is called the *reference system*) and introduces auxiliary fermionic degrees of freedom through a continuous Hubbard-Stratonovich transformation of the partition function's path integral. The Hubbard-Stratonovich transformation maps the fermions of the reference system with strong local correlations to weakly correlated and delocalized, so called *dual*, fermions.

The Hubbard-Stratonovich transformation is required to circumvent the obstacle of Wick's theorem not being applicable to the reference system described by the Hamiltonian in the atomic limit, which is because of two-body operators being present in the Hamiltonian. When transformaing the original action, auxiliary degrees of freedom are introduced, and then the original fermions are integrated out. The resulting action contains n-particle interactions up to all orders given by connected correlation functions of the unperturbed systems.

The reference system for the simple Dual Fermion method is an atom, whereas the *Cluster Dual Fermion* (CDF) metod discussed here expands around a local quantum impurity problem, for example a Hubbard cluster. An optimal choice of the impurity problem allows to establish relation to the dynamical mean-field theory, which appears in the approach as the zero-order approximation.

2.1 Dual Fermion approach with a general reference system

We start with a general lattice fermion model with the local Hubbard-like interaction vertex U . Generalisation to the multi-orbital case with general interactions is straightforward [50]. The general strategy is related to the formally exact separation of the local and non-local correlations effects. We introduce auxiliary dual fermionic

fields which will couple local correlated impurities or clusters back to the original lattice [108].

Using the path-integral formalism the partition function of a general fermionic lattice system can be written in the form of the functional integral over Grassmann variables $[c^*, c]$:

$$Z = \int \mathcal{D}[c^*, c] \exp(-S_L[c^*, c]) \quad (2.1)$$

The original action of interacting lattice fermions can be expressed as the sum of the one-electron contribution and the interaction. The former is most conveniently represented in Matsubara and momentum space, using the Fourier transformed hopping matrix $\hat{t}_{\mathbf{k}}$ (in the single-orbital case, this provides the energy spectrum), whereas the Hubbard interaction U is local and instantaneous and is therefore treated in imaginary time and real space. Any type of local multi-orbital interaction is allowed.

$$S_L[c^*, c] = - \sum_{\mathbf{k}\nu\sigma} c_{\mathbf{k}\nu\sigma}^* [i\nu + \mu - \hat{t}_{\mathbf{k}}] c_{\mathbf{k}\nu\sigma} + \sum_i \int_0^\beta d\tau U n_{i\tau\uparrow}^* n_{i\tau\downarrow}. \quad (2.2)$$

Here and in the following, $\nu = (2n + 1)\pi/\beta$ ($\omega = 2n\pi/\beta$), with $n \in \mathbf{Z}$, are the fermionic (bosonic) Matsubara frequencies, β is the inverse temperature, τ is the imaginary time in the interval $[0, \beta)$, μ is the chemical potential, the index i labels the lattice sites, m refers to different orbitals (\hat{t} can be a matrix in orbital space), σ is the spin projection and the \mathbf{k} -vectors are quasimomenta. In order to keep the notation simple, it is useful to introduce the combined index $|1\rangle \equiv |i, m, \sigma, \tau\rangle$ while assuming summation over repeated indices. Summation over Matsubara frequencies ν assume normalization factor $1/\beta$ and the \mathbf{k} integration normalized by volume of Brillouin zone. Translational invariance is assumed for simplicity in the following, although a real space formulation is possible [124].

In order to formulate an expansion around a suitable reference action, as illustrated in Fig. 2.1, a quantum cluster problem is introduced by a general frequency dependent hybridization function $\hat{\Delta}_\nu$ and the same local interaction,

$$S_\Delta[c_i^*, c_i] = - \sum_{\nu, \sigma} c_{i\nu\sigma}^* [i\nu + \mu - \hat{\Delta}_\nu] c_{i\nu\sigma} + \sum_\nu U n_{i\nu\uparrow}^* n_{i\nu\downarrow}. \quad (2.3)$$

$\hat{\Delta}_\nu$ in this notation is the effective ‘‘hybridization’’ matrix which describes hoppings inside the cluster as well connections to an auxiliary fermionic bath. Note that $\hat{\Delta}_\nu$ is allowed to contain instantaneous parts, i.e., finite asymptotic for $\nu \rightarrow \infty$. The main motivation for rewriting the lattice action in terms of a quantum cluster model is that such a reference system can be solved numerically exactly for a given hybridization

function using Exact Diagonalization (ED) or continuous time Quantum Monte Carlo (CT-QMC) [46]. In this work, we use an isolated cluster as a reference model. In that case, Δ is completely instantaneous and the model is solvable by ED.

Using the locality of the hybridization function $\hat{\Delta}_\nu$, the lattice action Eq. (2.2) can be rewritten exactly in terms of the individual impurity models and the effective one-electron coupling ($\hat{\Delta}_\nu - \hat{t}_\mathbf{k}$) between different impurities (or plaquettes):

$$S_L[c^*, c] = \sum_i S_\Delta[c_i^*, c_i] + \sum_{\mathbf{k}\nu\sigma} c_{\mathbf{k}\nu\sigma}^* \left(\hat{t}_\mathbf{k} - \hat{\Delta}_\nu \right) c_{\mathbf{k}\nu\sigma} \quad (2.4)$$

Although we can solve an individual impurity model exactly, in the present formulation the effect of spatial correlations due to the second term in Eq.(2.4) is still problematic, since the impurity action is non-Gaussian and one cannot use the Wick's theorem.

The main idea of the dual fermion transformation is the change of variables from strongly correlated fermions (c^*, c) to weakly correlated “dual” Grassmann fields (d^*, d) in the path integral representation for the partition function from Eq. (2.1), followed by a simple perturbation treatment. The new variables were introduced through the following Hubbard-Stratonovich (HS)-transformation [120, 59] with the following single-particle matrix $\tilde{t}_{\mathbf{k}\nu} = \left(\hat{t}_\mathbf{k} - \hat{\Delta}_\nu \right)$.

$$e^{-c_1^* \tilde{t}_{12} c_2} = \det [\tilde{t}] \int \mathcal{D}[d^*, d] e^{d_1^* \tilde{t}_{12}^{-1} d_2 - d_1^* c_1 - c_1^* d_1} \quad (2.5)$$

We can immediately see this HS-transformation “localizes” the $[c_i^*, c_j]$ fermions: while on the left hand-side they are still “hopping” through the lattice, on the right-hand side they are localized on one site ($[c_i^*, c_i]$).

Compared to the original dual fermion scheme [108], we perform the Hubbard-Stratonovich decoupling here without any scaling factors related with local Green's function to reduce the number of matrix multiplications in the final algorithm [81]. In this way, the notation of the formalism becomes closer to the original strong-coupling expansion [112, 99, 100, 34, 33]. Nevertheless, it is important to stress the crucial difference: the dual fermion theory includes the freedom to choose an arbitrary hybridisation function Δ .

With this reference system the lattice partition function becomes

$$\frac{Z}{Z_d} = \int \mathcal{D}[c^*, c, d^*, d] \exp(-S[c^*, c, d^*, d]) \quad (2.6)$$

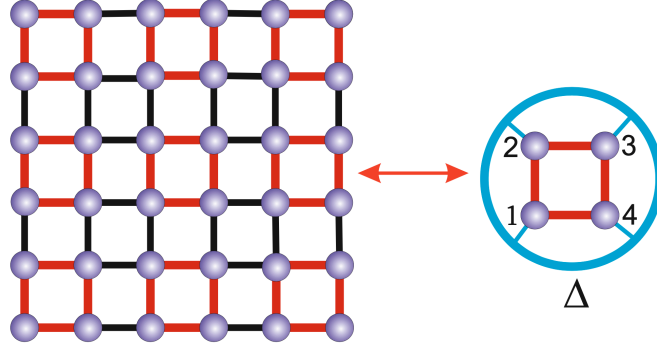


FIGURE 2.1: Schematic representation of a plaquette reference system for the square lattice.

with $Z_d = \det [\tilde{t}]$. The lattice action transforms to

$$S[c^*, c, d^*, d] = \sum_i S_\Delta^i - \sum_{\mathbf{k}, \nu, \sigma} d_{\mathbf{k}\nu\sigma}^* \left(\hat{t}_k - \hat{\Delta}_\nu \right)^{-1} d_{\mathbf{k}\nu\sigma} \quad (2.7)$$

Hence the coupling between sites is transferred to a local coupling to the auxiliary fermions:

$$S_\Delta^i[c_i^*, c_i, d_i^*, d_i] = S_\Delta[c_i^*, c_i] + \sum_{\nu, \sigma} (d_{i\nu\sigma}^* c_{i\nu\sigma} + c_{i\nu\sigma}^* d_{i\nu\sigma}) \quad (2.8)$$

For the last term we use the invariance of the trace so that the sum over all states labeled by \mathbf{k} could be replaced by the equivalent summation over all sites by a change of basis in the second term. The crucial point is that the coupling to the auxiliary fermions is purely local and S_Δ^i decomposes into a sum of local terms. The lattice fermions can therefore be integrated out from S_Δ^i for each site i separately. This completes the change of variables:

$$\frac{1}{Z_\Delta} \int \mathcal{D}[c^*, c] \exp(-S_\Delta^i[c_i^*, c_i, d_i^*, d_i]) = \exp\left(-\sum_{\nu, \sigma} d_{i\nu\sigma}^* g_\nu d_{i\nu\sigma} - V_i[d_i^*, d_i]\right) \quad (2.9)$$

where Z_Δ is partition function of impurity action S_Δ Eq. (2.3) and g_ν is the exact impurity Green function

$$g_{12} = -\langle c_1 c_2^* \rangle_\Delta = \frac{1}{Z_\Delta} \int \mathcal{D}[c^*, c] c_1 c_2^* e^{-S_\Delta[c^*, c]} \quad (2.10)$$

The above equation may be viewed as the defining equation for the dual potential $V[d^*, d]$. The choice of the dual transformation in the form of Eq.(2.5), without the traditional renormalization of the d -fields by a factor of g_ν^{-1} , ensures a particularly simple form of this potential. The price that we pay for this simple form is the unconventional dimensionality of the dual Green's function and self-energy, but it proves to be very convenient for numerical multiorbital/cluster calculations. An explicit expression is found by expanding both sides of Eq. (2.9) and equating the resulting expressions order by order. While formally this can be done up to all orders, and in this sense the transformation to the dual fermions is exact, for most applications it is enough to approximate the dual potential by the first non-trivial interaction vertex:

$$V[d^*, d] = \frac{1}{4} \sum_{1234} \gamma_{1234}^P d_1^* d_2^* d_3 d_4 \quad (2.11)$$

where for the local vertex the combined index $1 \equiv \{m\nu\sigma\}$ consists of orbital degrees of freedom (or cluster sites), frequency, and spin. γ is the exact, fully antisymmetric, reducible two-particle vertex of the local quantum impurity problem, in the particle-particle notation (denoted by the index P). The absence of normalization in the HS-transformation (2.5) leads to the impurity "legs" remain "unamputated". Normally this procedure implies division by the single-particle Green's functions. In the multiorbital case, this division involves a potentially unstable matrix inversion, which is avoided by the present choice of normalization. The vertex is then given by the connected part of the local two-particle correlations function

$$\gamma_{1234} = \kappa_{1234} - \kappa_{1234}^0 \quad (2.12)$$

with the two-particle Green's function of the local reference system being defined in particle-particle notation as :

$$\kappa_{1234}^P = \langle c_1 c_2 c_4^* c_3^* \rangle_\Delta = \frac{1}{Z_\Delta} \int \mathcal{D}[c^*, c] c_1 c_2 c_4^* c_3^* e^{-S_\Delta[c^*, c]} \quad (2.13)$$

The disconnected part of the impurity two-particle Green function is

$$\kappa_{1234}^0 = g_{13}g_{24} - g_{14}g_{23} \quad (2.14)$$

The single- and two-particle Green functions can be calculated using the CT-QMC Monte Carlo algorithms [46]. After integrating out the lattice fermions, the dual action depends on the new variables only and for the one-orbital paramagnetic case is

$$\tilde{S}[d^*, d] = - \sum_{\mathbf{k}\nu\sigma} d_{\mathbf{k}\nu\sigma}^* \tilde{G}_{0\mathbf{k}\nu}^{-1} d_{\mathbf{k}\nu\sigma} + \sum_i V_i [d_i^*, d_i], \quad (2.15)$$

the bare dual Green function having the following form

$$\tilde{G}_{\mathbf{k}\nu}^0 = \left[\left(\hat{t}_{\mathbf{k}} - \hat{\Delta}_{\nu} \right)^{-1} - g_{\nu} \right]^{-1}. \quad (2.16)$$

Action Eq.(2.15) allows us to calculate the dual self-energy $\tilde{\Sigma}$ with a chosen level of approximation. After this, we transform the results back using an exact relation between the dual and lattice Green's functions (Section 2.3).

The lattice self-energy is a sum of the reference contribution Σ^0 (i.e the self-energy of the impurity or the cluster) and correction Σ' (which is related to the dual self-energy $\tilde{\Sigma}$ in the following manner [106])

$$\begin{aligned} \Sigma_{\mathbf{k}\nu} &= \Sigma_{\nu}^0 + \Sigma'_{\mathbf{k}\nu} \\ \Sigma'_{\mathbf{k}\nu} &= g_{\nu}^{-1} - (g_{\nu} + \tilde{\Sigma}_{\mathbf{k}\nu})^{-1} \end{aligned} \quad (2.17)$$

For numerical calculations, instead of calculating the lattice self-energy, it is more convenient to directly use a simple connection between the dual self-energy and lattice Green's function[108]

$$G_{\mathbf{k}\nu} = \left[\left(g_{\nu} + \tilde{\Sigma}_{\mathbf{k}\nu} \right)^{-1} - \tilde{t}_{\mathbf{k}\nu} \right]^{-1}. \quad (2.18)$$

where $\tilde{\Sigma}_{\mathbf{k}\nu}$ is calculated via diagrammatic perturbation scheme using the $\tilde{G}_{0\mathbf{k}\nu}^{-1}$ matrix and plaquette vertex γ_{1234} . The properly rescaled dual self energy plays the role of a T-matrix for the the reference Green's function g . With this relation, the calculation only involves single and two-particle correlation functions of the reference system and no ‘‘amputated’’ quantities. The reduced number of matrix inversions makes it suitable for multi-orbital systems. The case of the ‘‘bare dual fermions’’ $\tilde{\Sigma}_{\mathbf{k}\nu} = 0$ is equivalent to the cluster perturbation theory [44].

2.2 Perturbation in dual space

The cluster dual fermion perturbation theory (Fig. 2.1) starts with the interaction between dual fermions. We use here the particle-hole notation for the local vertex and write explicit spin indices and Matsubara frequency structure of the connected two particle Green's function[108, 47] as follows:

$$\begin{aligned}
-\gamma_{1234}^{\sigma\sigma'}(\nu, \nu', \omega) &= \langle c_{1\sigma}(\nu)c_{2\sigma}^*(\nu + \omega)c_{3\sigma'}(\nu' + \omega)c_{4\sigma'}^*(\nu') \rangle_{\Delta} - \\
&\quad - \beta g_{12}^{\sigma}(\nu)g_{34}^{\sigma'}(\nu')\delta_{\omega 0} + \\
&\quad + \beta g_{14}^{\sigma}(\nu)g_{32}^{\sigma}(\nu + \omega)\delta_{\nu\nu'}\delta_{\sigma\sigma'}.
\end{aligned} \tag{2.19}$$

In Matsubara space, the vertex depends on two fermionic (ν, ν') and one bosonic (ω) frequencies. For the sake of completeness and the reader's convenience we mention that the connection between the particle-particle and the particle-hole notation is $\gamma_{1234}(\nu, \nu', \omega) = \gamma_{1342}^P(\nu, \nu', \nu + \nu' + \omega)$ with the particle-particle frequency notation being $\kappa_{1234}^P(\nu, \nu', \omega) = \langle c_1(\nu)c_2(\omega - \nu)c_4^*(\omega - \nu')c_3^*(\nu') \rangle_{\Delta}$. Thus, the bare vertex of the dual fermion perturbation theory is the full connected correlation function of the reference system. The present vertex differs from the usual dual fermion expression due to the different rescaling factor of the Hubbard-Stratonovich field. Here, we avoid amputation of the legs of the vertex, which requires division by Green's functions at all external points.

It is useful to symmetrize the vertex into charge density (d) and magnetic (m) channels:

$$\gamma_{1234}^{d/m}(\nu, \nu', \omega) = \gamma_{1234}^{\uparrow\uparrow}(\nu, \nu', \omega) \pm \gamma_{1234}^{\uparrow\downarrow}(\nu, \nu', \omega)$$

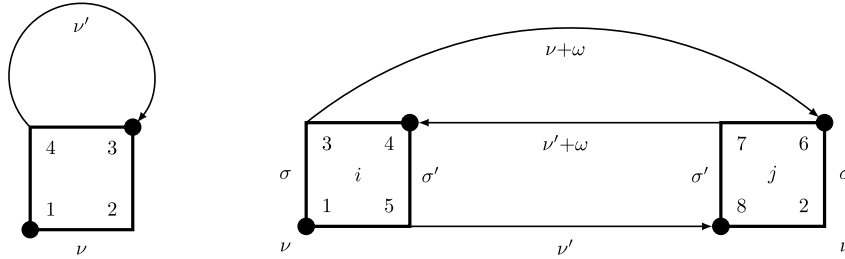


FIGURE 2.2: Feynman diagram for the first order (left) and the second order (right) dual fermion perturbation for the self-energy $\tilde{\Sigma}$: a line represents the non-local \tilde{G}_{43} and a box is the local γ_{1234} .

Now we can write the first-order dual fermion self-energy which is local in plaquette space (Fig. 2.2):

$$\tilde{\Sigma}_{12}^{(1)i}(\nu) = \sum_{\nu', 3, 4} \gamma_{1234}^d(\nu, \nu', 0) \tilde{G}_{43}^{ii}(\nu') \quad (2.20)$$

The second order Feynman diagram for DF-perturbation (Fig. 2.2) in real space (\mathbf{R}_{ij}) has density- and magnetic-channel contributions with corresponding constants ($c_d = -\frac{1}{4}$ and $c_m = -\frac{3}{4}$):

$$\tilde{\Sigma}_{12}^{(2)ij}(\nu) = \sum_{\nu' \omega} \sum_{3-8} \sum_{\alpha=d,m} c_\alpha \gamma_{1345}^{\alpha,i}(\nu, \nu', \omega) \tilde{G}_{36}^{ij}(\nu + \omega) \tilde{G}_{74}^{ji}(\nu' + \omega) \tilde{G}_{58}^{ij}(\nu') \gamma_{8762}^{\alpha,j}(\nu', \nu, \omega) \quad (2.21)$$

In principle, one can go beyond the second order perturbation expansion and include dual ladder diagrams [49, 47], dual parquet diagrams[75] or a stochastic sum of all dual diagrams with the two-particle vertex γ_{1234} , using diagrammatic Monte Carlo in dual space [64, 45, 128]. In addition, the diagrammatic series can be made self-consistent, using dual skeleton diagrams and “bold” lines. Finally, one can also update the reference system (and obtain a frequency dependent Δ) with quite involved numerical approach. But as the main goal of the present work is not to present quantitatively reliable results but rather to highlight the connection between the degenerate reference system and the superconducting fluctuations we will mostly stick to the second-order consideration. We used two independent implementations of the Dual Fermion method, one of which is discussed in Section 2.5, which gave the ability to cross-check the results. The vertex function γ using a Fortran implementation of dual fermions that uses the equivalence of the four sites in the plaquette to speed up the vertex calculation.

2.3 Exact relation for Green’s function

After appropriate diagrammatic results for the dual self-energy and the dual Green’s function has been obtained, it has to be transformed back to the corresponding physical quantities in terms of real lattice fermions. The fact that dual fermions are introduced through the exact Hubbard-Stratonovich transformation Eq. (2.5) allows to establish exact identities between dual and lattice Greens function [108, 47].

We can establish the relations between the n -particle cumulants of dual and lattice fermions using the cumulant (linked cluster) technique, by considering two different,

equivalent representations of the following generating functional:

$$e^{F[J^*J, L^*L]} = \mathcal{Z}_d \int \mathcal{D}[c^*c, d^*d] e^{-S[c^*c, d^*d] + J_1^*c_1 + c_2^*J_2 + L_1^*d_1 + d_2^*L_2} \quad (2.22)$$

Integrating out the lattice fermions from this functional similar to (2.9) (this can be done with the sources J and J^* set to zero) yields

$$e^{F[L^*, L]} = \tilde{\mathcal{Z}}_d \int \mathcal{D}[d^*, d] e^{-S_d[d^*, d] + L_1^*d_1 + d_2^*L_2} \quad (2.23)$$

with $\tilde{\mathcal{Z}}_d = \mathcal{Z}/\tilde{\mathcal{Z}}$. We obtain the dual Green's function and two-particle correlator related with non-local susceptibilities from (2.23) by suitable functional derivatives, e.g.

$$\tilde{G}_{12} = - \left. \frac{\delta^2 F}{\delta L_2 \delta L_1^*} \right|_{L^*=L=0} \quad (2.24)$$

Integrating out the dual fermions from Eq.(2.22) using the HST, we obtain an alternative representation, which more clearly reveals a connection of the functional derivatives with respect to the sources J, J^* and L, L^* . The result is

$$F[J^*J, L^*L] = -L_1^*(t - \Delta)_{12}L_2 + \ln \int \mathcal{D}[c^*, c] \exp \left(-S[c^*, c] + J_1^*c_1 + c_2^*J_2 - L_1^*(t - \Delta)_{12}c_2 - c_1^*(t - \Delta)_{12}L_2 \right). \quad (2.25)$$

In analogy to (2.24), we obviously obtain the cumulants in terms of lattice fermions by functional derivative with respect to the sources J and J^* with L and L^* set to zero. Applying the derivatives with respect to L, L^* to (2.25) with $J = J^* = 0$ and comparing to (2.24), e.g. yields the following identity:

$$G_{12} = -(t - \Delta)_{12}^{-1} + (t - \Delta)_{11'}^{-1} \tilde{G}_{1'2'} (t - \Delta)_{2'2}^{-1}. \quad (2.26)$$

Solving for G provides the rule how to transform the dual Green's function to the physical quantity in terms of lattice fermions.

2.4 Plaquette periodization

The separation of the original lattice into plaquettes breaks the translational symmetry, because bonds within a plaquette are treated differently from bonds between plaquettes. In order to write all quantities in terms of the momentum \mathbf{k} in the Brillouin Zone of the original lattice, we need to restore the full translational symmetry.

Let us discuss a periodization of plaquette self-energy $\Sigma_{ij}(\mathbf{r}, \nu)$ Eq. (2.17) where $\mathbf{r} \equiv (r_x, r_y)$ is the supercell translation and i, j are cluster sites (see Fig.(2.3)). The latter can be alternatively described by intra-plaquette translation vectors \mathbf{i}, \mathbf{j} taking values $[(0, 0), (0, 1), (1, 1), (1, 0)]$ for the site indices 0 to 3 respectively. We would like to get a lattice periodic self-energy $\Sigma(\mathbf{R}, \nu)$ where $\mathbf{R} \equiv (R_x, R_y)$ is the original square lattice translations. By construction Σ is periodic in \mathbf{r} , but not in \mathbf{R} . The natural periodization procedure would be taking all four possible values of $\mathbf{i} \equiv (i_x, i_y)$ and average over them for a given value of \mathbf{R} . This is done straightforwardly with a minor technical challenge of determining the supercell translation \mathbf{r} and final site index \mathbf{j} that correspond to a given value of lattice translation \mathbf{R} and initial site index \mathbf{i} . By recasting

$$\mathbf{i} + \mathbf{R} \equiv (i_x + R_x, i_y + R_y) = (2[(i_x + R_x)/2] + 2\{(i_x + R_x)/2\}, 2[(i_y + R_y)/2] + 2\{(i_y + R_y)/2\}), \quad (2.27)$$

and noticing that $\mathbf{i} + \mathbf{R} = \mathbf{j} + 2\mathbf{r}$, we immediately find $\mathbf{r}(\mathbf{i}, \mathbf{R}) = ([i_x + R_x]/2, [(i_y + R_y)/2])$ and $\mathbf{j}(\mathbf{i}, \mathbf{R}) = (2\{(i_x + R_x)/2\}, 2\{(i_y + R_y)/2\})$. Here $[x]$ and $\{x\}$ are the integer and fractional parts of x respectively. Finally for the periodized self-energy we take

$$\Sigma(\mathbf{R}, \nu) = \frac{1}{4} \sum_{\mathbf{i}} \Sigma_{ij(\mathbf{i}, \mathbf{R})}(\mathbf{r}(\mathbf{i}, \mathbf{R}), \nu), \quad (2.28)$$

with the sum being taken over four cluster sites.

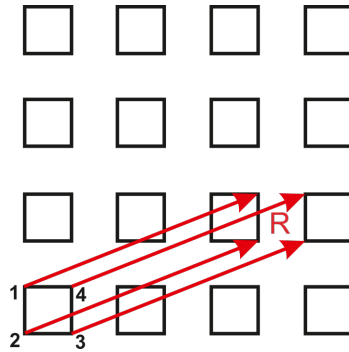


FIGURE 2.3: Scheme for the real-space periodization of the 2×2 plaquette lattice.

2.5 Implementation: Multiorbital DF

The “Multiorbital DF” solver is an implementation of the Dual Fermion method according to [66, 51], which is able to solve an arbitrary system of clusters connected by momentum-space hopping. The program was tested by cross-checking the output with the Fortran implementation of Dual Fermion method during the Dual Fermion study of the 2×2 plaquette. It is still in development and will be made available at [103] after completion.

The method takes as inputs the following data:

- momentum-space hopping $\hat{t}_{\mathbf{k}}$ and the chemical potential μ ;
- from cluster model: self-energy $\Sigma_{\nu 12}^0$ and Green’s function $g_{\nu 12}$, bare vertex function $\gamma_{1234}^{\sigma\sigma'}(\nu, \nu', \omega)$.

The bare dual Green’s function \tilde{G}^0 is computed using Eq. 2.16, with our choice of the hybridization function being

$$\hat{\Delta}_{\nu 12} = (\nu + \mu)I_{12} - \Sigma_{\nu 12}^0 - (g_{\nu})_{12}^{-1}. \quad (2.29)$$

The dual Green’s function is initially set $\tilde{G} = \tilde{G}^0$.

First- and second-order self-energies are calculated with corresponding Eq. 2.20 and Eq. 2.21 and summed

$$\tilde{\Sigma} = \tilde{\Sigma}^{(1)} + \tilde{\Sigma}^{(2)}.$$

Bethe-Salpeter matrices $\Lambda^{P/d/m}$ (Eq. 4.3) are intermediate result of the multiplication of $\gamma^{P/d/m}$ and two G functions in Eq. 2.21.

Optionally, the calculation can be run without the second-order self-energy and Bethe-Salpeter matrices.

Lattice self-energy is computed with Eq. 2.17, and local lattice self-energy

$$\Sigma_{(\mathbf{K}+\mathbf{k})\nu}^{\text{loc}} = \frac{1}{N_c} \sum_{12} \Sigma_{\mathbf{k}\nu 12} e^{-i(\mathbf{K}\mathbf{r}_1 - \mathbf{K}\mathbf{r}_2)}. \quad (2.30)$$

The simplest form of self-consistency, so called *boldening* of the dual Green’s function, is implemented by updating \tilde{G} with the Dyson equation

$$\tilde{G}_{12\mathbf{k}\nu} = [\tilde{G}_{0\mathbf{k}\nu}^{-1} - \tilde{\Sigma}_{\mathbf{k}\nu}]_{12}^{-1} \quad (2.31)$$

and re-running the procedure starting from the calculation of $\tilde{\Sigma}^{(1,2)}$.

Part II

Study of the two-dimensional Hubbard model

Chapter 3

Exact Diagonalization of 2×2 Hubbard plaquette

The Hubbard model introduced in 1963 by J. Hubbard [60] to describe electrons in 3d transition metal oxides is one of the most universal models used for studying systems with strong electron-electron correlations. This simple model is important in theoretical physics because it can describe a number of phenomena such as superconductivity, metal-insulator transition, antiferromagnetism and ferrimagnetism. It can be used to solve the many-body problem in terms of valent localized states, for which density functional theory (DFT) would break down. In the simplest case this subspace consists of one level per magnetic ion which, according to the Pauli principle, can be either empty, occupied by one electron with the spin up, by one electron with the spin down, or two electrons with opposite spins. The Hamiltonian of such model is

$$\mathcal{H} = \sum_{i \neq j, ss'} t_{ij}^{ss'} c_{is}^{\dagger} c_{js'} + \frac{1}{2} \sum_{ijklss'} U_{ijkl} c_{is}^{\dagger} c_{js'}^{\dagger} c_{ls'} c_{ks} - \mu \sum_{is} n_{is}, \quad (3.1)$$

where U_{ijkl} is the matrix element of Coulomb interaction, $t_{ijss'}$ is the hopping integral between sites i and j with corresponding spins s and s' , μ is chemical potential, $c_{is}^{(+)}$ and $n_{is} = c_{is}^{\dagger} c_{is}$ are, correspondingly, electron annihilation (creation) and number of particles operators on site i with the spin s .

The 2×2 *plaquette* is a two-dimensional Hubbard cluster consisting of 4 single-orbital sites with Coulomb interaction U , with nearest neighbour (vertical and horizontal) hoppings t and next-nearest neighbour (diagonal) hopping t' (see Fig. 3.1). Optionally there is a periodic boundary condition, in which case it should be noted that in resulting Hubbard hamiltonian the effective hoppings $t_{\text{eff}} = 2t$ and $t'_{\text{eff}} = 4t'$, because they are summed with the same indices as internal hoppings.

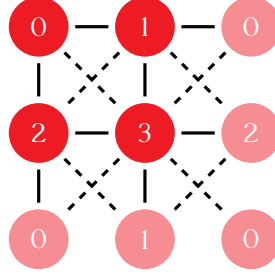


FIGURE 3.1: 2×2 plaquette with periodic boundary condition. The circles represent sites with Coulomb interaction U , solid lines hopping t , dashed lines hopping t' .

Hole or electron doping corresponding to Hamiltonian sectors is defined as

$$\delta = \frac{|N - N_s|}{N_s}, \quad (3.2)$$

where $N = N_\uparrow + N_\downarrow$ is the total number of electrons and N_s is the number of sites. For example, for $N_s = 16$ half-filling $(N_\uparrow, N_\downarrow) = (8_\uparrow, 8_\downarrow)$ is undoped $\delta = 0$, sectors $(7_\uparrow, 6_\downarrow)$ and $(6_\uparrow, 7_\downarrow)$ correspond to hole doping $\delta = 0.1875$, sector $(7_\uparrow, 7_\downarrow)$ to hole doping $\delta = 0.125$, sector $(9_\uparrow, 9_\downarrow)$ to electron doping $\delta = 0.125$, etc.¹

Harland et al. [53] suggest that the 2×2 plaquette in the so-called effective t, t' Hubbard model is the minimal and generic consistent electronic structure model of the theory of high-temperature cuprate superconductors [7, 101], rather than the conventional atomic limit typical for the theory of Mott insulators [10, 62]. From band-structure calculations [7, 101] the Hubbard model can be safely reduced to an effective one-band model with nearest- and next-nearest-neighbor hopping

$$\mathcal{H} = \sum_i U_i n_{i\uparrow} n_{i\downarrow} - \mu \sum_{is} n_{is} + \sum_{i \neq j, s} t_{ij} c_{is}^\dagger c_{js}, \quad (3.3)$$

which with a standard parametrization of the tight-binding model for $\text{YBa}_2\text{Cu}_3\text{O}_7$ [7, 101] would have $t'/t = -0.3$ and t as the unit of energies. The Coulomb interaction U is on the order of the bandwidth $W = 8t$. This system experiences an energy spectrum peculiarity, namely, the highly degenerate point merging two singlets and two doublets, which is related to the formation of local valence bonds in the frustrated quantum spin model [3].

The convention used throughout this study is $t = -1$, $U > 0$ and $t' \geq 0$ ($t'/t \leq 0$).

¹In the absence of the magnetic field term $\mathcal{H}_{\text{mag}} = H(n_{i\uparrow} - n_{i\downarrow})$, where H is the magnetic field intensity, the Hamiltonian favours minimal difference $|N_\uparrow - N_\downarrow|$, so we will only consider sectors with $|N_\uparrow - N_\downarrow| \leq \pm 1$ throughout this work.

3.1 Phase diagrams

For different values of t' , U , μ , ground state of the model corresponds to a certain number of electrons. This dependency can be represented as a phase diagram in the space of U and μ for a fixed t' . On phase boundaries the ground state is at least two times degenerate, consisting of states with two different number of electrons. On triple points it is at least three times degenerate, consisting of states with three different numbers of electrons.

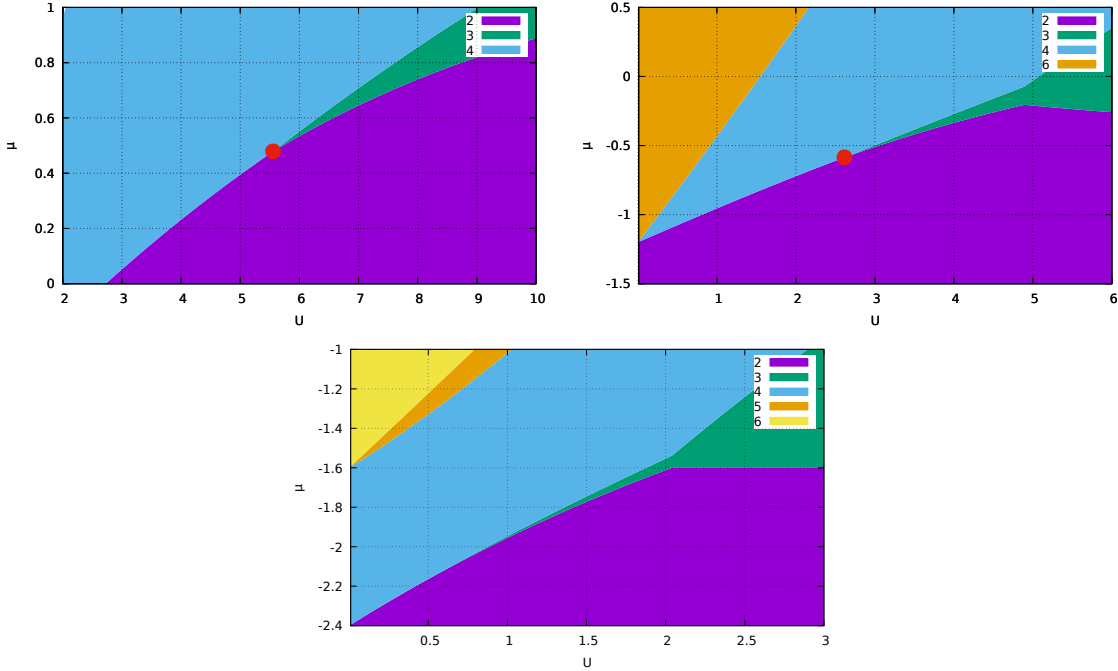


FIGURE 3.2: Number of electrons in the ground state of periodic 2×2 plaquette.

Top left: $t' = 0.15$, triple point at $U = 5.555$, $\mu = 0.479$;

Top right: $t' = 0.3$, triple point at $U = 2.615$, $\mu = -0.585$;

Bottom: $t' = 0.6$, no triple point.

The phase diagram for $t' = 0.15$ (Fig. 3.2) reproduces the one presented in the original article about the plaquette [53], with the triple point $U = 5.56$, $\mu = 0.479$ corresponding to $U = 2.78$, $\mu = 0.24$ of the original with $t = 0.3$.²

²This change of the values is due to the explicit accounting for the plaquette's periodicity in our definition of Hamiltonian (see the note about periodic boundary after Fig. 3.1), because of which we have to take $t' = 0.15$ instead of the original $t' = 0.3$ to have the same relation $t'_{\text{eff}}/t_{\text{eff}} = -0.3$ apply to our parameters, and then the resulting U and μ are twice the original ones.

In the triple point, the ground state is 6-fold degenerate, with 1 state from sectors $(2_\uparrow, 2_\downarrow)$ and $(1_\uparrow, 1_\downarrow)$ each, and 2 states from $(2_\uparrow, 1_\downarrow)$ and $(1_\uparrow, 2_\downarrow)$ each.

The following procedure was used to calculate the phase diagram of total number of electrons $N = N_\uparrow + N_\downarrow$. For each U ,

1. The low-energy E_N is obtained for each total number of electrons N using Exact Diagonalization solver, with $\mu = 0$.
2. For all possible pairs of N , their “intersection” μ_{int} , at which the low-energy states of sectors overtake each other, is found at which $E_{N_1} - \mu_{\text{int}}N_1 = E_{N_2} - \mu_{\text{int}}N_2$ or $\mu_{\text{int}} = (E_{N_1} - E_{N_2})/(N_1 - N_2)$.
3. Energies for all N are calculated for the minimum μ under consideration, and the ground state is determined.
4. Starting from this ground state, μ_{int} are used to determine the sequence of N changing as μ increases.

3.2 Dynamical averages in momentum space

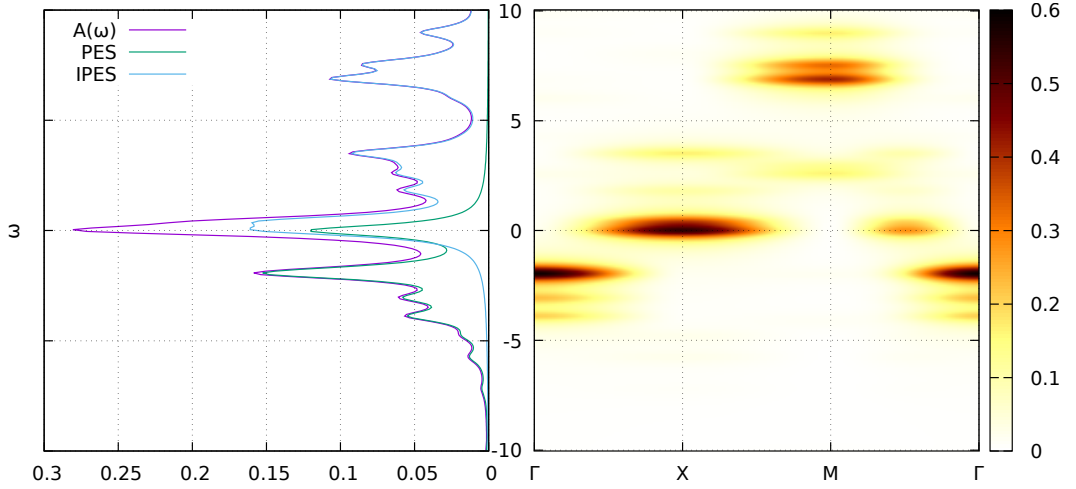


FIGURE 3.3: Exact Diagonalization density of states $A(\omega)$ (left), \mathbf{k} -resolved spectral density $A(\mathbf{k}, \omega)$ (right) in the Brillouin zone 64×64 \mathbf{k} -mesh of periodic 2×2 plaquette with $t' = 0.15$, $U = 5.56$, $\mu = 0.479$, $\beta = 10$.

The momentum dependence of the self-energy on the lowest Matsubara frequency (Fig. 3.4) and \mathbf{k} -resolved spectral density (Fig. 3.3) have been calculated in the triple point of the 2×2 plaquette.

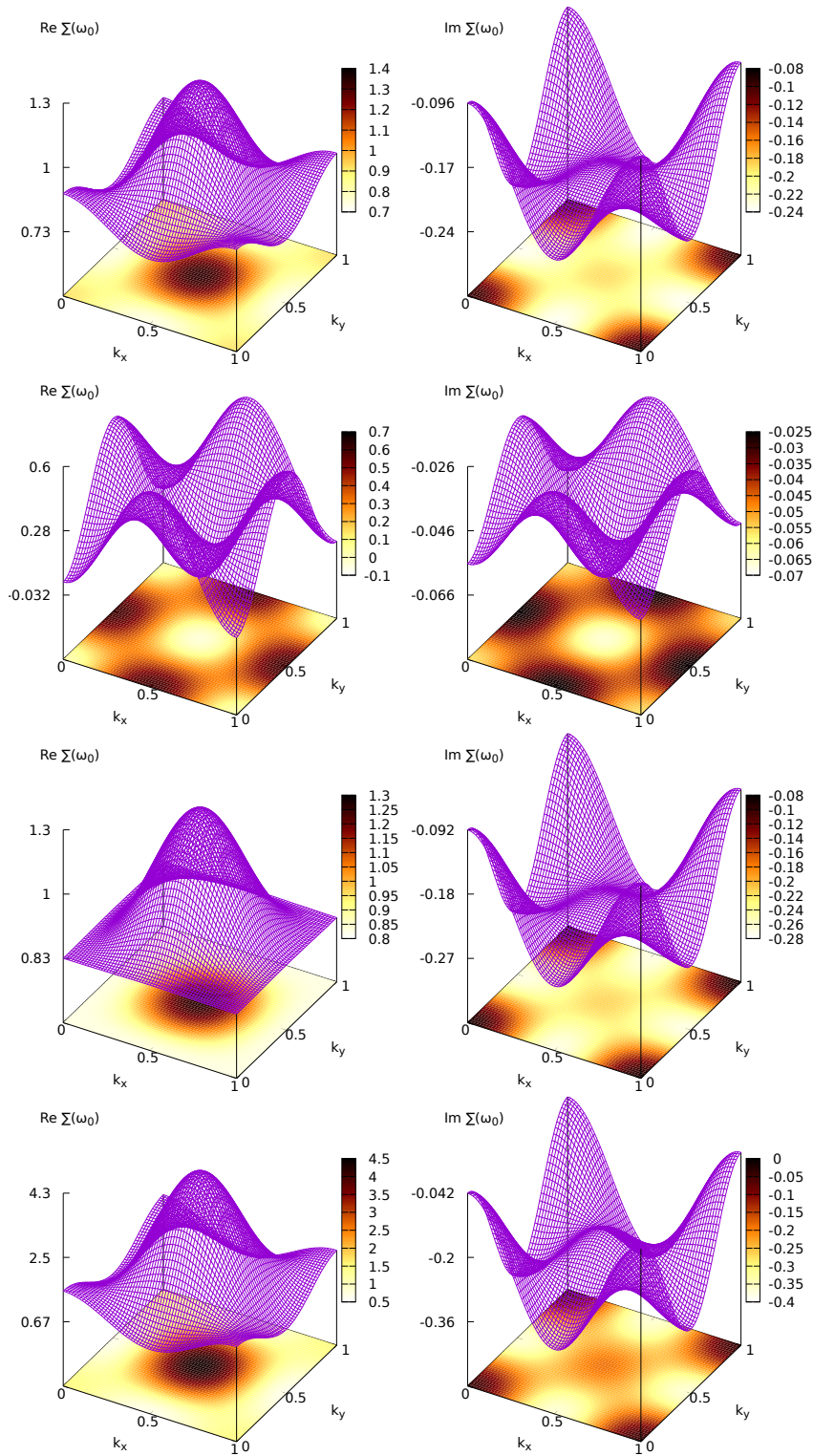


FIGURE 3.4: Exact Diagonalization self-energy $\Sigma(\mathbf{k}, i\omega_0)$ in the full Brillouin zone 64×64 \mathbf{k} -mesh on the lowest Matsubara frequency $i\omega_0$ of periodic 2×2 plaquette with $t' = 0.15$, $U = 5.56$, $\mu = 0.479$, $\beta = 10$.

Top to bottom: for full Hamiltonian, for sector $(1_\uparrow, 1_\downarrow)$, sectors $(2_\uparrow, 1_\downarrow)$ and $(1_\uparrow, 2_\downarrow)$, sector $(2_\uparrow, 2_\downarrow)$.

To calculate the observables in the momentum space we take Fourier transform of the ED results, for example for the Green's function:

$$G_k(\omega) = \frac{1}{N_s} \sum_{ij} G_{ij}(\omega) e^{-i\mathbf{k}(\mathbf{r}_i - \mathbf{r}_j)}, \quad (3.4)$$

where the \mathbf{r}_i and \mathbf{r}_j are the cluster coordinate vectors of sites i and j , and N_s is the number of sites.

Chapter 4

Dual Fermion study of 2×2 plaquette

After 35 years since the discovery of the high-temperature superconductivity [18], there is still no consensus on the nature of the mechanism of d-wave pairing in cuprates [114, 37, 70, 67, 104]. Nevertheless, new experimental findings clearly point to the existence of a quantum critical point around a hole doping of $\delta \approx 0.24$ [102, 12, 25]. This concentration separates the exotic bad-metal state for smaller doping from Fermi-liquid behaviour for larger hole concentration with “normal” Fermi-surface described, at least qualitatively, by conventional density-functional theory [6]. Moreover, the carrier density obtained from Hall effect measurements in large-doping regime is equal to its nominal value $n_H \approx 1 - \delta$ while for smaller doping the bad-metal behaviour appears with Fermi-arcs, “enigmatic pseudogap phase” and ($n_H \approx \delta$) at high temperature [102, 24]. Recent investigations of highly overdoped cuprates show that this “strange metal phase” is located around $\delta_c \approx 0.24$ point [12]. For hole concentrations less than δ_c superconducting pairs come entirely from the region of incoherent electrons at the antinode region (X -point) of the Brillouin zone (Planckian dissipators) [12].

Normal-state electronic specific heat measurements for many different cuprate superconductors in a normal phase reveal a huge peak in the electron Density of States (DOS) at the Fermi energy at $\delta_c \approx 0.24$ with a strong evidence of the presence of a Quantum Critical Point (QCP) at this hole doping [102]. Taking into account this critical concentration as a fingerprint of high- T_c materials, we will use the cluster dual-fermion superperturbation theory [106], Exact Diagonalization and Complex Network Theory to model the electronic instability.

First-principle electronic structure calculations [6] suggest that a single-band tight-binding model with next nearest neighbour (NNN) hopping and on-site Coulomb interaction, the so-called “ $t - t' - U$ ” Hubbard model, has all ingredients to describe high- T_c phenomena. Moreover, the case of $t'/t = -0.15$ corresponds to the LSCO-cuprate family while one expects $t'/t = -0.3$ to describe cuprate families with higher T_c such as e.g. YBCO and Tl2201 [101]. We developed an efficient second-order perturbation theory starting from a 2×2 plaquette, where $\delta = 0.25$ corresponds to

a highly degenerate point for $U/t \approx 6$ [53]. In a close analogy with the Kondo model, where the degeneracy of the two spin states of a magnetic impurity plays a crucial role in the anomalous low-energy properties, the special properties of the degenerate states of the plaquette can reveal the nature of the anomalous behavior of the interacting Hubbard model on a two-dimensional lattice.

The first attempt to discuss the plaquette physics as the main ingredient of the high-Tc theory was done with the cluster dynamical mean-field theory (DMFT) scheme [78], and later Altman and Auerbach analytically explained the importance of plaquette two-hole states with $d_{x^2-y^2}$ symmetry [5]. Nevertheless they did not consider the possibility of a degenerate ground state of the plaquette [53] with a correspondingly divergent perturbation series similar to the perturbative theory in Kondo problem [57]. In some sense, the degeneracy of the ground states with $N = 2, 3, 4$ electrons per plaquette in the critical point plays the same role as the degeneracy between spin-up and spin-down states in the conventional Kondo effect and is crucially important for the pseudogap formation [53]. If we treat the Kondo problem in dual perturbation from the atomic limit [76] then the local four-point vertex is divergent at low temperature, while the Green's function is finite. In the case of degenerate plaquette both Green's function for reference system and vertex are divergent for low temperature.

We will start here with this six-fold degenerate ground state of a 2×2 plaquette with t'/t fixed to -0.15 depicted as a star-point in the Fig. 4.1. Since we use here periodic boundary conditions the critical Coulomb interaction becomes $U/t = 5.56$ in contrast with the case of isolated plaquette [53]. This is in a very good agreement with the value of the Coulomb interaction $U/t = 5.6$ that was found in the diagrammatic Monte Carlo calculations [132] in a search of pseudogap formation, and the value of $U/t \approx 6$ pointed out in the recent review [102] as the most reasonable value of the effective Hubbard interaction for cuprates. Note also that periodic boundary conditions effectively double t' compared to t , which explains the chosen value of the NNN hopping twice smaller than in Ref. [53]. At a special value of the chemical potential [53] $\mu \approx 0.48$ the ground state for the half-filled $N = 4$ antiferromagnetic singlet is degenerate with the singlet for $N = 2$ electrons and with two doublets from $N = 3$ sector. For these values of the parameters the plaquette state corresponds to the hole doping of $\delta_c = 0.25$. If we start from such a degenerate point as a reference system, any perturbation theory for the lattice will be highly divergent.

We will also consider reference systems differing from the degenerate point in the value of the chemical potential. For smaller $\mu \approx 0$ (marked with the circle in Fig. 4.1) the lattice would tend to a metallic behavior, for larger $\mu \approx 0.8$ (marked with the square) the perturbation for the lattice results in a superconducting $d_{x^2-y^2}$ instability.

Facing such a complex system that is hard to solve exactly, it is frequently useful to consider solvable reference systems instead. This strategy is the basis for variational and mean-field approaches, among others. The simplest exactly solvable model is based on infinite-dimensional case with a plaquette as elementary unit (cluster DMFT) [52]. However, nonlocal correlations effects should be relevant for the low-dimensional systems which means that we have to go beyond this limiting case. In electronic systems, the dual fermion [108] approach provides a recipe for using arbitrary local reference systems [20], with a way to incorporate nonlocal corrections in a systematic fashion. There is a large amount of freedom in choosing this reference system which can be used to capture essential physics of the full system under investigation.

In the case of the doped $t-t'-U$ Hubbard model, d-wave superconducting fluctuations are known to be important, and a four-site plaquette is the minimal reference system that contains their spatial structure and additionally has an important degenerate point [53, 13]. Below we show that this degenerate point also induces clear signatures in the two-particle correlation function, which is the basic building block of the dual fermion perturbation theory.

The central question for a reliable theory of the high-Tc cuprates can be formulated in the following manner: what is the mechanism of superconducting coupling and which minimal model explains the key experimental observations such as nodal-antinodal dichotomy and pseudogap formation in the underdoped regime, strange metal behaviour, etc.? An important part of that question is: what is the minimal length scale needed to understand these phenomena? For the Mott insulating phase, a single atom with Coulomb interaction, coupled to a (dynamical) bath, is qualitatively sufficient. Extending this to a single bond explains how antiferromagnetic exchange interactions between local moments emerge. It has been argued, starting from Ref. [78], that a plaquette consisting of 2×2 sites is the minimal unit when thinking about d-wave superconductivity: it is sufficiently large to express the phase difference in the horizontal and vertical direction that characterizes d-wave superconductivity. The $t-t'-U$ plaquette is known to have a critical line of degenerate states in parameter space of (U, t', μ) [13]. We will argue that, similar to how the generation of antiferromagnetic exchange on a single bond forms the starting point for antiferromagnetism, this plaquette degeneracy plays a central role in the origin of d-wave superconductivity.

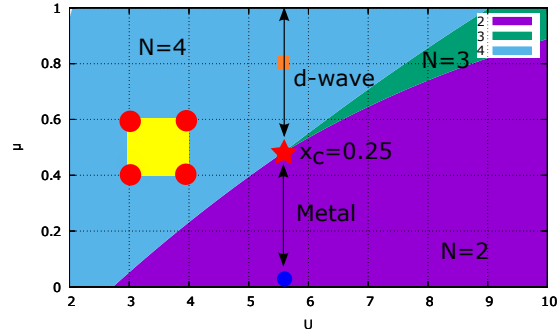


FIGURE 4.1: Phase diagram of 2×2 plaquette with the degenerate point marked by star. The region of $d_{x^2-y^2}$ superconducting phase and normal metal for square lattice are also marked.

4.1 Results for plaquette dual scheme

We study the optimally doped square lattice Hubbard model, with nearest neighbour hopping t and NNN hopping t' . As illustrated in Fig. 2.1, the original lattice can be reconsidered as a lattice of 2×2 plaquettes. Every unit cell of the plaquette lattice contains 4 atoms of the original lattice, as shown on the left-hand side of Fig. 2.1. The plaquette lattice has the following 4×4 hopping matrix (see Fig. 2.1), with the numbering of sites shown on Fig. 4.2:

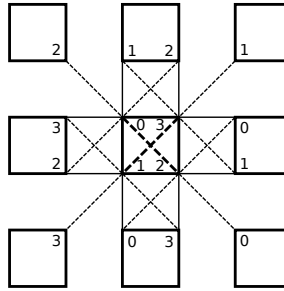


FIGURE 4.2: Hubbard plaquettes connected by momentum-space hoppings. Thick lines: hoppings inside the plaquette, thin lines: k-space hoppings.

$$\begin{aligned}
t_{\mathbf{k}} &= \begin{pmatrix} \varepsilon & t & t' & t \\ t & \varepsilon & t & t' \\ t' & t & \varepsilon & t \\ t & t' & t & \varepsilon \end{pmatrix} + \\
&+ \begin{pmatrix} 0 & 0 & 0 & 0 \\ 0 & 0 & 0 & t' \\ 0 & 0 & 0 & 0 \\ 0 & 0 & 0 & 0 \end{pmatrix} e^{i(k_x - k_y)} + \begin{pmatrix} 0 & 0 & 0 & 0 \\ 0 & 0 & 0 & 0 \\ 0 & 0 & 0 & 0 \\ 0 & t' & 0 & 0 \end{pmatrix} e^{i(k_x + k_y)} + \\
&+ \begin{pmatrix} 0 & 0 & t' & 0 \\ 0 & 0 & 0 & 0 \\ 0 & 0 & 0 & 0 \\ 0 & 0 & 0 & 0 \end{pmatrix} e^{i(-k_x + k_y)} + \begin{pmatrix} 0 & 0 & 0 & 0 \\ 0 & 0 & 0 & 0 \\ t' & 0 & 0 & 0 \\ 0 & 0 & 0 & 0 \end{pmatrix} e^{i(k_x - k_y)} + \\
&+ \begin{pmatrix} 0 & 0 & t' & t \\ 0 & 0 & t & t' \\ 0 & 0 & 0 & 0 \\ 0 & 0 & 0 & 0 \end{pmatrix} e^{-ik_x} + \begin{pmatrix} 0 & 0 & 0 & 0 \\ 0 & 0 & 0 & 0 \\ t' & t & 0 & 0 \\ t & t' & 0 & 0 \end{pmatrix} e^{ik_x} + \\
&+ \begin{pmatrix} 0 & 0 & 0 & 0 \\ t & 0 & 0 & t' \\ t' & 0 & 0 & t \\ 0 & 0 & 0 & 0 \end{pmatrix} e^{-ik_y} + \begin{pmatrix} 0 & t & t' & 0 \\ 0 & 0 & 0 & 0 \\ 0 & 0 & 0 & 0 \\ 0 & t' & t & 0 \end{pmatrix} e^{ik_y} = \\
&= \begin{pmatrix} \varepsilon & tK^{0+} & t'L^{-+} & tK^{-0} \\ tK^{0-} & \varepsilon & tK^{-0} & t'L^{--} \\ t'L^{+-} & tK^{+0} & \varepsilon & tK^{0-} \\ tK^{+0} & t'L^{++} & tK^{0+} & \varepsilon \end{pmatrix}, \tag{4.1}
\end{aligned}$$

where the functions $K_{\mathbf{k}}^{mn}$ and $L_{\mathbf{k}}^{mn}$, with $m, n \in \{-1, 0, +1\}$, are defined as

$$\begin{aligned}
K_{\mathbf{k}}^{mn} &= 1 + e^{i(mk_x + nk_y)} \\
L_{\mathbf{k}}^{mn} &= 1 + e^{i(mk_x + nk_y)} + e^{imk_x} + e^{ink_y}
\end{aligned}$$

We will use a single plaquette as the reference system. Compared to the single-site dual fermion formalism, this plaquette reference system already encompasses the short-ranged correlations that are essential in this system.

In the dual fermion approach, there is a general freedom of choosing the most appropriate reference system. One way to construct a plaquette reference system would be to simply remove all black links in Fig. 2.1 (and attach the remaining sites to a bath). This is equivalent to the self-consistent cluster-DMFT scheme [78] and corresponds to averaging over the supercell Brillouin zone. This scheme eliminates exactly half of the nearest-neighbor hoppings and three quarters of the next-nearest-neighbor hoppings.

Here we choose another path and consider plaquettes with periodic boundary conditions as a static reference system. In terms of the supercell Brillouin zone, this corresponds to achieving self-consistency for $k = 0$ only, instead of the momentum

average. The intra-plaquette hopping is

$$\Delta_0 \equiv t_{\mathbf{k}=0} = \begin{pmatrix} \varepsilon_0 & 2t & 4t'_0 & 2t \\ 2t & \varepsilon_0 & 2t & 4t'_0 \\ 4t'_0 & 2t & \varepsilon_0 & 2t \\ 2t & 4t'_0 & 2t & \varepsilon_0 \end{pmatrix}. \quad (4.2)$$

Note that we include the possibility of using a different chemical potential $\mu_0 = -\varepsilon_0$ in the reference system, compared to that of the lattice model $\mu = -\varepsilon$ to adjust the hole doping. We fix the nearest neighbour hopping t but retain the freedom of adjusting the next nearest neighbour hopping t' in the dual fermion transformation. For example this may be used to reduce the factor 4 for the t' hoppings for the periodic boundary conditions (see the remark for Fig. 3.1) for 2×2 plaquette if we chose $t'_0 = t'/2$.

With the plaquette as the reference system, one can use the exact diagonalization approach to calculate the dual Green's function and the plaquette vertex function[48]. We choose the optimal parameters for the High- T_c cuprates where the ground state of the plaquette is six-fold degenerate[53] with $U = 5.56$, $t = -1$, $t'_0 = 0.15$ $\mu_0 = 0.48$ with $t' = 0.15$ or 0.3 and $\mu = 0.7$ or 1.5 correspondingly to keep the optimal doping $\delta \approx 0.15$ in the lattice. We investigate different temperatures as low as possible until the dual perturbation theory breaks down due to the divergence in the plaquette vertex function at the degenerate point in the limit $T \rightarrow 0$.

In the Fig. 4.3 we compare the density of states (DOS) for plaquette DF second-order perturbation (DF2) with the so-called cluster perturbation theory (CPT) which corresponds to zero dual-self energy in Eq.(2.18) for quite high temperature ($\beta = 3$). We use Padé-analytical continuation from Matsubara to the real energy axes[42]. One can see that the DOS for the dual fermion theory is much more sharply peaked near the Fermi level compared to the CPT-result. For comparison we also show the ED result for the plaquette with a sharp peak exactly at Fermi level due to six-fold degenerate ground state. In this case there is still no signature for a pseudogap and the lattice self-energy is “well-behaved”.

4.1.1 Vertex and Bethe–Salpeter Equation

The central idea of starting from an appropriate reference system, is that the exact solution of the latter already contains the essential correlations of the original system. These manifest themselves on the one-particle level (g) but especially also on the two-particle level. Recent studies have illustrated the value of the information encoded in vertices and susceptibilities [107, 115, 73, 74, 52, 119, 92, 82, 105, 22] even in the case of a single-orbital model.

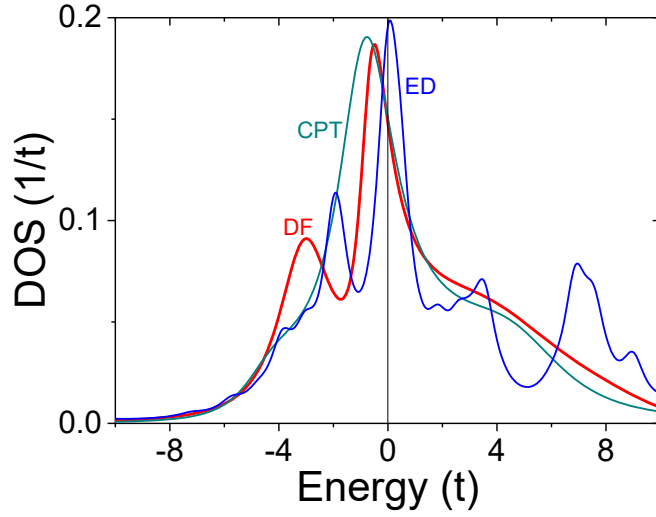


FIGURE 4.3: Density of states for dual fermion plaquette second order scheme (DF) in comparison with the cluster perturbation theory (CPT) and exact diagonalization (ED) of 2×2 plaquette for $U = 5.56$, $t'_0 = t' = 0.15$, $\mu_0 = 0.48$ and $\mu = 1.55$, $\beta = 3$.

In the present case, we use the critical plaquette as the reference model. This plaquette has a sixfold degenerate ground state and anomalies related to transitions between these ground states manifest themselves in the two-particle correlation functions at finite temperature through the T^{-3} behavior compared to the usual T^{-1} one in the general case.

The Bethe-Salpeter equation has an intertwined spin, site and frequency structure which can be simplified by looking at the different channels. Since our main interest is superconductivity, we consider the singlet particle-particle channel. For comparison we consider also particle-hole density and magnetic channels. Regarding the frequencies, we restrict ourselves to the lowest 10 Matsubara frequencies, since the vertex function Eq.(2.12) decays strongly with (ν, ν') [4].

Within the cluster dual fermion theory, the lattice instability manifests itself by $\lambda_{max} = 1$, where λ_i are eigenvalues of the following Bethe-Salpeter matrix $\Lambda_{i,j}$ in the case of the particle-particle singlet channel:

$$\Lambda_{12,34}^{P\nu\nu'}(q, \omega) = \frac{T}{2N_k} \sum_{k; 3'4'} \gamma_{12,3'4'}^{P\nu\nu'}(\omega) \tilde{G}_{4',4}(\omega - \nu', q - k) \tilde{G}_{3',3}(\nu', k) \quad (4.3)$$

with $i = (12, \nu)$, $j = (34, \nu')$ and $q = 0$, $\omega = 0$. In this case the matrix γ^P is Hermitian (real for $\omega = 0$), while matrix Λ is not Hermitian, but the leading eigenvalues are still found to be real for all channels. It has been shown that lattice and dual two-particle

quantities have the same set of poles[19]. In the limit $T \rightarrow 0$, the plaquette vertex has several divergences ($\sim T^{-3}$), corresponding to degeneracies of the reference model, while the cluster Green's function has divergences ($\sim T^{-1}$) at the degenerate point. Results for the maximum eigenvalues of the Bethe-Salpeter matrix Λ at the critical point for $\omega = 0$ and $q = 0$ obtained with the Fortran solver are presented in the Fig. 4.4.

The eigenvector corresponding to λ_{max} for the particle-particle singlet case has $d_{x^2-y^2}$ symmetry in the plaquette space. Exactly at the plaquette degenerate point the instability in the density channel is very large because the $N = 2, 3, 4$ states are degenerate. We found that this density instability is not robust against change of μ_0 and as soon as we shift it towards low hole doping $\mu_0 = 0.8$ there is no density instability[4]. On the other hand the singlet superconducting instability is very robust and becomes the leading one for doping lower than $\delta = 0.25$. The magnetic instability does not play any role for the doped case and becomes the leading one only in the half-filled case[4].

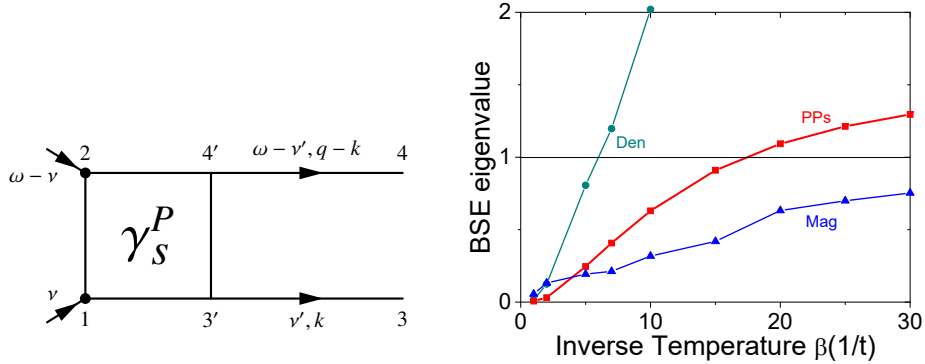


FIGURE 4.4: Diagrammatic representation of the Bethe-Salpeter kernel in the particle-particle channel (left) and its maximum eigenvalues (right) for the particle-particle singlet (PPs), density (Den) and magnetic (Mag) channel (right) for doped plaquette with $U=5.56$ and $t'=-0.15t$, $\mu=1.55$ and

Results for the maximum eigenvalues of the Bethe-Salpeter matrix Λ_{ij} for different hole doping are presented in the Fig. 4.5. At the half-field case with $t' = 0$ and $\mu_0 = U/2$ the main instability related with particle-hole magnetic channel with eigenvector corresponds to antiferromagnetic checkerboard structure. In this case there is not density and superconducting instability. For optimally doped case ($\mu_0 = 0.8$) the largest instability related with particle-particle singlet $d_{x^2-y^2}$ superconductivity. The density instability is not robust again small change in (μ_0) for plaquette. Finally

for overdoped case ($\mu_0 = 0.0$) there is no instability till $\beta = 10$ which may indicate formation of normal metallic phase.

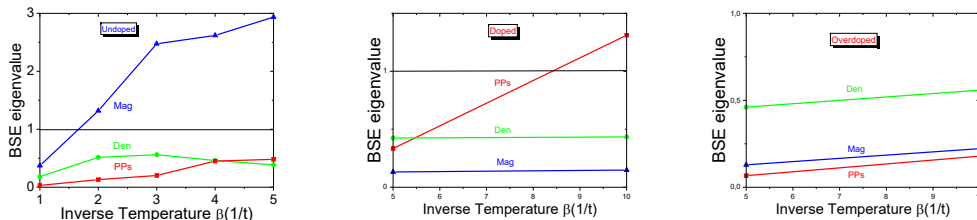


FIGURE 4.5: Maximum eigenvalues of BSE for half-filled plaquette with $U=8$ and $t'=0$ (left), for doped plaquette with $U=5.56$ and $t'=-0.3t$, $\mu_0=0.8$ $\mu=1.55$ (middle), and for overdoped plaquette with $U=5.56$ and $t'=-0.3t$, $\mu_0=0.0$ $\mu=1.5$ (right)

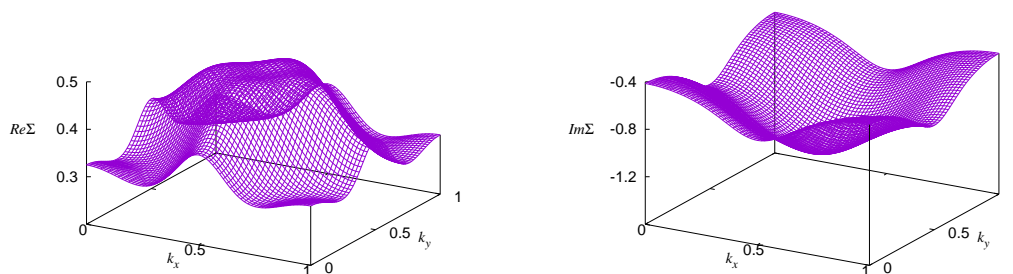


FIGURE 4.6: Real (left) and imaginary (right) part of lattice $\Sigma_{\mathbf{k},\nu=\pi T}$ for dual fermion plaquette theory for $U=5.56$, $t'/t=-0.15$, $\mu_0 = 0.48$, $\mu=1.55$ and $\beta = 3$.

The Fig.4.6 shows the periodized lattice DF- plaquette self-energy according to Eq. (2.17) in the full Brillouin zone 64×64 \mathbf{k} -mesh for the lowest Matsubara frequency. The real part of the self-energy already has an anomalously sharp feature near X point in the Brillouin zone.

4.2 Results of the Multiorbital DF solver

Results of the other Dual Fermion solver used in our study [31] are given on Fig. 4.4 (right), Fig. 4.5 and Fig. 4.6 for comparison.

The following results were obtained with the ‘‘Multiorbital DF’’ implementation of Dual Fermion method (Section 2.5).

For the system that was studied (Fig. 4.2), the self-consistency by the boldening of dual Green's function \tilde{G} (Eq. 2.31):

- does not seem necessary when calculating only the first-order perturbation, as the first iteration already leaves the result unchanged (Fig. 4.8);
- reaches a good convergence in ca. 10 iterations when calculating the first- and second-order perturbations (Fig. 4.11, 4.12, 4.7).

The maximum eigenvalues of Bethe-Salpeter matrices Λ Fig. 4.7 are in a good agreement with $\beta = 5$ and $\beta = 10$ on Fig. 4.4, while the shape of $\Sigma(\mathbf{k}, \omega_0)$ Fig. 4.10-4.12, middle, resembles Fig. 4.6 only roughly which may due to different choice of β .

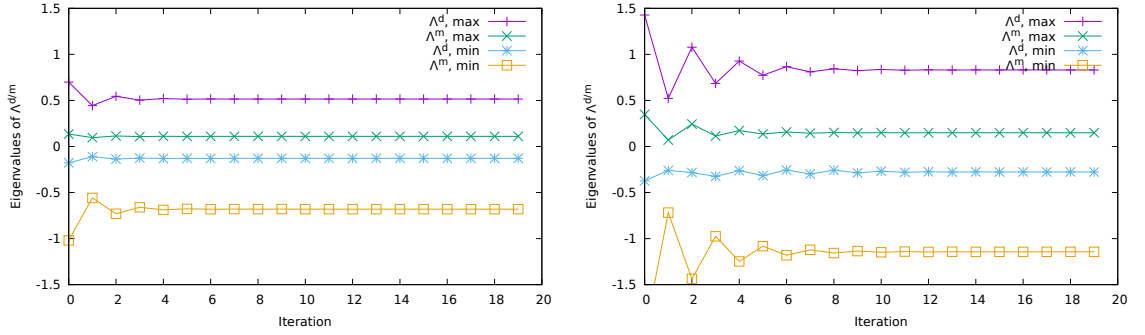


FIGURE 4.7: Convergence of the eigenvalues of Bethe-Salpeter matrix $\Lambda^{d/m}$ with iterations of dual Green's function boldening with $\mu = 1.55$, $t' = 0.15$. Left: $\beta = 5$, right: $\beta = 10$.

Reference system parameters: $t'_0 = 0.15$, $U = 5.56$, $\mu_0 = 0.479$, $\beta = 5$.

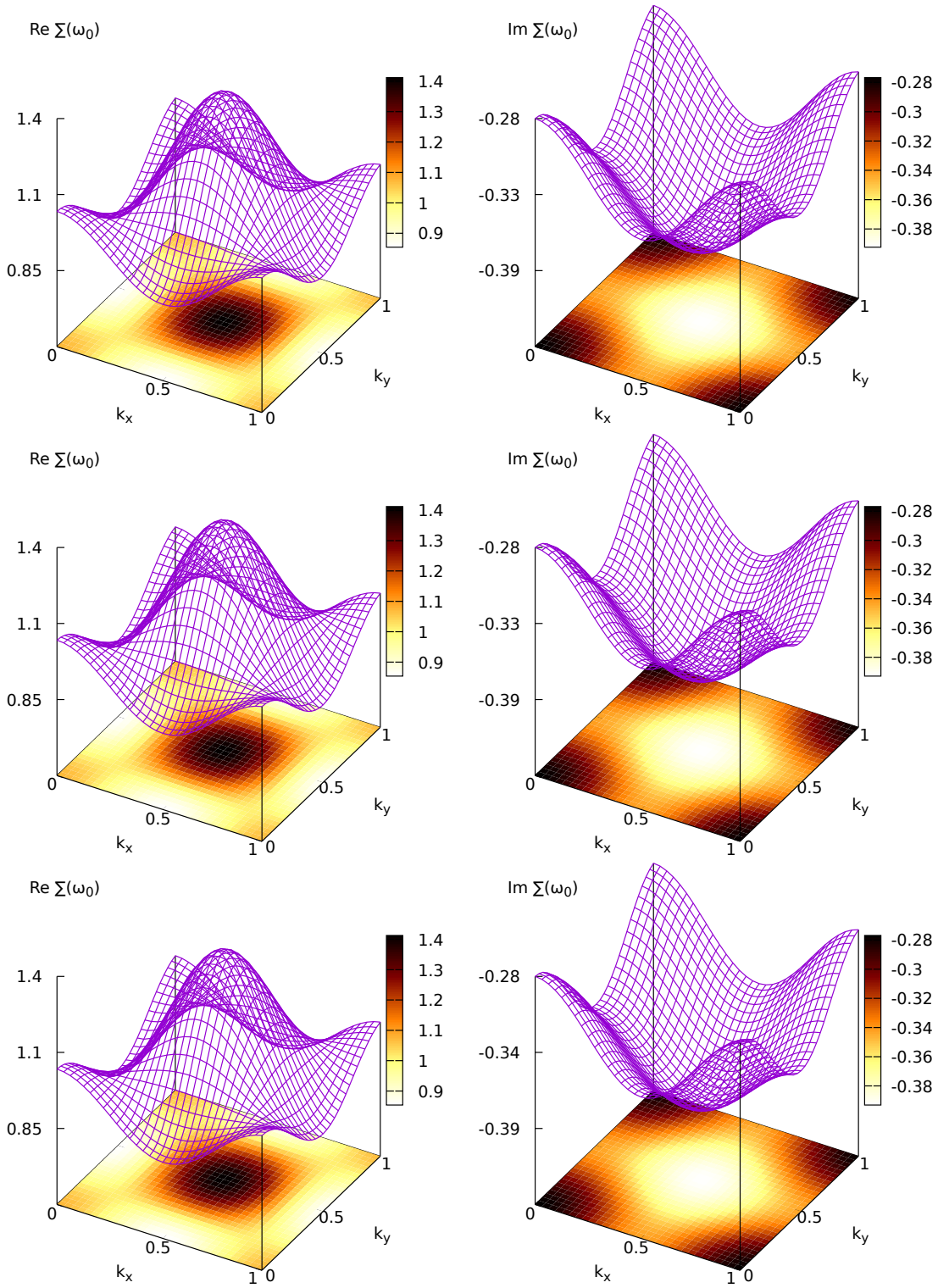


FIGURE 4.8: Lattice self-energy $\Sigma(\mathbf{k}, \omega_0)$ in the full Brillouin zone 32×32 \mathbf{k} -mesh on the lowest Matsubara frequency ω_0 for dual fermion plaquette theory. Top to bottom: $t' = 0$, $t' = 0.15$, $t' = 0.3$.

$\mu = 0.479$, with only first-order perturbation. Same results with and without self-consistency.

Reference system parameters: $t'_0 = 0.15$, $U = 5.56$, $\mu_0 = 0.479$, $\beta = 5$.

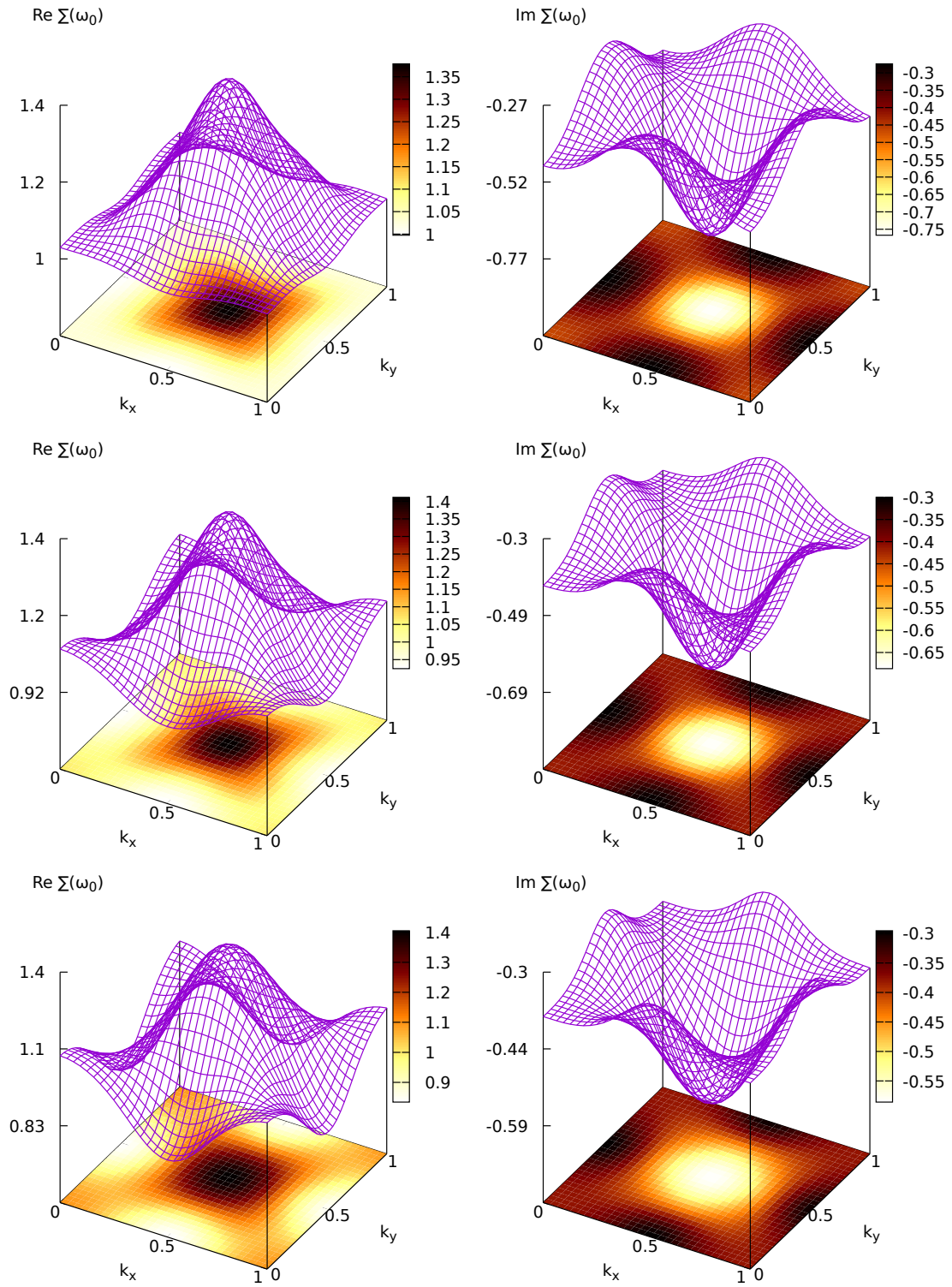


FIGURE 4.9: 4.8, continued: $\mu = 0.479$, with first- and second-order perturbation, 20 self-consistency iterations in the second order.

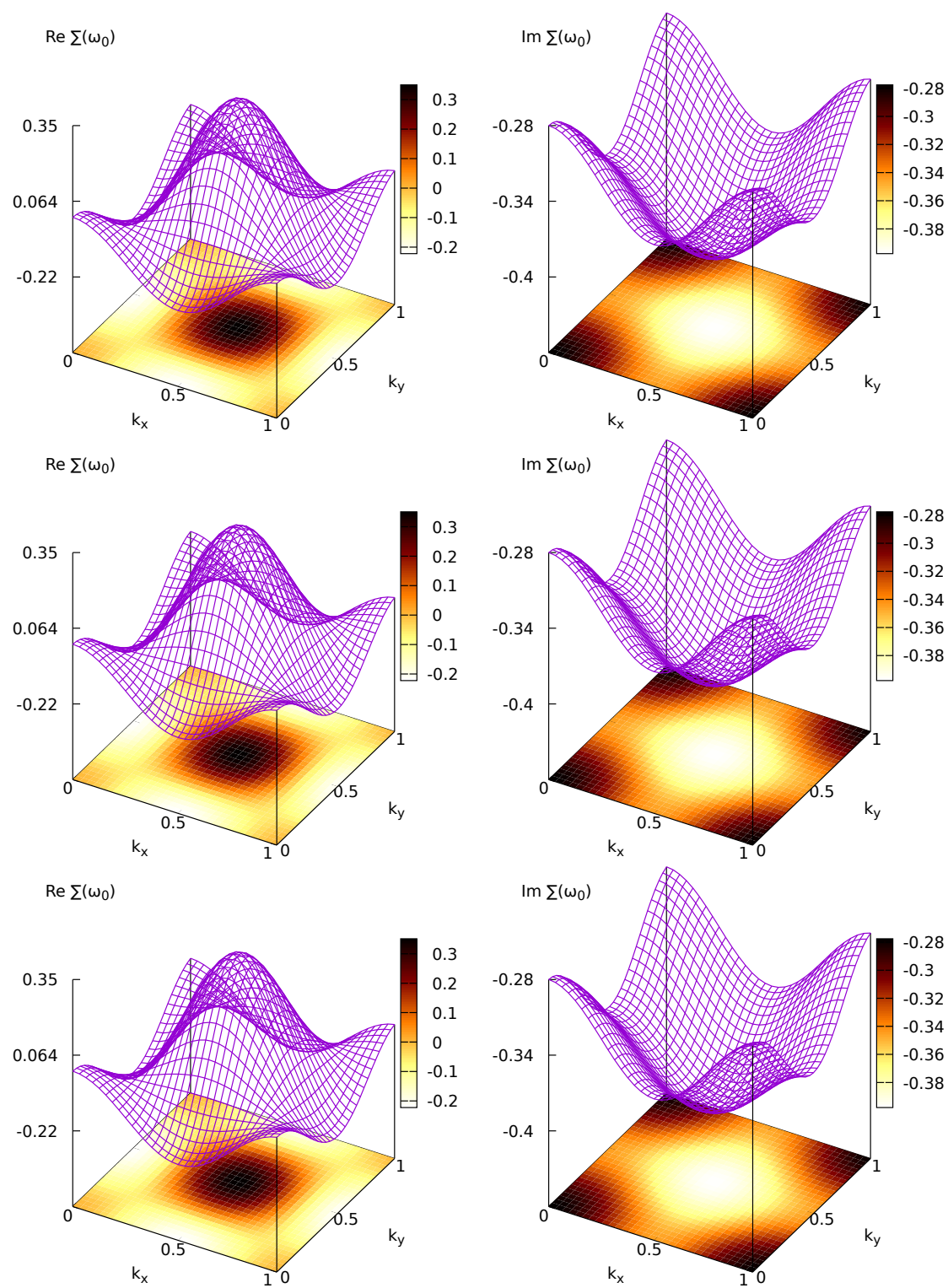


FIGURE 4.10: 4.8, continued: $\mu = 1.55$, with only first-order perturbation. Same results with and without self-consistency.

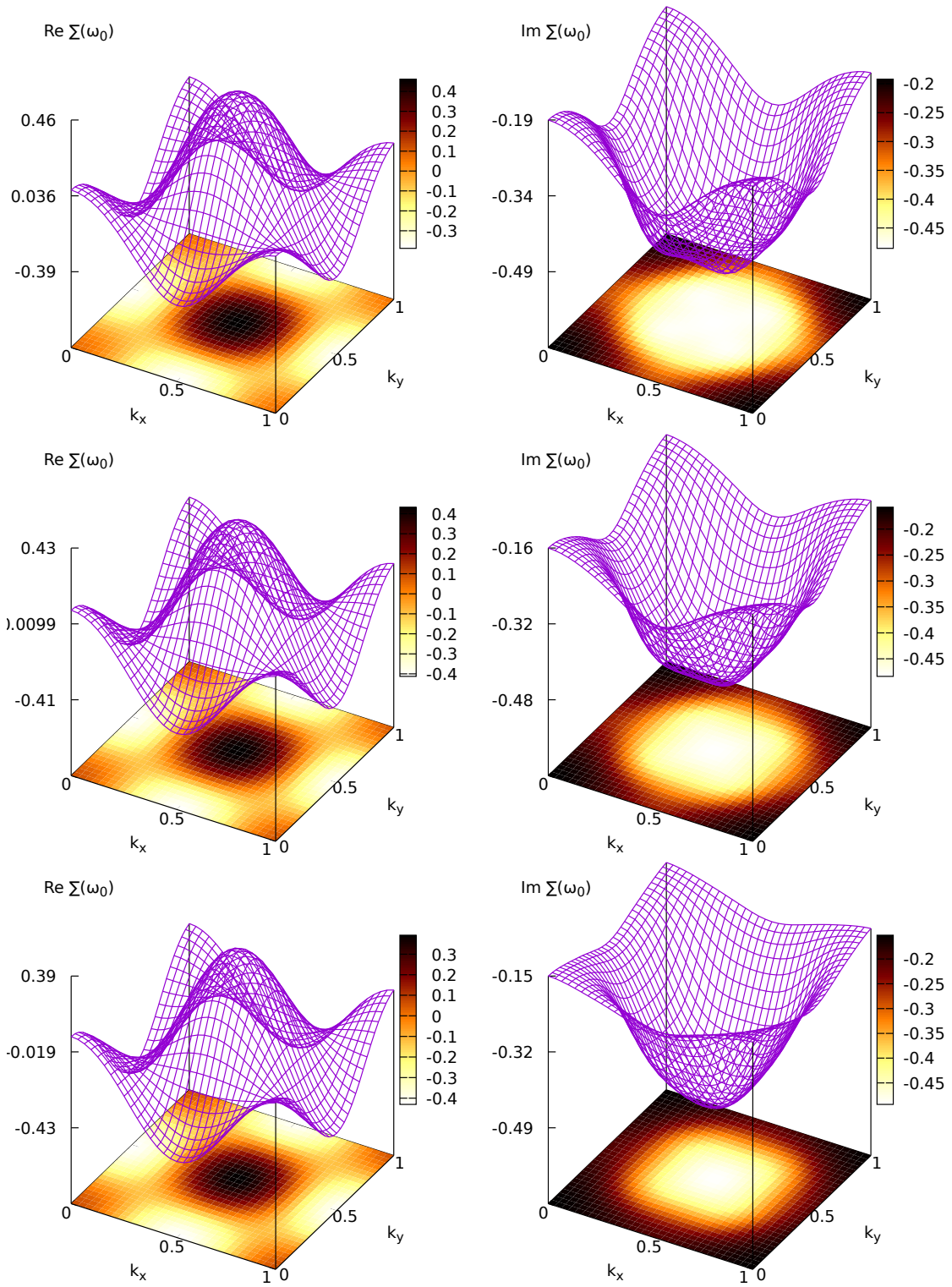


FIGURE 4.11: 4.8, continued: $\mu = 1.55$, with first- and second-order perturbation, 20 self-consistency iterations in the second order.

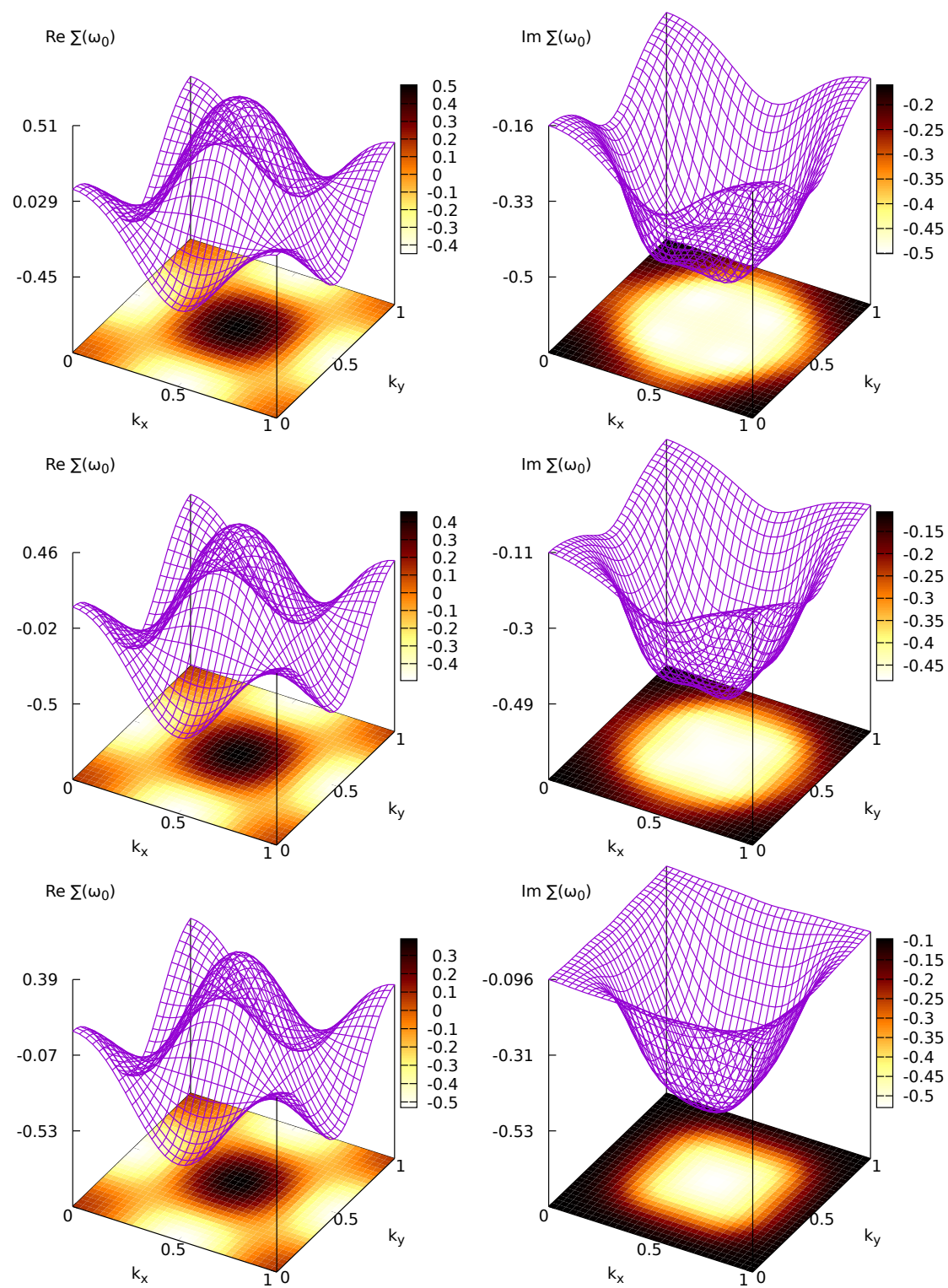


FIGURE 4.12: 4.8, continued: $\mu = 1.55$, with first- and second-order perturbation, no self-consistency.

Chapter 5

Exact Diagonalization of 4×4 Hubbard cluster

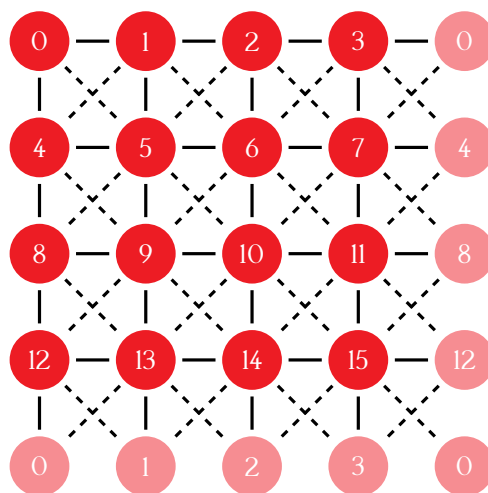


FIGURE 5.1: 4×4 cluster with periodic boundary condition. The circles represent sites with Coulomb interaction U , solid lines hopping t , dashed lines hopping t' .

A larger system can be constructed using the same principles as the 2×2 plaquette by arranging four 2×2 plaquettes as corners of a square and connecting them by the same nearest and next-nearest neighbour hoppings t , t' , making a Hubbard cluster of 4×4 sites, or the 4×4 *plaquette* (Fig. 5.1). The reason for choosing such system is that it allows to study the interaction of the highest number of 2×2 plaquettes possible on commonly available computing hardware, while also being less susceptible to the finite-size effects than the 2×2 plaquette.

It should be noted that the optional periodic boundary condition, unlike in the 2×2 plaquette, changes symmetry of the system and does not occur “automatically”

by a simple corresponding change of t_{eff} and t'_{eff} and instead has to be explicitly specified.

With periodic boundary, the system of nearest-neighbour hoppings t is equivalent to a hypercube [29], for example the stripe of 2×2 plaquettes between sites 0 to 7 can correspond to the one 3-dimensional cube of the hypercube, 8 to 15 to the other cube, and the remaining edges between the two stripes to the edges between the two 3d cubes. The system of the next-nearest neighbour hoppings t' can be said to be equivalent to two disconnected 3d cubes: one corresponding to the sites 1, 3, 4, 6, 9, 11, 12, 14, and the other one to the sites 0, 2, 5, 7, 8, 10, 13, 15.

A similar cluster, sans t' , has already been the subject of several studies, including Exact Diagonalization [28, 27]. More recent studies argue that the next-nearest neighbor hopping t' plays a crucial role in the stabilization of superconductivity [35], which is supported by our results (Section 5.2).

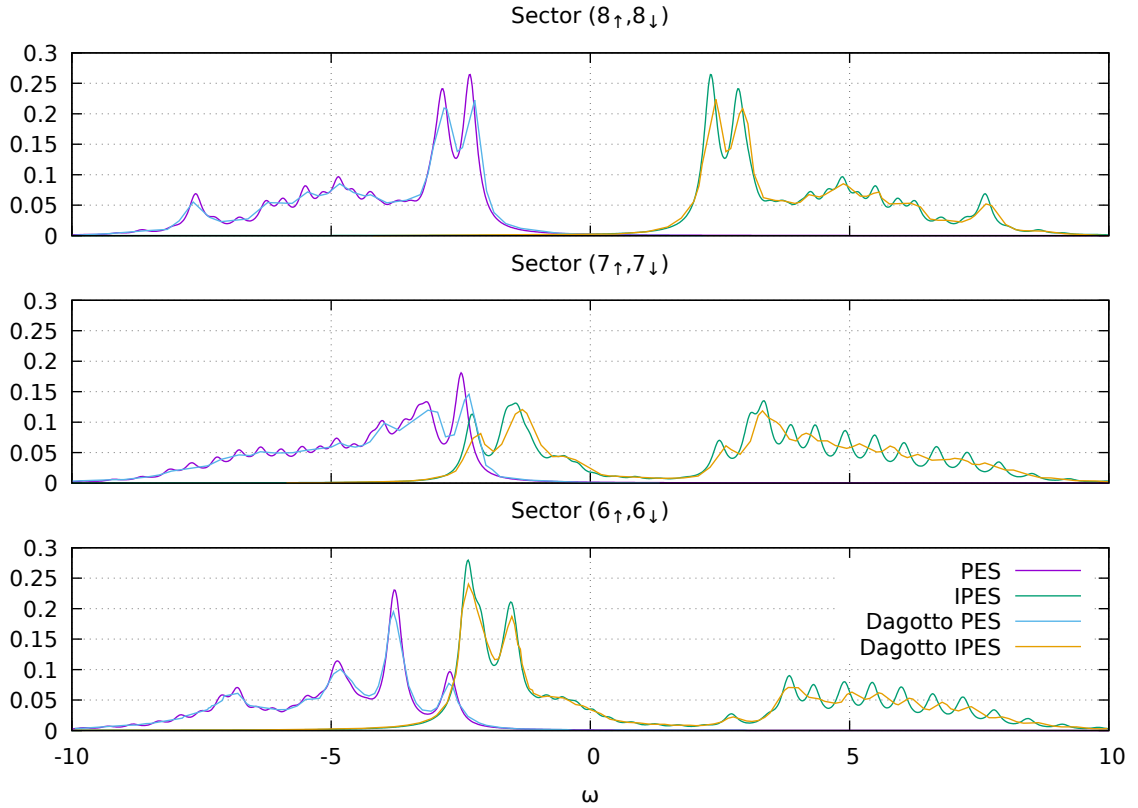


FIGURE 5.2: Comparison of spectral density of periodic 4×4 cluster $t'=0$, $\beta = 20$, $U=8$, $\mu = 4$ with calculations by Dagotto et al.[28, 27].

To ensure that the Exact Diagonalization of the 4×4 cluster is functioning correctly, as the first step the spectral densities by Dagotto et al.[28, 27] were reproduced

(Fig. 5.2).

5.1 Phase diagrams

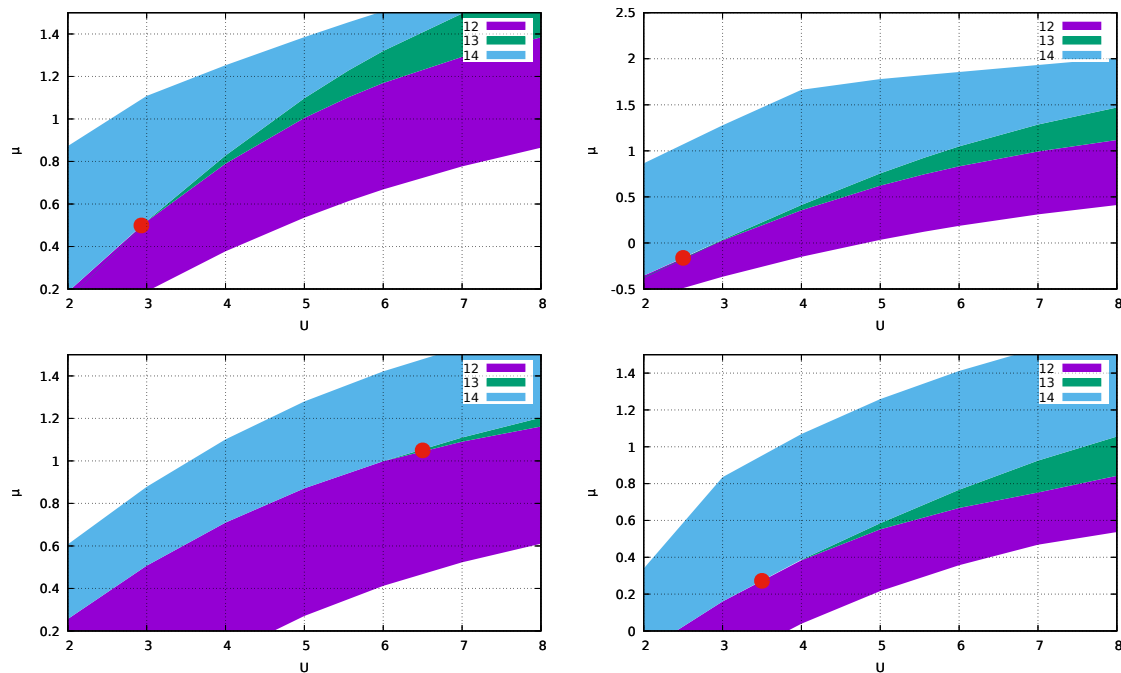


FIGURE 5.3: Number of electrons in the ground state of the 4×4 cluster.

Top left: periodic boundary, $t' = 0.15$, triple point at $U = 2.933$, $\mu = 0.499$;

Top right: periodic boundary, $t' = 0.3$, triple point at $U = 2.5$, $\mu = -0.162$;

Bottom left: nonperiodic boundary, $t' = 0.15$, triple point at $U = 6.5$, $\mu = 1.050$;

Bottom right: nonperiodic boundary, $t' = 0.3$, triple point at $U = 3.5$, $\mu = 0.272$.

Phase diagrams of total number of electrons have been calculated following the procedure described for the phase diagrams of the 2×2 plaquette in Section 3.1. It can be seen that for the same t' as the optimal $t' = 0.15$ of the 2×2 plaquette the 4×4 cluster exhibits a triple point as well (Fig. 5.3). However, the U and μ of the degenerate point are different from the 2×2 plaquette, and the number of electrons at the triple point does not correspond to the number of electrons in the 2×2 plaquette on Fig. 5.3 multiplied by 4 (8, 12, 16). In addition to that, the ground state of the 4×4 cluster may consist of such states of the four 2×2 plaquettes which are not necessarily their ground states. This means the triple point in the 4×4 cluster does not necessarily indicate the presence of a quantum critical point.

5.2 Pairing mechanism in real space. Comparison with Dual Fermion

To understand why superconductivity occurs, it is necessary to find a pairing mechanism, i.e., an attractive interaction between pairs of fermions. So far, we have studied the eigenvalues of the Bethe-Salpeter equation to identify such a superconducting instability. Here, we will gain additional insight from a complementary real-space method. We calculated the pairing energy of two holes on the 4×4 periodic cluster – which consists of 2×2 plaquettes – through the ground state energies in the different occupation sectors,

$$\Delta_{2h} = \tilde{E}_{2h} - 2\tilde{E}_{1h}, \quad (5.1)$$

where the energies are measured relative to the half-filled ground states E_0 with no holes, $\tilde{E}_{Nh} = E_{Nh} - E_0$. $\Delta_{2h} < 0$ signals pairing. Calculated energies for $t' = 0$ are in perfect agreement with the standard ED results[26].

Figure 5.4 shows the pair binding energy Δ_{2h} between pairs of holes for a 4×4 $t - t' - U$ Hubbard model with periodic boundary conditions as a function of interactions strength U for different next-nearest neighbours hopping t' . There is a very strong binding of two holes around $U = 6$ and $t'/t = -0.3$, which is consistent with the estimate for the cuprates [101]. The pairing energy is of the order of $\Delta_{2h}/t \approx -0.7$ which is of the order 3000 K for $t \approx 0.4$ eV for generic cuprates model [101, 6]. There is a clear change of behaviour of Δ_{2h} as a function of t' , with the vanishing of the pairing energy at small U . It can be attributed to the change of the ground state for the sector $(7\uparrow, 7\downarrow)$ at $t'/t \approx 0.12$ [4]. We also observe a drastic change of the behavior of the magnetic correlations from antiferromagnetic at $t' = 0$ to almost non-magnetic for $t'/t = -0.3$ in this sector[4]. Similar energetics of hole-binding in 4×4 Hubbard cluster was found recently[129] for a different model of inhomogeneous hoppings[126]

These results clearly show the importance of t' , which greatly increases the pairing energy gain. At the same time, in a non-interacting systems $\Delta_{2h} = 0$ by definition, so a finite value of U is also necessary for the pairing. We find that the optimal U increases with t' . A second observation is the order of magnitude of the pairing, $\Delta_{2h} \approx t \gg k_B T_c$. This tells us that bound pairs exist for temperatures far above the superconducting region. The superconducting transition should then be seen as the condensation of these pairs. Thus, the binding energy of two holes turns out to be much higher than the superconducting critical temperature which means that the pairs (“bipolarons”) should be well-defined also in non-superconducting phase, a situation dramatically different from the conventional BCS superconductivity. The difference is like the difference between purely itinerant weak ferromagnets and ferromagnets with local magnetic moments which exist until very high temperatures

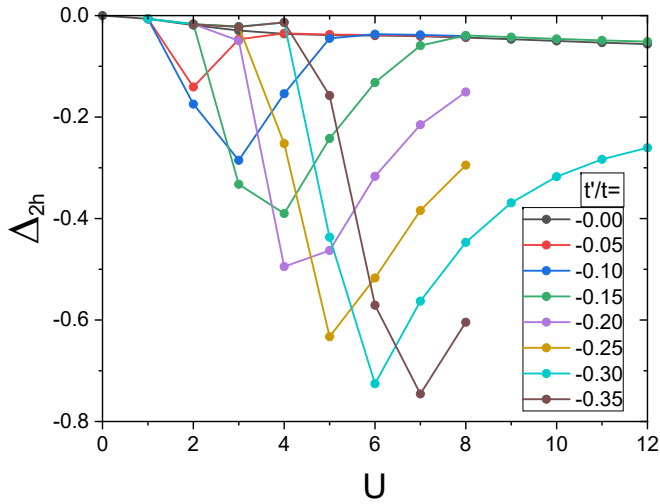


FIGURE 5.4: Pairing energy Δ_{2h} of two holes in a 4×4 cluster with periodic boundary condition as a function of U and t' .

and only order, rather than appear, at the Curie temperature [96].

We analyzed the spin-spin correlation function in the sector $(7\uparrow, 7\downarrow)$ with different NNN hoppings t' (Fig.5.12) and clearly see a sharp change from antiferromagnetic correlations for $t' = 0$ to almost nonmagnetic case or ferromagnetic stripes in the x or y directions for $t' = 0.3$. A similar reduction of AFM-correlations and existence of FM-one with t' was found in a lattice QMC study[135].

5.3 Spectral information

Due to the degeneracy of states with different particle number, the density of states of the plaquette is large close to the Fermi level. The availability of low-energy states is the driving force behind the instabilities that occur once a lattice of plaquettes is considered. In Fig. 5.5 we compare the density of states for the plaquette DF perturbation theory for low temperature ($\beta = 5$) with the ED results for the 4×4 cluster in the sector $(7\uparrow, 7\downarrow)$, which corresponds to a 2×2 lattice of plaquettes. These two methods are complementary: the DF approach is perturbative in the inter-plaquette coupling and able to handle large lattices, whereas the ED is exact but limited by the cluster size. From the comparison of the two curves, we conclude that both the dual fermion theory and the ED results show a pseudogap, i.e., a substantial reduction of the density of states compared to a single plaquette. It is natural to conclude that the pseudogap in the 4×4 cluster is related to the coherent

interactions of the large peak on the DOS in the reference plaquette or Fano-like effect of interactions with the “soft fermion mode” of the low-lying excitations which are encoded in the local vertex functions of the DF-approach. In this sense the pseudogap physics is not related to the magnetic fluctuations, and is more in line with the “hidden fermion” physics[110, 111] or “destructive interference phenomena”[93].

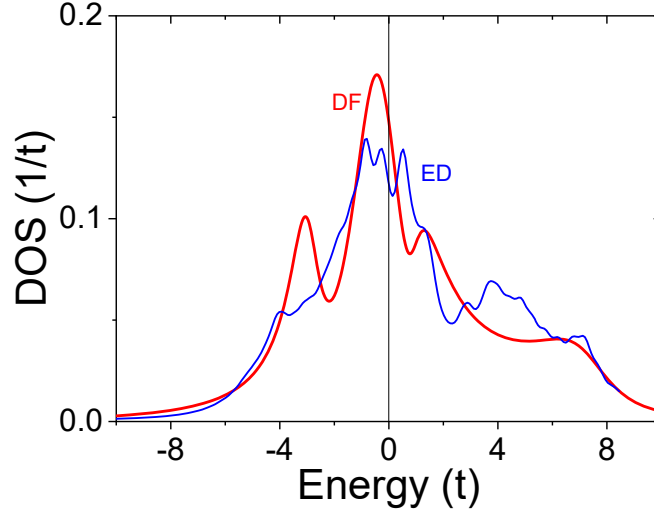


FIGURE 5.5: Density of states for dual fermion plaquette perturbation (DF) with $\beta = 5$ in comparison with exact diagonalisation (ED) for 4×4 periodic cluster. See also Fig. 4.3.

5.4 Ground state properties

We present low-lying many-body states of (4×4) periodic cluster for the sector $(7\uparrow, 7\downarrow)$ in Fig. 5.6 and marked the degeneracy of few important states the numbers. The ground state for $t' = 0$ is three-fold degenerate due to 2^4 super-cube symmetry[29]. As function of t this state split to ground state doublet and a singlet which has higher energy. Around $t'/t = -0.12$ the ground state of the sector $(7\uparrow, 7\downarrow)$ change to singlet (red curve on Figure 5.6) with much lower energy and different symmetry related with drastic change of spin-spin correlations from antiferromagnetic-like for small t' to nonmagnetic of weak ferromagnetic for larger t' (Fig. 5.12).

Fig. 5.7 (left panel) shows the many-body ground state energies for (4×4) periodic cluster for different sectors with N electrons for different interaction strength $U = 0 \div 12$ (from bottom to top). One clearly see that the largest effect of lowering

energy of $N = 14$ sector compare to half-field $N = 16$ one (red dot) appears exactly at $U = 6$ where the pair-hole binding energy has minimum for $t'/t = -0.3$ (Fig. 5.4). In the left panel of Fig. 5.7 we show comparison of our exact diagonalization of 4×4 periodic cluster for $t'/t = -0.15$ with ED results of Dagotto et.al[26] for $t' = 0$ and $U=4, 8, 10$. Note that our ED results for $t' = 0$ exactly coincide with Dagotto et.al[26]. We note that the many-body energies for half-field cluster $N = 16$ almost perfectly not depends on small change of t' due to antiferromagnetic blocking of t' hoppings. The same effect happens even for one hole with $N = 15$ probably due to large string-like $t - J$ blocking. However for the two-hole situation with $N = 14$ there are clearly appreciable lowering of ground state energy for $U = 4$ exactly in the same place where the pair-hole binding energy has minimum for $t'/t = -0.15$ (Fig. 5.4).

In Fig. 5.12 different static correlators are shown from ED calculations of (4×4) periodic cluster with $t' = 0$ and $t'/t = -0.3$. The spin-spin correlators in the sector $N = 14$ ($7\uparrow, 7\downarrow$) drastically change behaviour from almost antiferromagnetic at $t' = 0$ to nonmagnetic or ferrimagnetic-like structure.

Fig. 5.10 show density of states for different sectors (hole concentrations) for ED calculations of (4×4) periodic cluster with $t'/t = -0.15$ and $t'/t = -0.3$. We can conclude that for $t'/t = -0.3$ and optimal $U = 5.56$ all calculated sectors corresponding to doping $\delta = 0.0525 \div 0.25$ have large pseudogap DOS. Simple pictorial view on such pseudogap formation presented in Fig. 5.9 (left). If we consider (4×4) cluster build from four interacting (2×2) plaquettes each of has sharp peak at Fermi level, then it is clear that through the resonant interactions the total DOS would have a pseudogap at E_F . This is similar to the Fano effect for Kondo-like impurity in the conducting bath.

We should point out that the optimal interaction $U/t \approx 6$ is smaller than the bandwidth $W/t = 8$ and substantially below the strong coupling, effective $t - J$ model limit. Therefore, the huge hole-hole binding we found in the 4×4 cluster at intermediate $U/t \approx 6$, with two holes located on different “diagonal” plaquettes, is very different from the so-called “string-like” effective hole-hole interactions in the $t - J$ model, where two holes are sitting with nearest-neighbor or next-nearest-neighbor distance [26], i.e., in the same plaquette. On Fig. 5.8 we presented the pair-hole binding energy for ED calculations of (2×2) periodic plaquette with $t'/t = -0.3$ as function of U . The energy of the two-hole binding is much smaller than for (4×4) cluster with the same t' . The energy of two-hole binding on a single 2×2 plaquette is very similar to the results of Ref. [5] at $t' = 0$, see Fig. 5.8. This indicates that it is not favourable to put two holes in a single plaquette. Thus, the pairing is a phenomenon that emerges in the lattice of plaquettes, as we could also see in the dual Bethe-Salpeter equation.

Analysis of the hole-hole correlation function in this sector shows that the two

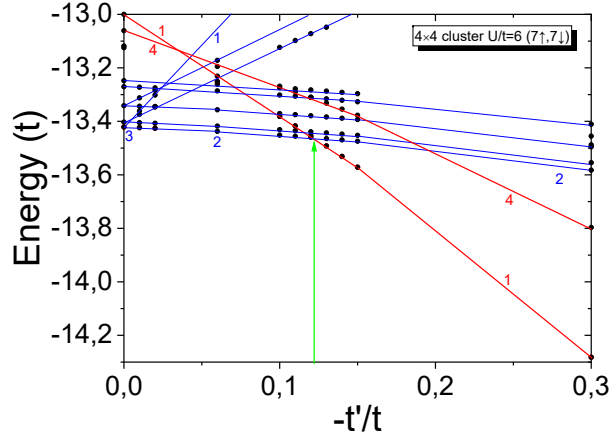


FIGURE 5.6: Many body states of (4×4) periodic cluster for the sector $(7\uparrow, 7\downarrow)$ as a function of t' for $U/t = 6$. The degeneracy of few low-lying states are marked with the numbers. The green arrow indicate the critical t' for ground state crossing.

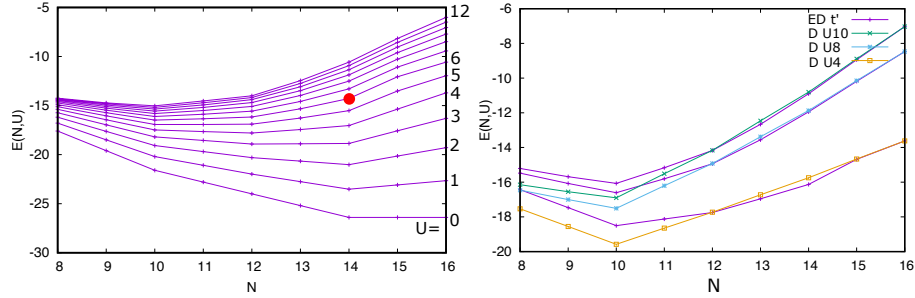


FIGURE 5.7: Many body ground state energies of (4×4) periodic cluster for different sectors as function of U for $t'/t = -0.3$ and $\mu = 0$. The red points shows the largest effect of lowering the total energy for the sector $N = 14$ ($7\uparrow, 7\downarrow$) (left). In other words, $E(14, U) - E(16, U)$ is minimal for $U = 6$. Comparison of the present ED calculations for $t'/t = -0.15$ with (ED t') ED results of Dagotto et.al[26] for $U=4, 8, 10$ from bottom to top (right).

holes occupy two different “diagonal” plaquettes in 4×4 cluster Fig. 5.9 (right). In other words, the hole-hole displacement is $(2, 2)$. In the periodic 4×4 cluster, the two holes thus share next-nearest neighbors plaquettes. Energetically, this configuration of the holes makes the t' hopping along the diagonals very efficient (see also Fig. 5.9 (right)). Thus, it is the kinetic energy associated with t' which drives such a strong hole-condensation for this concentration $\delta = 0.125$ (2 holes on 16 sites), which is not far from the optimal hole concentration for cuprates.

Fig. 5.19, (middle) shows the \mathbf{k} -dependent self-energy from exact diagonalization

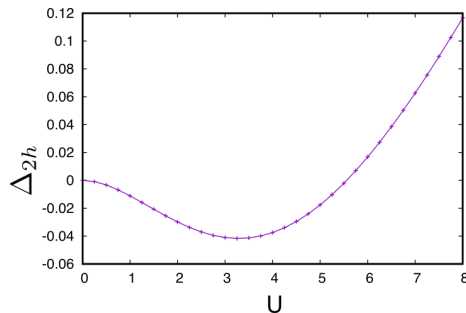


FIGURE 5.8: Energy of two-hole binding for 2×2 plaquette for $t'/t = -0.3$. Note that the energy scale is reduced by more than an order of magnitude compared to the 4×4 plaquette, see Fig. 5.4.

for of 4×4 cluster for $\delta = 0.125$ ($7\uparrow, 7\downarrow$) with first three non-local elements of $\Sigma_{ij}(\nu = \pi T)$. Due to periodic boundary condition the more long-range elements of $\Sigma_{ij}(\nu)$ are strongly overestimated. The general shape of the self-energy agree well with results of plaquette DF-perturbation (Fig. 4.6).

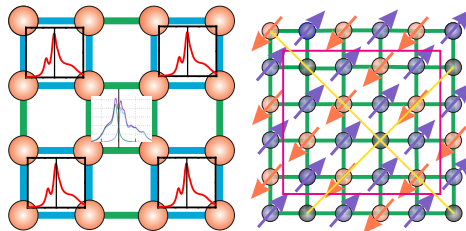


FIGURE 5.9: Schematic view of pseudogap formation in (4×4) periodic cluster from the peak DOS structure of individual 2×2 plaquettes (left), and the sketch of effective t' hopping in presence of two holes in AFM structures (right)

5.5 Hole-hole correlation

To investigate the important issue of the hole-hole interaction in the lattice, we use two approaches to the notion of a hole in the 4×4 plaquette. The first one is to consider a hole as an absence of electrons, *i.e.*, an empty site is viewed as a hole. The hole density operator at site i is then given by

$$n_i^h = (1 - n_{i\uparrow})(1 - n_{i\downarrow}). \quad (5.2)$$

We then investigate the hole-hole correlation function $\langle n_i^h n_j^h \rangle - \langle n_i^h \rangle \langle n_j^h \rangle$ in the ground state of the $(7\uparrow, 7\downarrow)$ sector as a function of the displacement $i - j$. The average hole density $\langle n_i^h \rangle$ is obviously given by $\langle n_i^h \rangle = 1 - \langle n \rangle + d$, where $\langle n \rangle$ is the average electron density, which in the given sector is just $7/8 = 0.875$, and $d = \langle n_{i\uparrow} n_{i\downarrow} \rangle$ is the double occupancy. The results for two different values of t' are shown in Fig 5.12.

The second approach is in the spirit of Landau's Fermi liquid theory. The hole is then viewed as the result of an annihilation operator acting on the half-filled $((8\uparrow, 8\downarrow)$ sector) ground state $|\psi_{16;0}\rangle$. Correspondingly a state with two holes would be the result of two annihilation operators acting on that state: $|\psi_{14;ij}\rangle = A_{ij} c_{i\uparrow} c_{j\downarrow} |\psi_{16;0}\rangle$, with A_{ij} being the normalization factor chosen in such a way that the norm of this state is unity. Then we calculate the overlap C_{ij} between the ground state of the $(7\uparrow, 7\downarrow)$ sector $|\psi_{14;0}\rangle$ and $|\psi_{14;ij}\rangle$ to see how well the two-hole state describes the true ground state. The results are shown in Fig. 5.12. Here we have to understand that for $t' = 0$ the ground state of the 4×4 plaquette is 3 fold degenerate. This is an accidental degeneracy that occurs because the 4×4 periodic lattice without t' is equivalent to a $2 \times 2 \times 2 \times 2$ hypercubic lattice[29]. This accidental degeneracy is unphysical in the sense that it is absent in larger two-dimensional clusters. Other effects of this property one can see on the left panel of fig. 5.12 noting that observables when i and j are nearest neighbors along the diagonal are identical with those when i and j are next nearest neighbors along the horizontal or vertical direction. On a 4-dimensional hypercube those pairs of sites are equivalent.

Due to this degeneracy and to the fact that C_{ij} is not an observable we have to take the results for $t' = 0$ with a grain of salt. The results are obviously dependent on the linear combination of the three ground states we choose to calculate the overlap (fig. 5.12 shows one such combination produced randomly by the ED solver). Still, we can see that C_{ij} tends to be largest if i and j have different spins on the Néel state. This is a clear indication that antiferromagnetic fluctuations are well preserved in the $(7\uparrow, 7\downarrow)$ sector with no NNN hopping. On the other hand for $t' = 0.3$ the largest overlap is found for the pairs (1,3) and (1,11), sites being numbered from 1 to 16 from left to right and then from top to bottom, in agreement with the understanding that large NNN hopping completely destroys the antiferromagnetic order.

Another interesting observation arises when we calculate the sum $\sum_{ij} C_{ij}^2$ for different values of t' . This value shows how well the $|\psi_{14;0}\rangle$ state is described in terms of the two holes states $|\psi_{14;ij}\rangle$. It turns out that while for $t' = 0$ this value is reasonably large (1.25, one should be surprised it is larger than one as the states $\Psi_{14;ij}$ are no orthogonal), for $t' = 0.3$ it is very low (0.0013). This indicates that the second approach to the notion of hole, in terms of the Fermi liquid theory is hardly appropriate for large t' , in other words the holes in that regime are very incoherent.

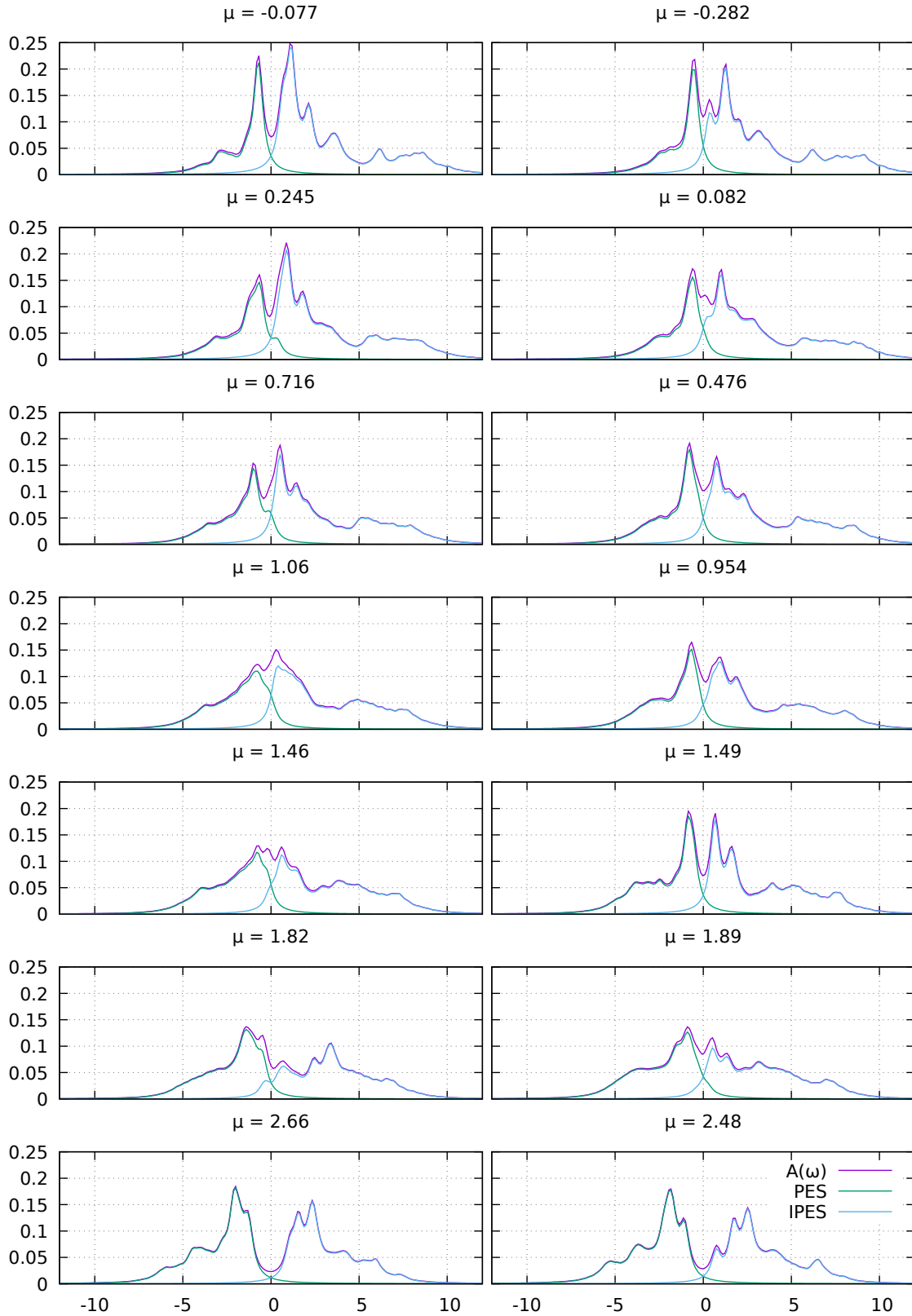


FIGURE 5.10: Spectral density $A(\omega)$ of periodic 4×4 cluster, $U = 5.56$, $\beta = 10$. Left to right: t' : 0.15, 0.3. Top to bottom: hole doping δ (sectors): 0.375 ($5_{\uparrow}, 5_{\downarrow}$); 0.3125 ($(6_{\uparrow}, 5_{\downarrow}), (5_{\uparrow}, 6_{\downarrow})$); 0.25 ($6_{\uparrow}, 6_{\downarrow}$); 0.1875 ($(7_{\uparrow}, 6_{\downarrow}), (6_{\uparrow}, 7_{\downarrow})$); 0.125 ($7_{\uparrow}, 7_{\downarrow}$); 0.0625 ($(8_{\uparrow}, 7_{\downarrow}), (7_{\uparrow}, 8_{\downarrow})$); 0 ($8_{\uparrow}, 8_{\downarrow}$).

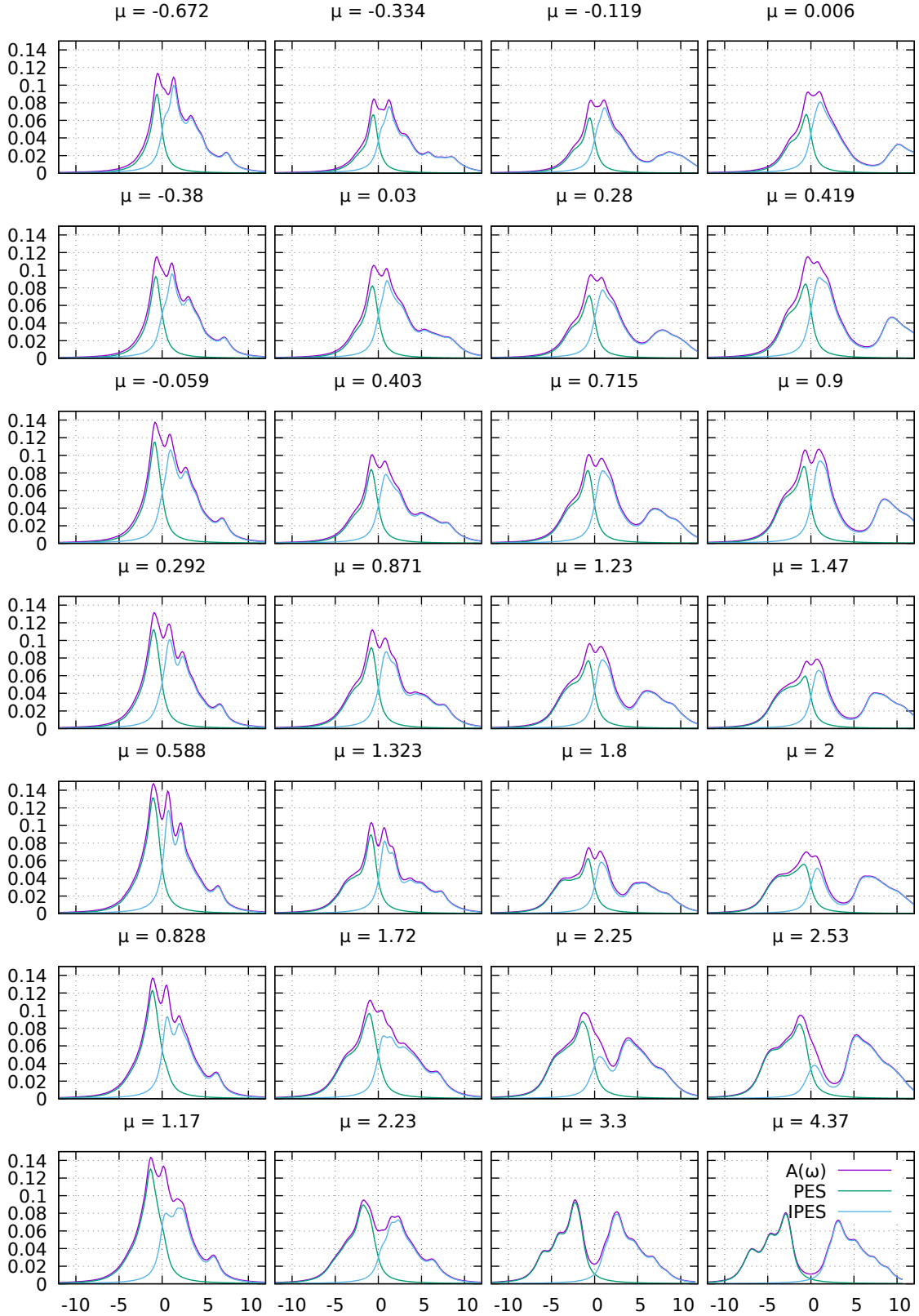


FIGURE 5.11: Spectral density $A(\omega)$ of periodic 4×4 cluster, $t' = 0.3$, $\beta = 5$. Left to right: U : 3, 5, 7, 9. Top to bottom: hole doping δ (sectors): 0.375 ($5_{\uparrow}, 5_{\downarrow}$); 0.3125 ($(6_{\uparrow}, 5_{\downarrow}), (5_{\uparrow}, 6_{\downarrow})$); 0.25 ($6_{\uparrow}, 6_{\downarrow}$); 0.1875 ($(7_{\uparrow}, 6_{\downarrow}), (6_{\uparrow}, 7_{\downarrow})$); 0.125 ($7_{\uparrow}, 7_{\downarrow}$); 0.0625 ($(8_{\uparrow}, 7_{\downarrow}), (7_{\uparrow}, 8_{\downarrow})$); 0 ($8_{\uparrow}, 8_{\downarrow}$).

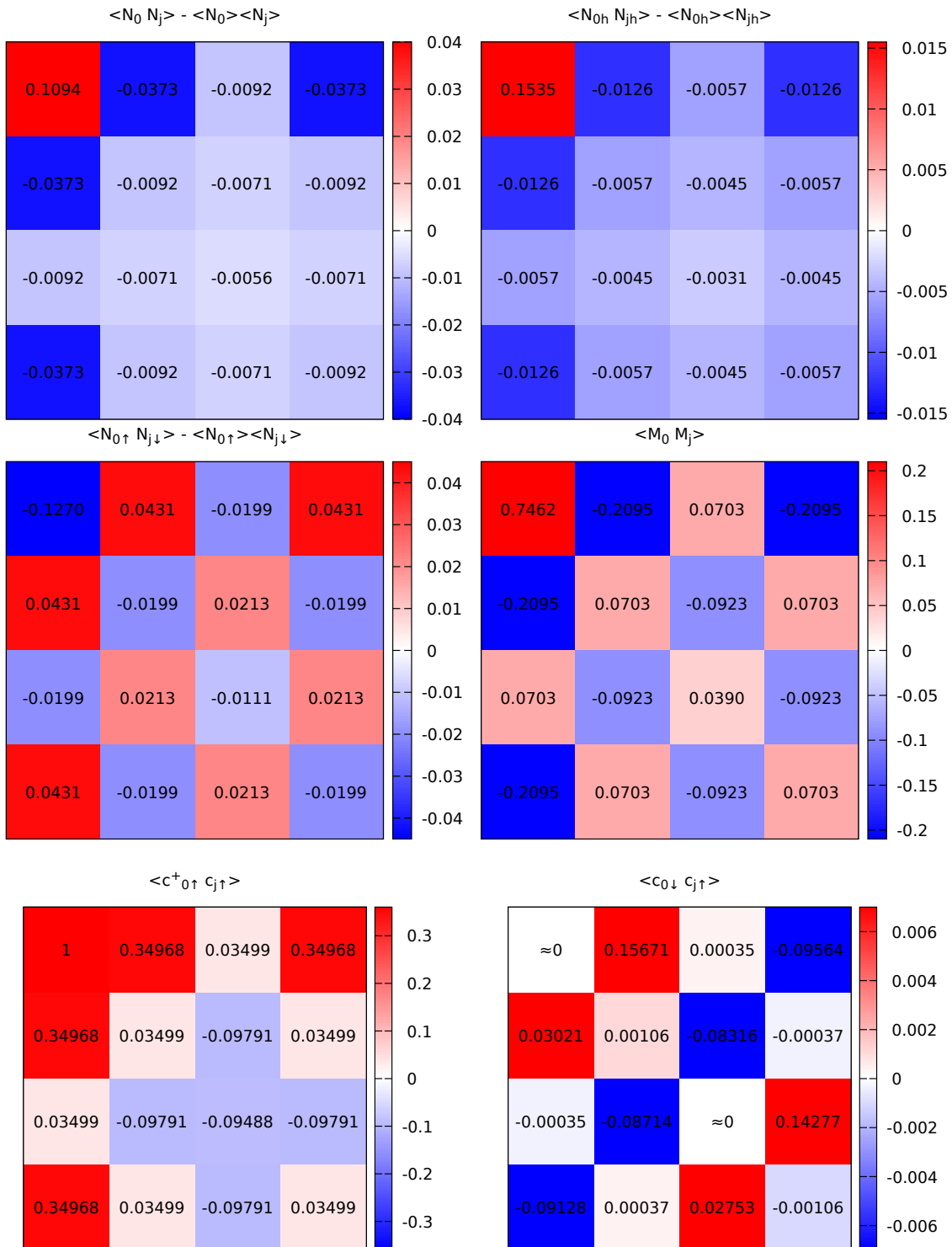
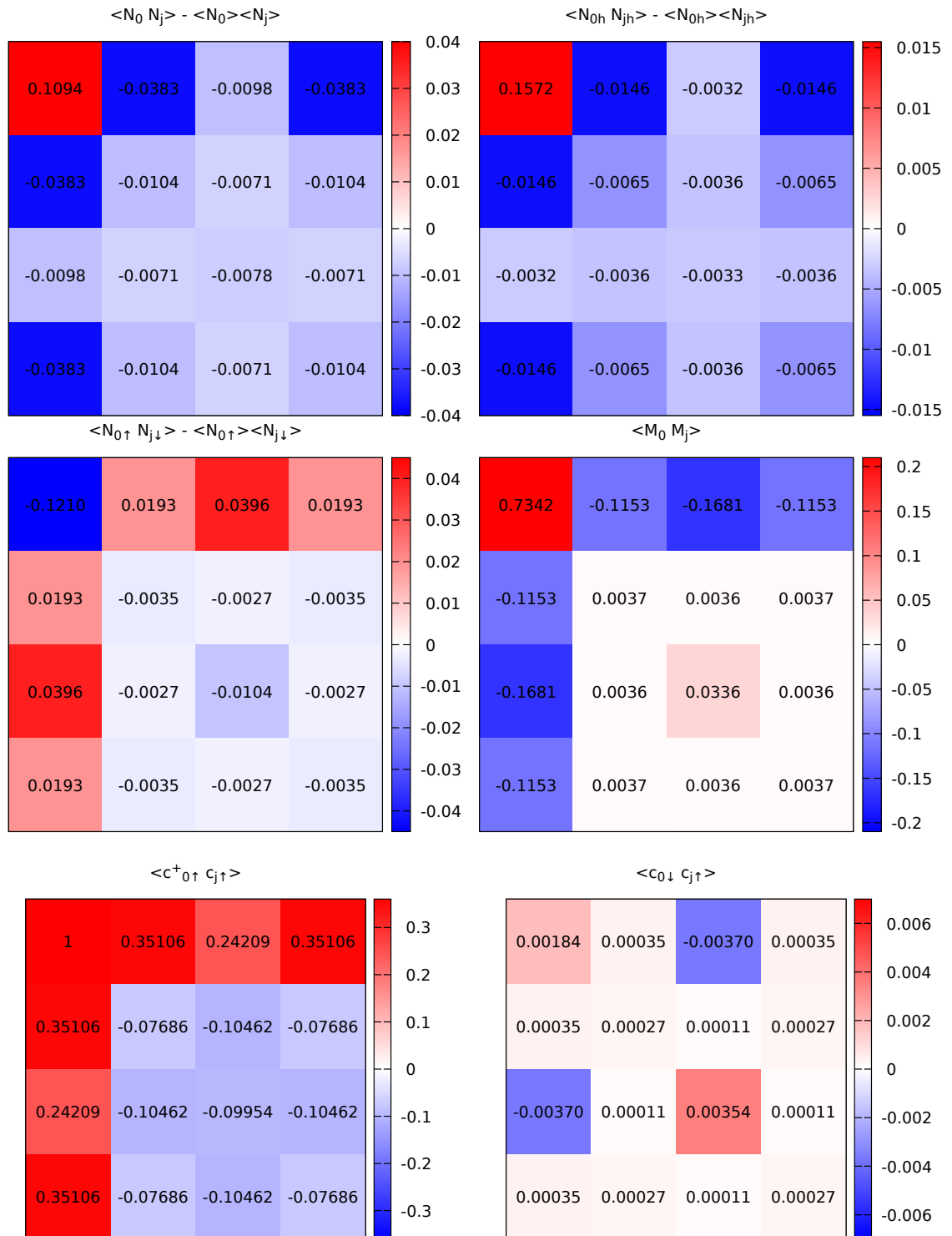
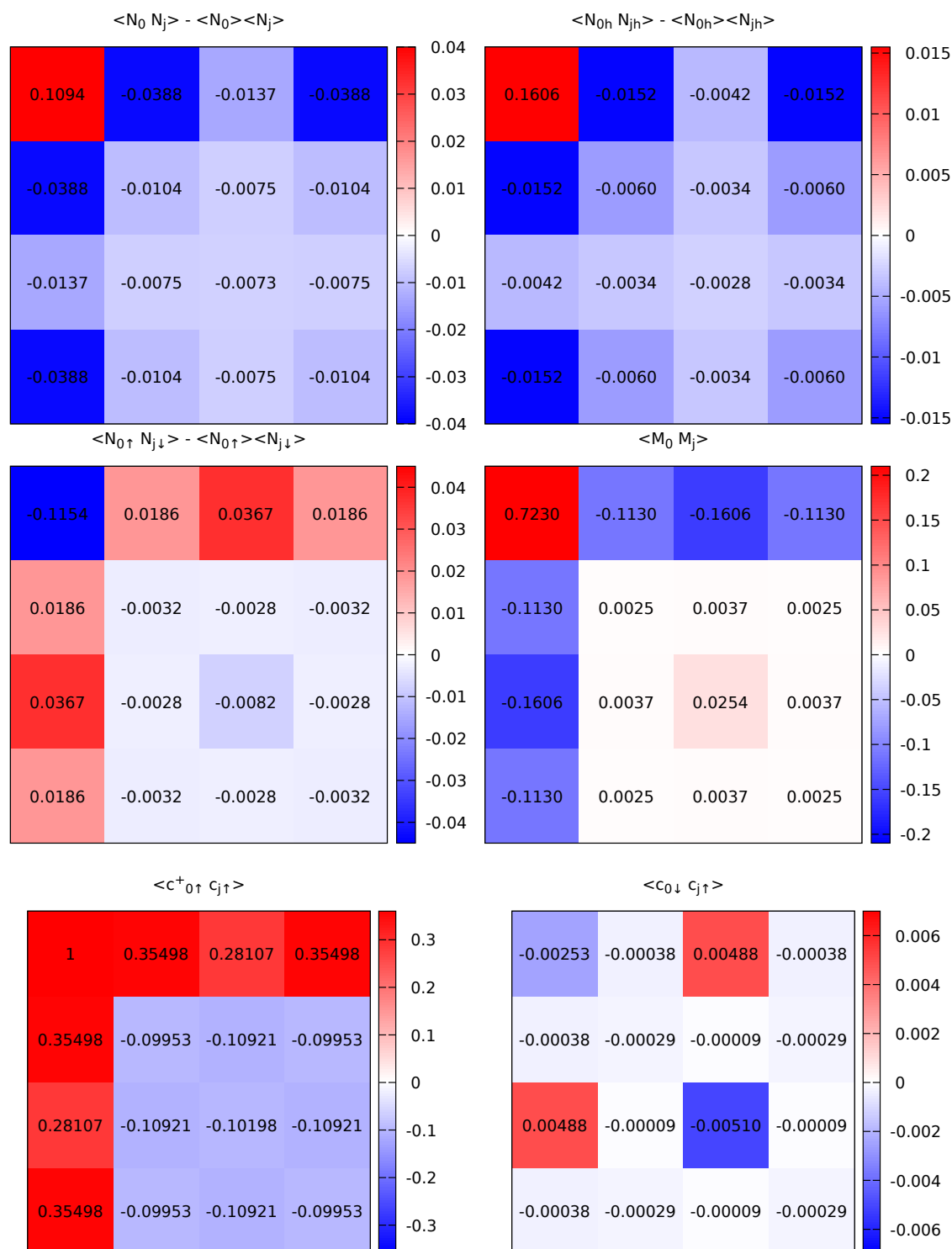
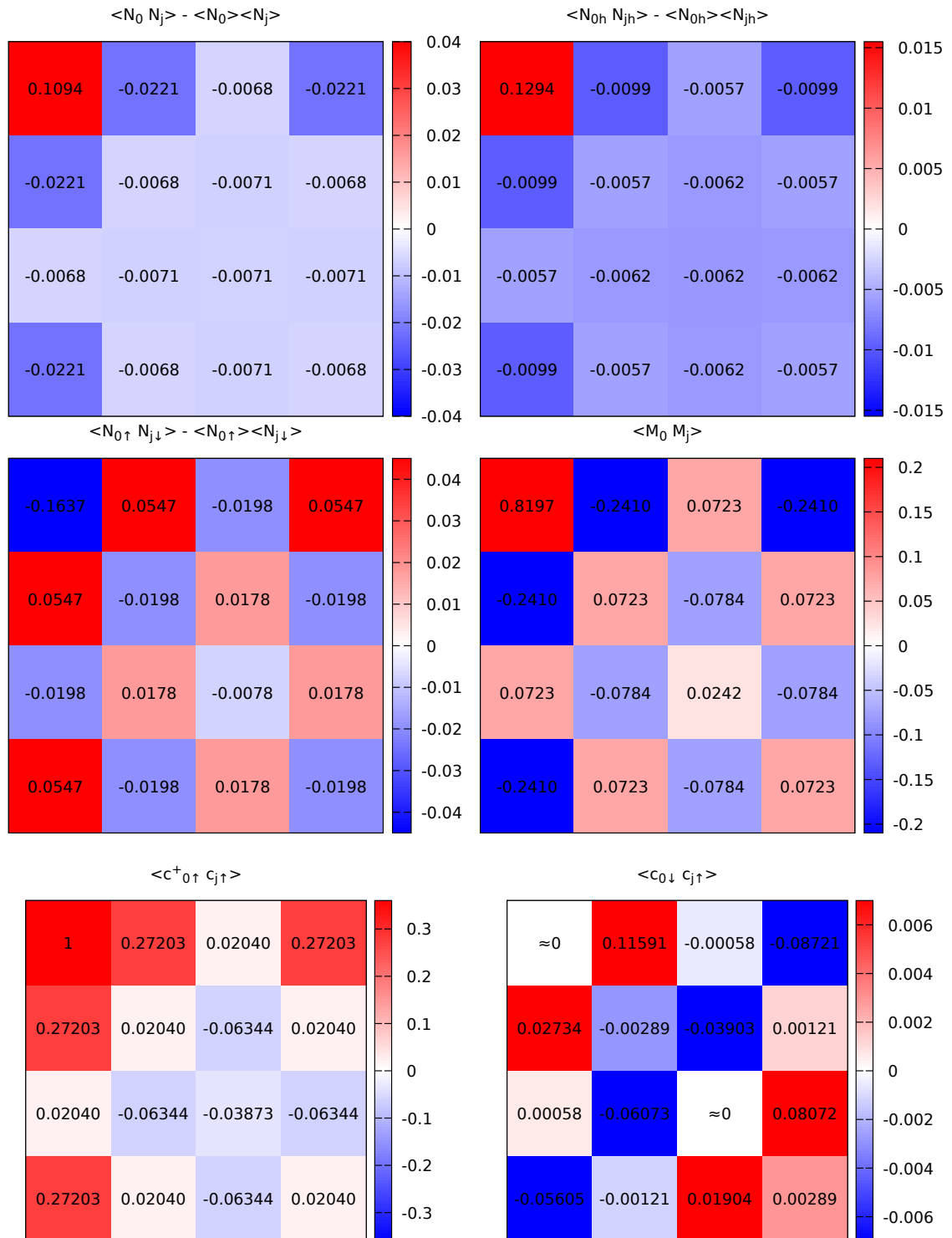
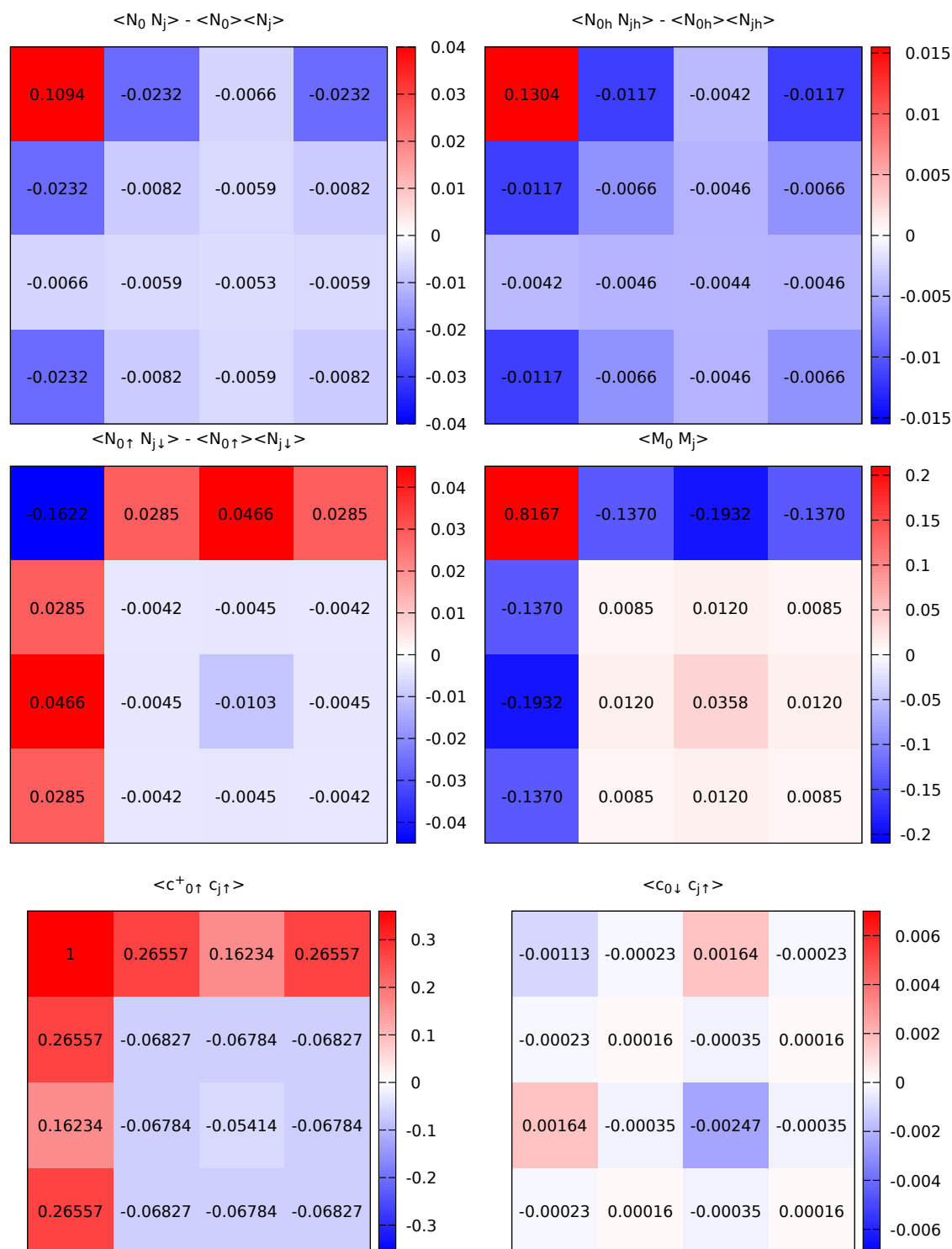


FIGURE 5.12: Exact Diagonalization static correlators in the ground state of the sector $(7_\uparrow, 7_\downarrow)$ (except bottom right $\langle 7_\uparrow, 7_\downarrow | c_{0\downarrow} c_{j\uparrow} | 8_\uparrow, 8_\downarrow \rangle$) of the periodic 4×4 cluster. Indices 0, 0 correspond to the top left corner of the grid. $U = 5.56$, $t' = 0$. For $t' = 0$ the ground state of $(7_\uparrow, 7_\downarrow)$ is 3 times degenerate, $\langle c_{0\downarrow} c_{j\uparrow} \rangle$ is shown for one of the eigenvectors.

FIGURE 5.13: 5.12 continued: $U = 5.56$, $t' = 0.15$.

FIGURE 5.14: 5.12 continued: $U = 5.56$, $t' = 0.3$.

FIGURE 5.15: 5.12 continued: $U = 10$, $t' = 0$.

FIGURE 5.16: 5.12 concluded: $U = 10$, $t' = 0.3$.

5.6 Dynamical averages in momentum space

Additionally, the momentum dependency of self-energy on the 0th Matsubara frequency (Fig. 5.18) and the \mathbf{k} -resolved spectral density (Fig. 5.20) were calculated. The conversion to momentum space was performed with the Fourier transform explained in Section 3.2.

As calculating the full set of ij for the 4×4 Hubbard cluster is very computationally demanding, requiring to calculate $16 \cdot 16 = 256$ combinations of sites, we use additional symmetries resulting from the periodicity, with the following set of non-equivalent pairs $\{i, j\}$ replicating the full G_{ij} and other ij -dependent observables:

$$\begin{aligned} \{0, 0\} \quad \mathbf{r} = \{0, 0\}, \{0, 5\} \quad \mathbf{r} = \{1, 1\}, \\ \{0, 1\} \quad \mathbf{r} = \{1, 0\}, \{0, 6\} \quad \mathbf{r} = \{2, 1\}, \\ \{0, 2\} \quad \mathbf{r} = \{2, 0\}, \{0, 10\} \quad \mathbf{r} = \{2, 2\}. \end{aligned}$$

Finite-size effects and the periodic boundary condition seem to cause overestimated contribution of components other than the local ($\{i, j\} = \{0, 0\}$), nearest-neighbour ($\{i, j\} = \{0, 1\}$) and next-nearest neighbour ($\{i, j\} = \{0, 5\}$) to $\Sigma_{\mathbf{k}}$, which results in a peculiar “wavy” shape in the \mathbf{k} -space (Fig. 5.17). This tendency can be offset by taking only the components $\{0, 0\}$, $\{0, 1\}$, $\{0, 5\}$ in the Fourier transform (Fig. 5.18).

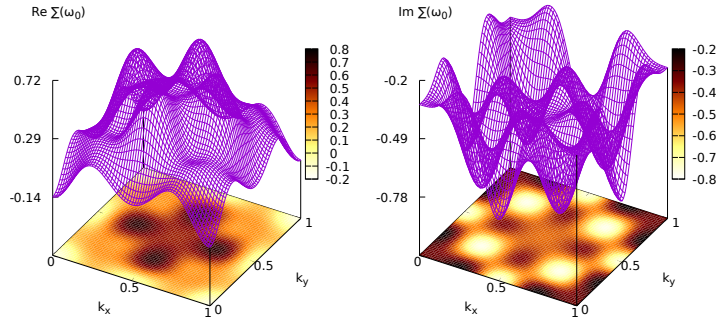


FIGURE 5.17: Exact Diagonalization self-energy $\Sigma(\mathbf{k}, i\omega_0)$ in the full Brillouin zone 64×64 \mathbf{k} -mesh on the lowest Matsubara frequency $i\omega_0$ in periodic 4×4 cluster with $\beta = 10$, sector $(7_\uparrow, 7_\downarrow)$, $\mu = 1.55$, $t' = 0.15$, $U = 5.56$.

Fourier transform from Σ_{ij} with all non-equivalent $\{i, j\}$.

The comparison of \mathbf{k} -resolved spectral density Fig. 5.20 for different values of t' shows that increase of t' flattens the conduction band. The general shape of the calculated spectral density is similar to the experimental band structure of a hole-doped cuprate Fig. 2.

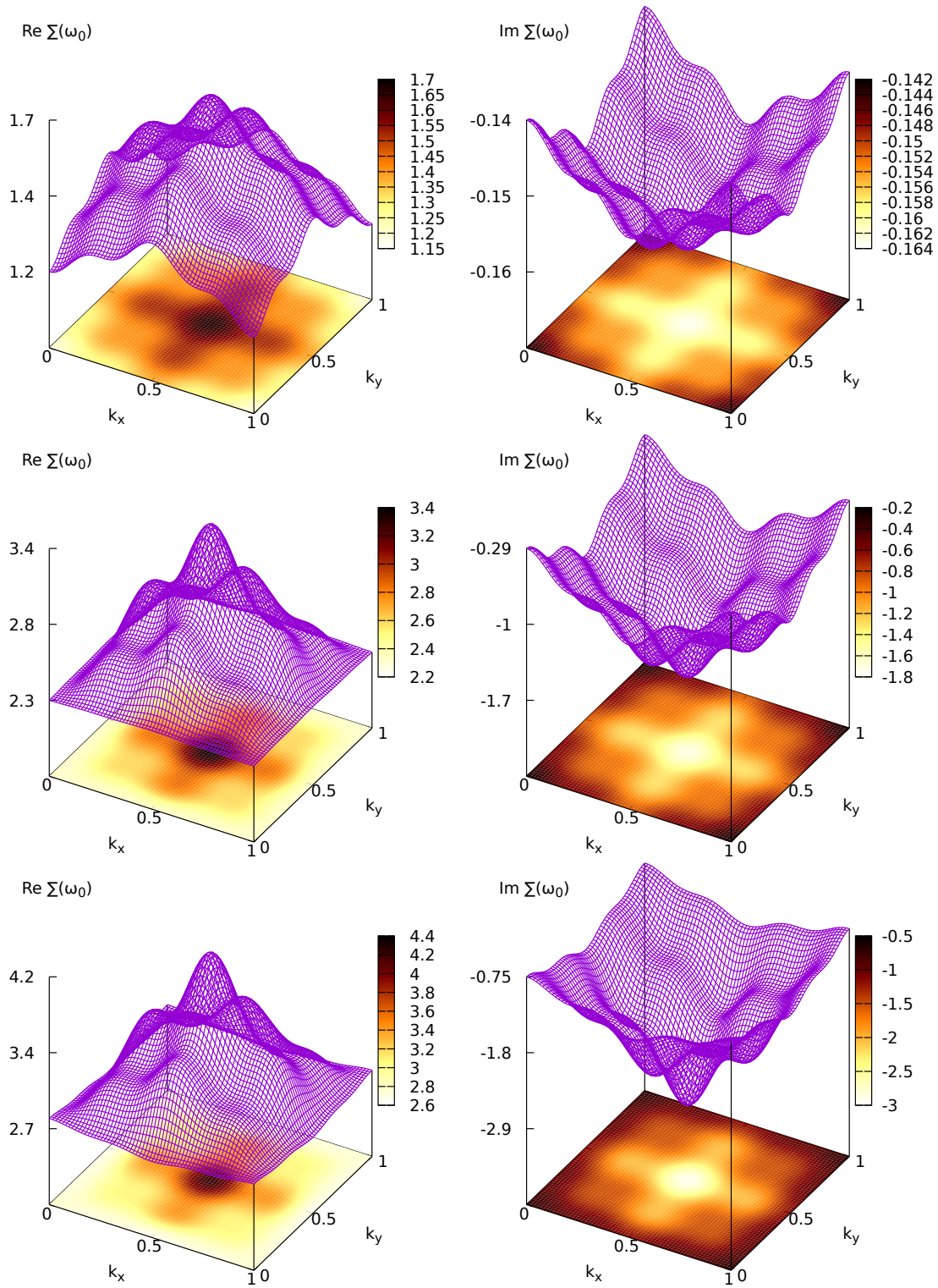
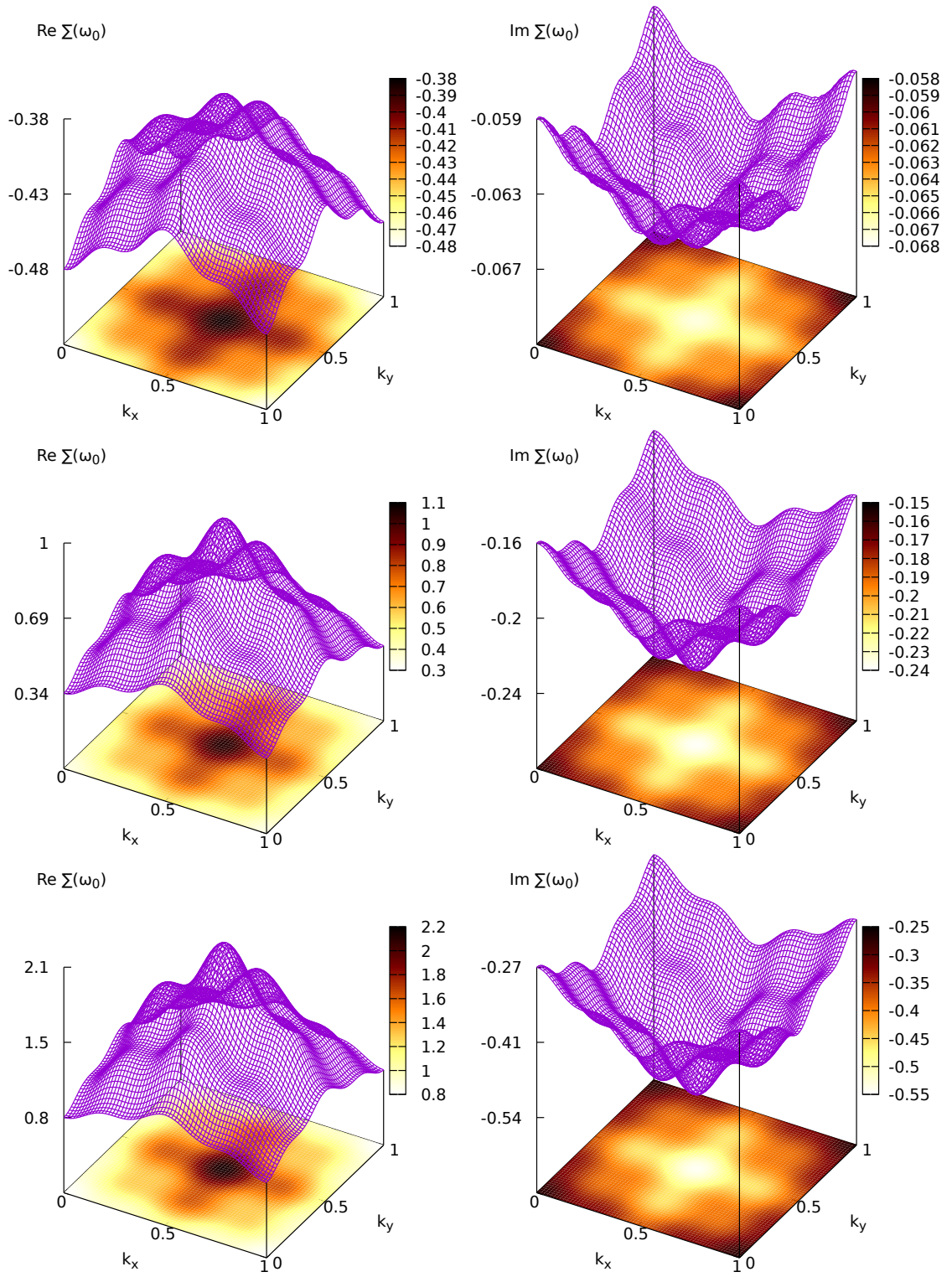


FIGURE 5.18: Exact Diagonalization self-energy $\Sigma(\mathbf{k}, i\omega_0)$ in the full Brillouin zone 64×64 \mathbf{k} -mesh on the lowest Matsubara frequency $i\omega_0$ in periodic 4×4 cluster with $\beta = 10$, sector $(7_\uparrow, 7_\downarrow)$. Top to bottom: $U = 3$, $U = 5.56$, $U = 7$.

Fourier transform from Σ_{ij} with non-equivalent $\{i, j\} = \{0, 0\}, \{0, 1\}, \{0, 5\}$. $\mu = 0$, $t' = 0.15$.

FIGURE 5.19: 5.18, concluded: $\mu = 1.55$, $t' = 0.3$.

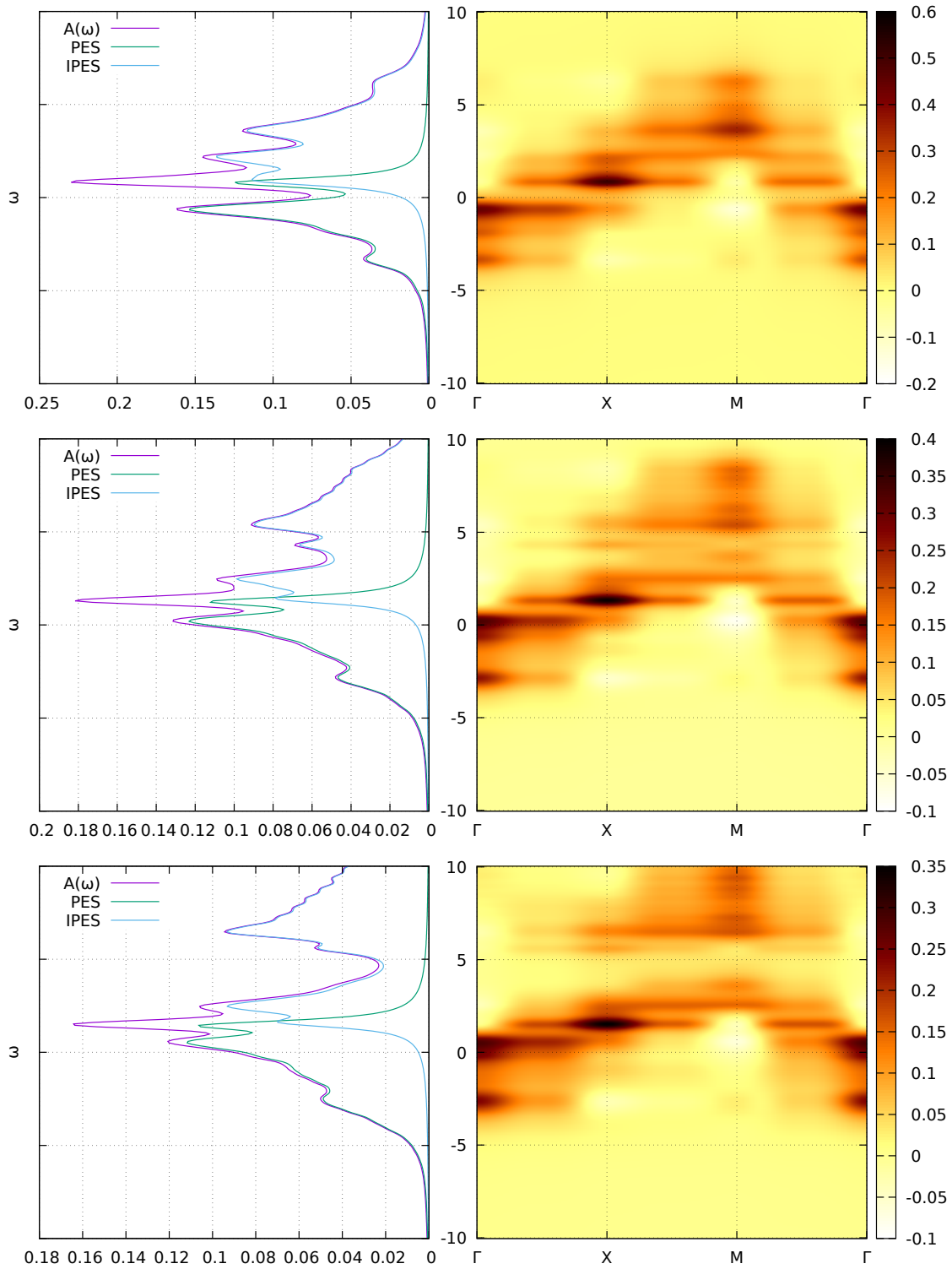
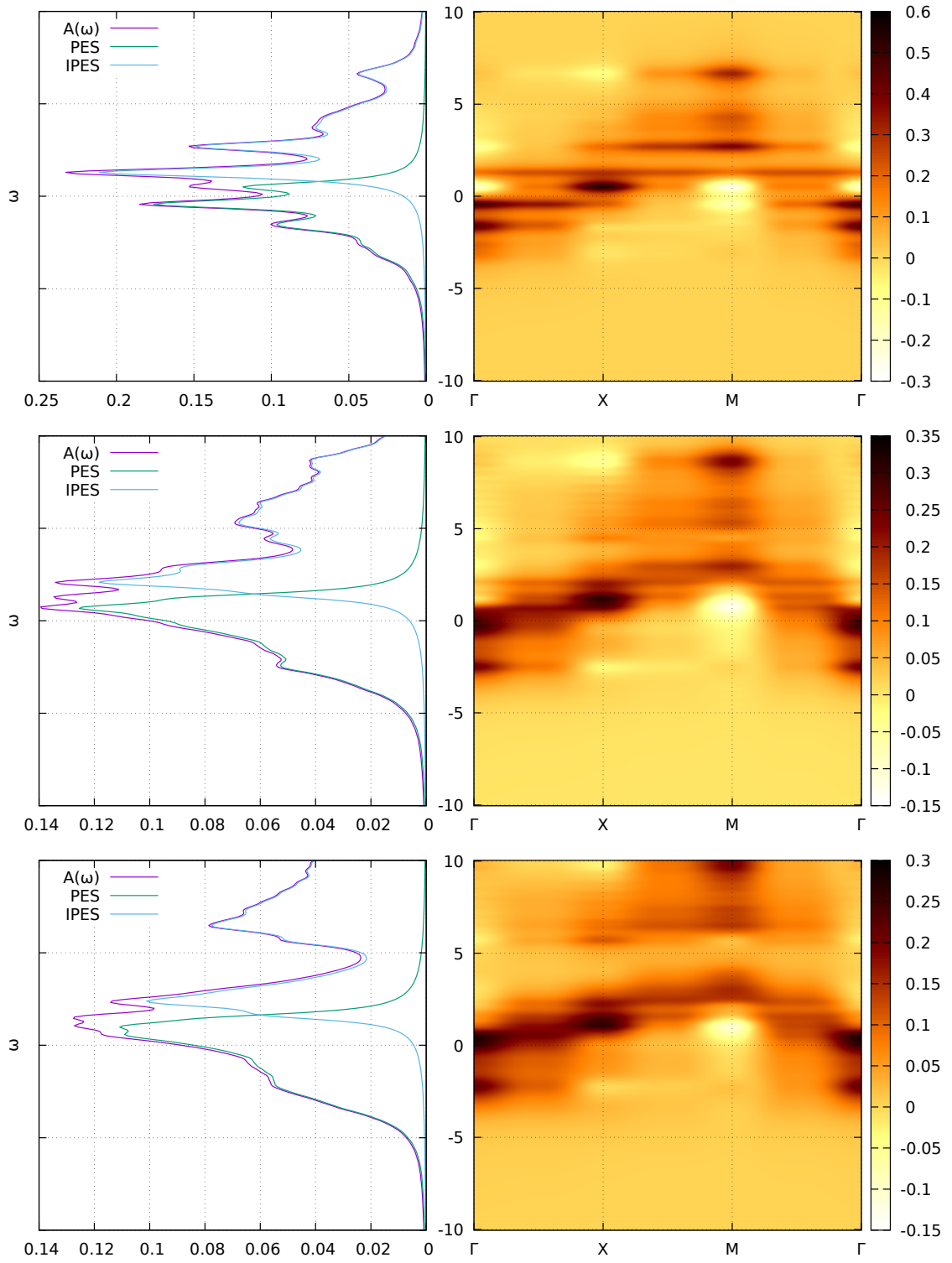
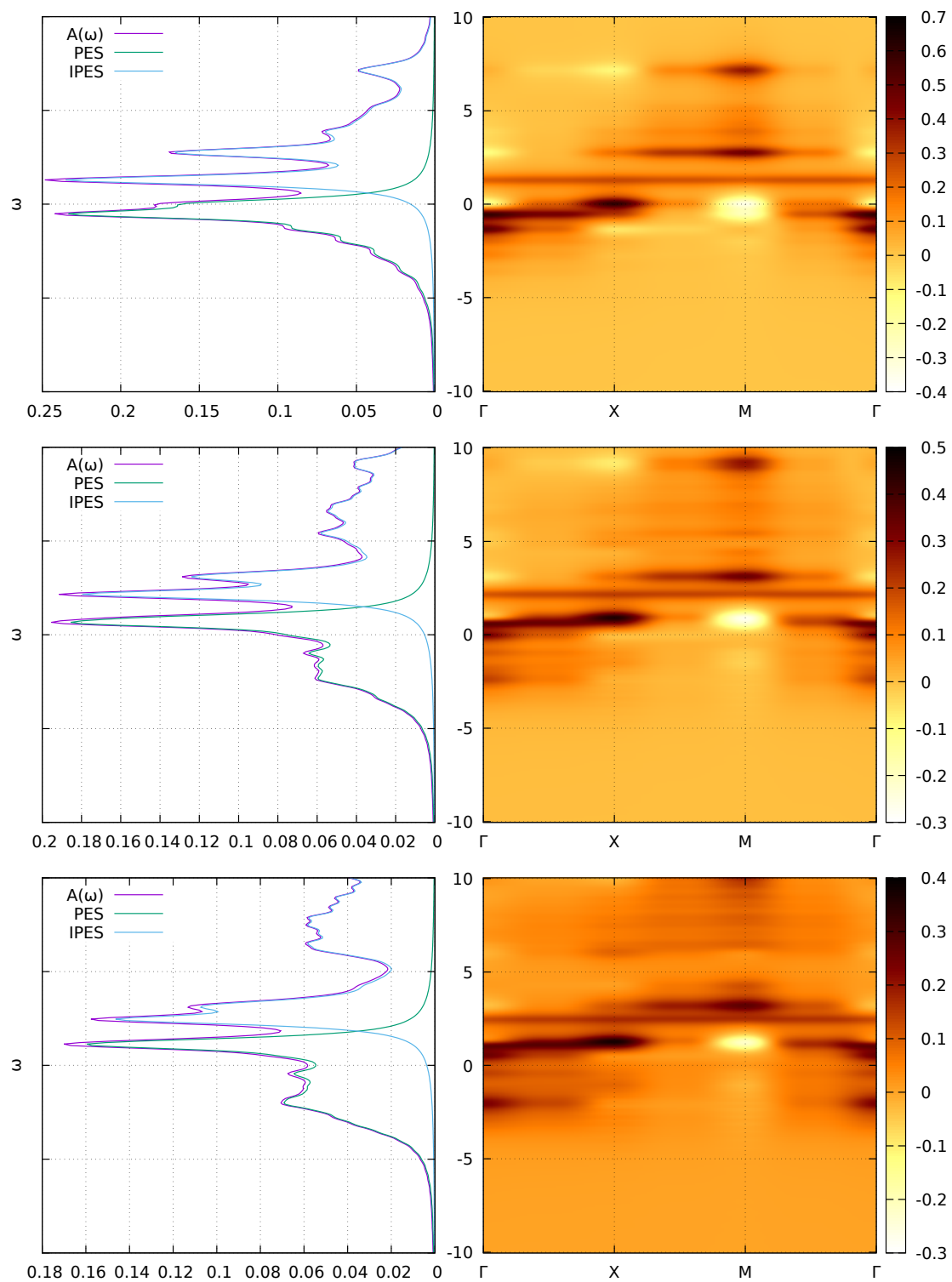


FIGURE 5.20: Exact Diagonalization density of states $A(\omega)$ (left), \mathbf{k} -resolved spectral density $A(\mathbf{k}, \omega)$ (right) in the Brillouin zone 64×64 \mathbf{k} -mesh of periodic 4×4 cluster with $\beta = 10$, sector $(7_{\uparrow}, 7_{\downarrow})$. Here Fermi level is at the energy where PES = IPES. Top to bottom: $U = 3$, $U = 5.56$, $U = 7$.

Fourier transform from G_{ij} with non-equivalent $\{i, j\} = \{0, 0\}, \{0, 1\}, \{0, 5\}$.
 $t' = 0$.

FIGURE 5.21: 5.20, continued: $t' = 0.15$.

FIGURE 5.22: 5.20, concluded: $t' = 0.3$.

Chapter 6

Complex network theory study of 4×4 Hubbard cluster

This chapter is based on our 2020 paper [13].

At first, the goal of extracting information about the tendency to form critical states out of small cluster solutions by means of exact diagonalization does not seem realistic, since studying systems in the critical regime unavoidably requires dealing with long-range correlations, while all the microscopic precursors of the transition on small lattices would be washed out by the finite-size effects. However, it is useful to bear in mind that, in the context of many-body quantum dynamics, the concept of entanglement and the phenomenon of collective emergence go hand in hand. An archetypical example of such relation is the Cooper pairs in the BCS theory of superconductivity: while the ground state wavefunction has a form of a product state of the Cooper pairs, each pair itself is a two-body entangled system. Therefore it is natural to expect that major transitions in phenomenological properties of many-body systems would be reflected in the patterns of entanglement, and quantum criticality should leave its fingerprint on all scales, not only in the deep infrared limit. A nice example of how fruitful this way of thinking can be was given in Refs. [130, 131], where entanglement measures were used to determine universality class of the Mott transition in the 2d Hubbard model.

Recently, a novel approach to phase transitions in quantum lattice models based on complex network theory has been suggested [127, 122]. It was noticed that a particular structure that can be computed with relative ease and appears to be very sensitive to reconfigurations of the quantum state is the network of quantum mutual information. The mutual information between two subsystems A and B of a larger systems is defined as

$$\mathcal{I}_{AB} = S_A + S_B - S_{A \cup B}, \quad (6.1)$$

where $S_A = -\text{Tr} \rho_A \log \rho_A$ is the von Neumann entropy, and $\rho_A = \text{Tr}_A \rho$ is the density matrix of subsystem A . Then we can associate a weighted graph with a state of a quantum lattice system, e.g. the Hubbard model, by considering the lattice

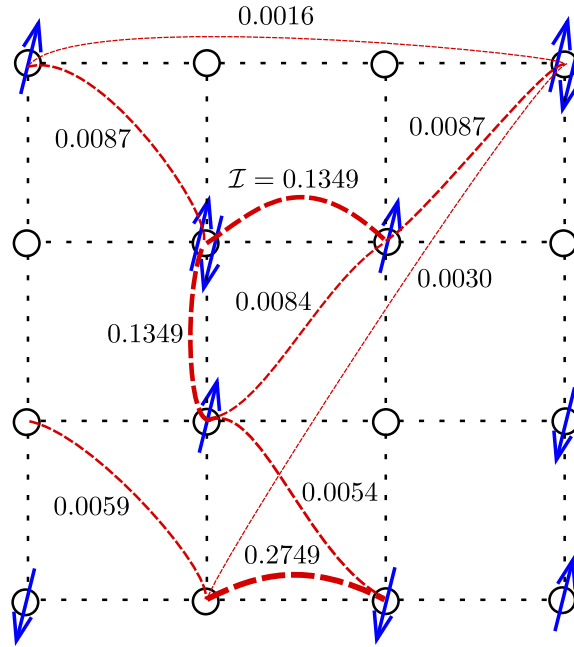


FIGURE 6.1: An artistic view of the mutual information complex network defined on the Hubbard lattice. While the network is fully connected, for illustrative purposes, only some of the network links are shown. The shown values of inter-site mutual information correspond to the case of non-periodic boundary conditions, $(6_{\uparrow}, 6_{\downarrow})$ sector, $U = 7.5$, $|t'| = 0.3$.

sites $i = 1 \dots N$, where N is the number of sites, as nodes of the graph, and the values of pairwise inter-site mutual information I_{ij} play the role of weights on the graph links (see Fig. 1). This representation is appealing for the following reason. Once a wave function on the lattice is known, it is easy to compute the entanglement entropy of a pair of sites and thus the mutual information. At the same time, such a network contains information of quantum correlations which could be very important to understand the dynamics of strongly correlated systems. In the cases of the transverse field Ising and the Bose-Hubbard models in 1d, it was demonstrated that certain characteristics of the mutual information network can be used to detect quantum phase transitions [127, 122]. Namely, behavior of the following functions upon changing parameters of the models has been studied:

- **Clustering** of a weighted graph is defined as

$$C = \frac{\text{Tr } \mathcal{I}^3}{\sum_{j \neq i}^N \sum_{i=1}^N [\mathcal{I}^2]_{ij}}, \quad (6.2)$$

where N is the total number of sites in the lattice, and \mathcal{I} is the $N \times N$ matrix of inter-site mutual information. One can see that this quantity maximizes on graphs with a lot of three-link loops with high weights. For the cases studied in Ref. [127], it was shown that it serves as sensitive detector that exhibits a clear dip at the phase transition point. A natural explanation of this fact is that, at the criticality, one can expect the corresponding network to be scale-free, and for generic scale-free networks clustering is usually quite low [68].

- **Disparity** of a single node in a network is defined as a measure to capture how non-uniformly weights on the links attached to this node are distributed:

$$Y_i = \frac{\sum_{j=1}^N (\mathcal{I}_{ij})^2}{\left(\sum_{j=1}^N \mathcal{I}_{ij}\right)^2} \quad (6.3)$$

For example, if the node has the same value of mutual information with all the other nodes of the network, its disparity would be $Y_i = 1/(N - 1)$, while if it correlates only with one neighbor, the disparity maximizes as $Y_i = 1$. Physically speaking, high disparity of a lattice site means that it tends to correlate only with a few other sites, and “factorize out” of the rest of the system. In the context of quantum many-body physics such a behavior would be typical for states that can be nearly decomposed into product states. On the other hand, low disparity means that the site correlates with a large number of degrees of freedom.

- **Density** is an overall characteristic of a network given by

$$D = \frac{1}{N(N-1)} \sum_{i,j=1}^N \mathcal{I}_{ij}, \quad (6.4)$$

i.e. it is the averaged fraction of all the weights (mutual information values) of the network. To gain more intuition on what properties of the many-body quantum state it reflects, we shall estimate an upper bound on this measure. If site i of the network is maximally entangled with the rest of the system, its entanglement entropy equals $S_i = \ln d = \ln 4$, where $d = 4$ is dimension of the local on-site Hilbert space in Hubbard model. On the other hand, mutual information monogamy theorem implies that $2S_i \geq \sum_{i,j} \mathcal{I}_{ij}$ [56], leading to

$$D \leq \frac{2}{N(N-1)} \sum_{i=1}^N S_i \leq \frac{2 \ln 4}{N-1} \xrightarrow{N \rightarrow \infty} 0 \quad (6.5)$$

i.e. the mutual information network is generally sparse even if the system is highly entangled. Note that bound (6.5) can be saturated in physically very distinct cases. D is maximal if either each single site is maximally entangled with just one partner site, and the state as a whole decomposes into a product of Bell pairs, or if the entanglement between the site and the rest of the system is homogeneously scrambled over all the sites. To distinguish between such configurations one has to refer to the disparity which defined above.

- **Pearson correlations** measure how much two nodes i and j of a network differ from each other:

$$r_{ij} = \frac{\sum_{k=1}^N (\mathcal{I}_{ik} - \langle \mathcal{I}_i \rangle) (\mathcal{I}_{jk} - \langle \mathcal{I}_j \rangle)}{\sqrt{\sum_{k=1}^N (\mathcal{I}_{ik} - \langle \mathcal{I}_i \rangle)^2} \sqrt{\sum_{k=1}^N (\mathcal{I}_{jk} - \langle \mathcal{I}_j \rangle)^2}}, \quad (6.6)$$

$$\langle \mathcal{I}_i \rangle = \frac{1}{N} \sum_{j=1}^N \mathcal{I}_{ij}$$

In Ref. [127] Pearson correlations of neighboring nodes were shown to develop a cusp around the phase transition point.

For one-dimensional Ising and Bose-Hubbard models [127], this approach to detecting quantum phase transitions points was successfully applied for systems of $\sim 10^2$ sites, and was demonstrated to be very robust upon finite-size effects. In the two-dimensional case, we are limited by much smaller system sizes (we perform exact diagonalization for a 4-by-4 plaquette), and should not expect our results to be free from finite-size artifacts. Still, as we shall see in the next section, the network measures exhibit clearly distinguishable features on a submanifold of the $t - t'$ Hubbard model parametric space. In particular, this submanifold includes the level-crossing point observed in a 2-by-2 plaquette for the choice of parameters corresponding to $\text{YBa}_2\text{Cu}_3\text{O}_7$ superconductor [53].

6.1 Results

The complex network measures discussed above have been computed across the space of parameters of a 4-by-4 $t - t'$ Hubbard plaquette. Within each fixed particle number sector, from $(5_\uparrow, 5_\downarrow)$ (37, 5% hole doping) to $(7_\uparrow, 7_\downarrow)$ (12, 5% hole doping), we scan over t' and U , Fig. 6.2. As an indicative value, we take $t' = 0.3$, which is estimated to be the next-neighbor hopping in the Hubbard model of YBaCuO compounds, and search for transition points around it. The temperature is fixed to $1/T = \beta = 100$ (all

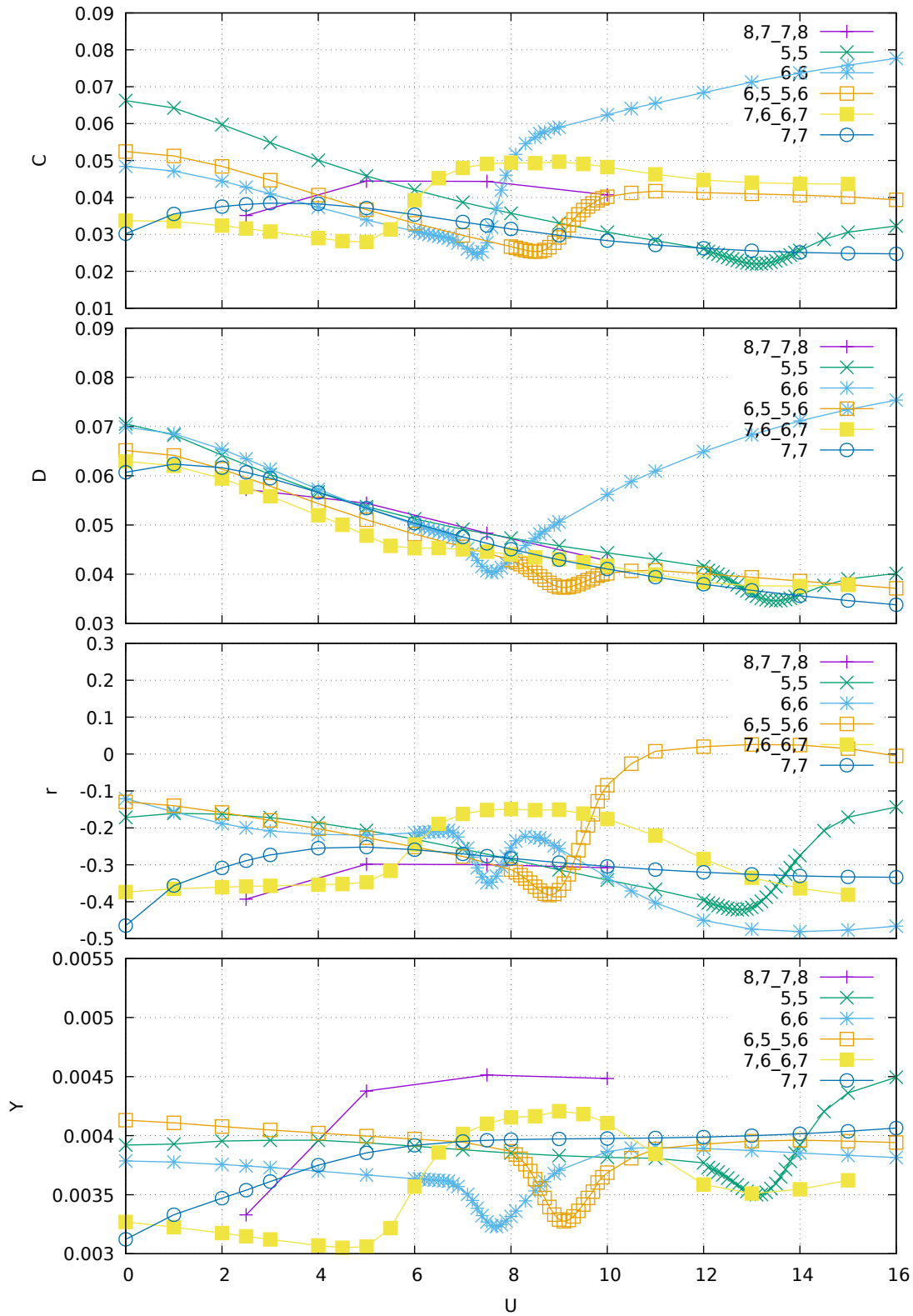


FIGURE 6.2: Characteristics of the mutual information complex network, – clustering C , density D , Pearson correlation r between neighboring sites in the middle of the 4-by-4 plaquette, and disparity Y of a site in the middle of the plaquette, – as functions of the on-site Coulomb repulsion U computed in different sectors for non-periodic boundary conditions. The hopping is $t' = 0.3$, the inverse temperature is $\beta = 100$.

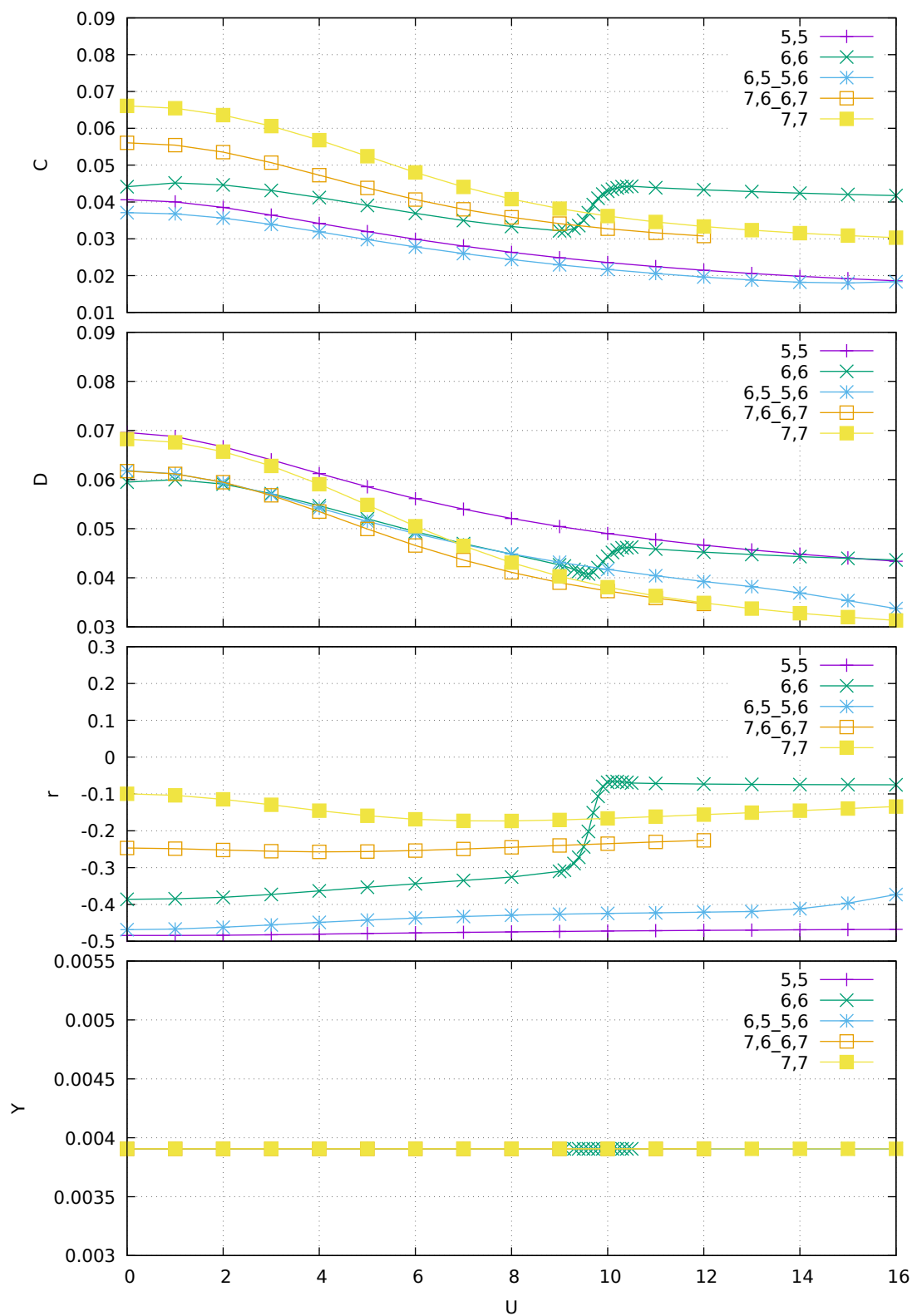


FIGURE 6.3: 6.2, concluded: with periodic boudary condition.

energies are expressed in the units of $|t|$, and the system is studied in the canonical ensemble.

We assume that a transition point is evident if all the measures exhibit some clear features around the same point. Accepting this criterion, we can claim with a high confidence that, for non-periodic boundary-conditions, there is a family of transition points in each sector (except $(7_{\uparrow}, 7_{\downarrow})$) forming a nearly perfect straight line in the $t' - U$ plane that extends in a certain range of t' ¹, Fig. 6.4 (for too small $|t'|$ the signs of criticality are faded away from the complexity measures). Moreover, for different values of hole doping, all these lines have very similar slope. This can be interpreted as that phase transition occurs on a 2d manifold in the 3d parametric $(U/t, t'/t, \text{particle number})$ space of the model.

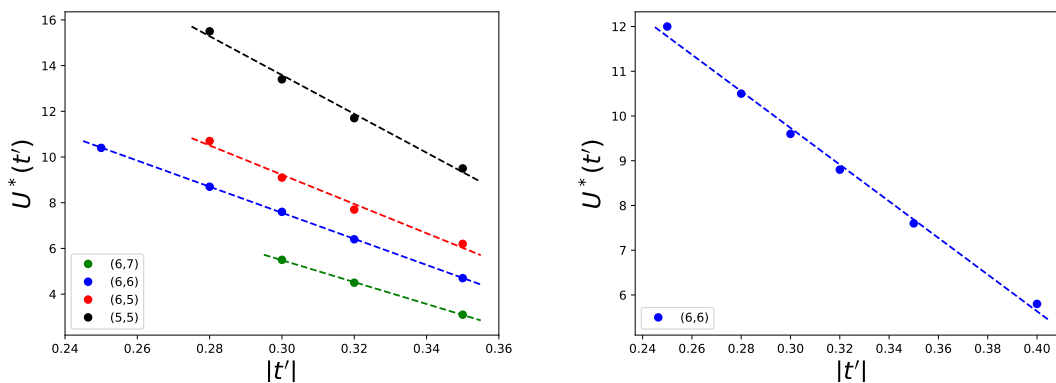


FIGURE 6.4: Dependence of the critical Coulomb repulsion U^* on the next-neighbor hopping t' for non-periodic (left) and periodic (right) boundary conditions at inverse temperature $\beta = 100$. The points correspond to locations of disparity minimum.

The features are more pronounced with non-periodic boundary conditions for the reason that the mutual information network has a richer structure in that case. If periodic boundary conditions are imposed, all lattice sites are identical, and every site has only five inequivalent connections to others, making the \mathcal{I}_{ij} matrix highly degenerate. Hence, the corresponding network structures are constrained by symmetries and much less sensitive to variations of the model parameters. When boundary conditions are changed for periodic ones, all the phase transition lines are smeared out with the only exception of the $(6_{\uparrow}, 6_{\downarrow})$ sector which corresponds to the hole doping of $\delta = 25\%$. For the latter, only the concrete values of Coulomb repulsion U gets shifted (see Additional results). While one can not expect the information network

¹For a more detailed picture of how complexity measures behave at different values of t' , see Additional results

constructed for periodic boundary to be sensitive enough to properly detect phase transitions, it is interesting to note that this single sector where the transition is evident for both choices of b.c. is the same as the one where level-crossing associated with formation of the pseudogap via Fano antiresonance occurs in a 2-by-2 plaquette [53].

6.2 Discussion

By associating the quantum state of the $t - t'$ Hubbard model with a weighted network of inter-site mutual information, for different values of the next-neighbor hopping t' , a set of transition lines was found in the $U - t'$ plane of the model parametric space, where characteristics of the network have a clearly distinguishable cusp. Such a behavior was previously shown to be an indication of quantum phase transitions in different one-dimensional models [127, 122]. The modern experimental understanding of the putative QCP in cuprates tells that it must be associated with the emergence of the pseudogap phase [61]. For example, for YBaCuO compounds the onset of pseudogap was experimentally demonstrated to happen at hole doping $\delta \simeq 22\%$ [113]. The hole doping $\delta = 25\%$ is the closest value one can get for a 4-by-4 cluster (the $(6_{\uparrow}, 6_{\downarrow})$ sector), and, interestingly, it is exactly the sector where the complex network measures demonstrate the most robust transition features. The particular value of the on-site Coulomb repulsion is affected by the finite size effects, and estimated to be about $U \simeq 7 - 8$ for $t' = 0.3$, which exceeds by $\sim 40\%$ the optimal $U \simeq 5.56$ indicated by the Dual Fermion study (Chapter 4). This discrepancy increases for the periodic boundary condition (Fig. 6.4): $U \simeq 9.5$, which exceeds by $\sim 70\%$.

Both the strength and the weakness of the employed approach is that it helps to identify *any* critical point while being ignorant about its nature. Therefore the existence of a manifold of QCP can be claimed in the $t - t'$ Hubbard model with a high confidence, but we cannot deduce what order parameter of the corresponding transition is. Still, we tend to relate the observed transition to the critical point discussed in [53], where it was associated with emergence of soft fermion modes.

6.3 Additional results

This section provides the results for the dependence of complex network measures on Coulomb repulsion U at different values of the hopping t' . It also shows the figures for the periodic boundary conditions, where the transition point is only evident for the $(6_{\uparrow}, 6_{\downarrow})$ sector. In the case of the periodic b.c. the disparity $Y = 0.00390625$ independently of U or t' .

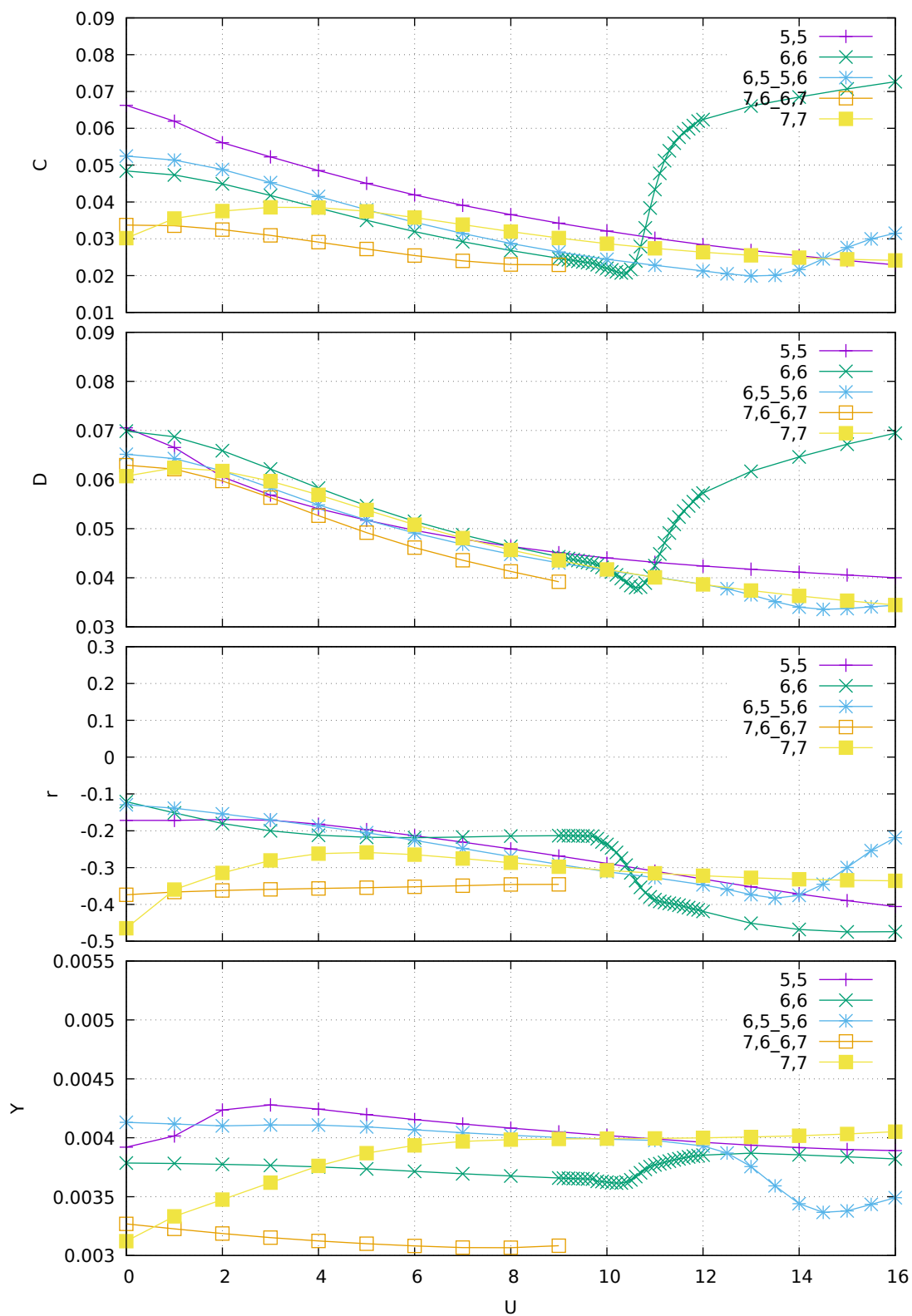
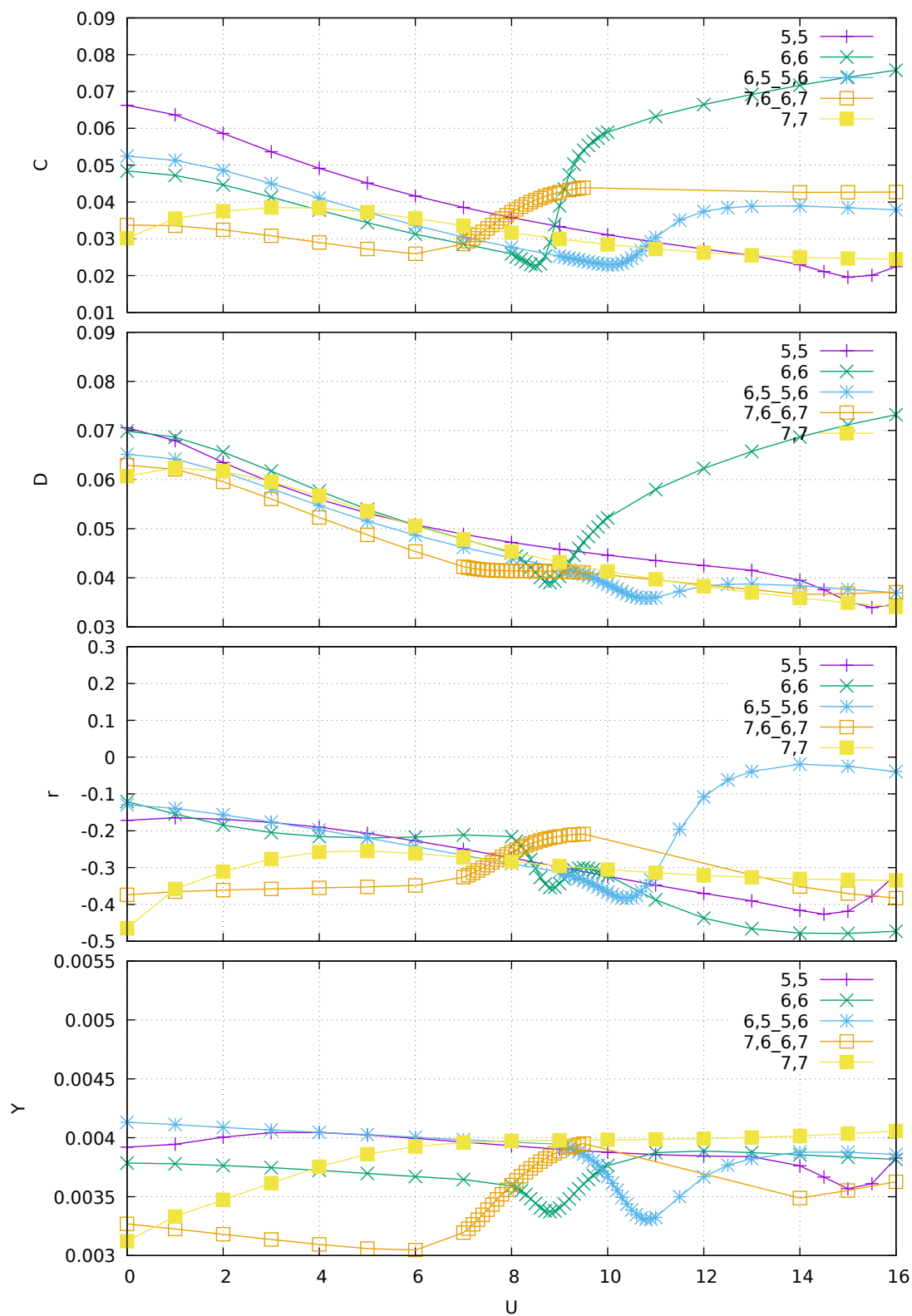


FIGURE 6.5: Characteristics of the mutual information complex network for non-periodic boundary conditions.
 $t' = 0.25$, $\beta = 100$.

FIGURE 6.6: 6.5, continued: $t' = 0.28$, $\beta = 100$.

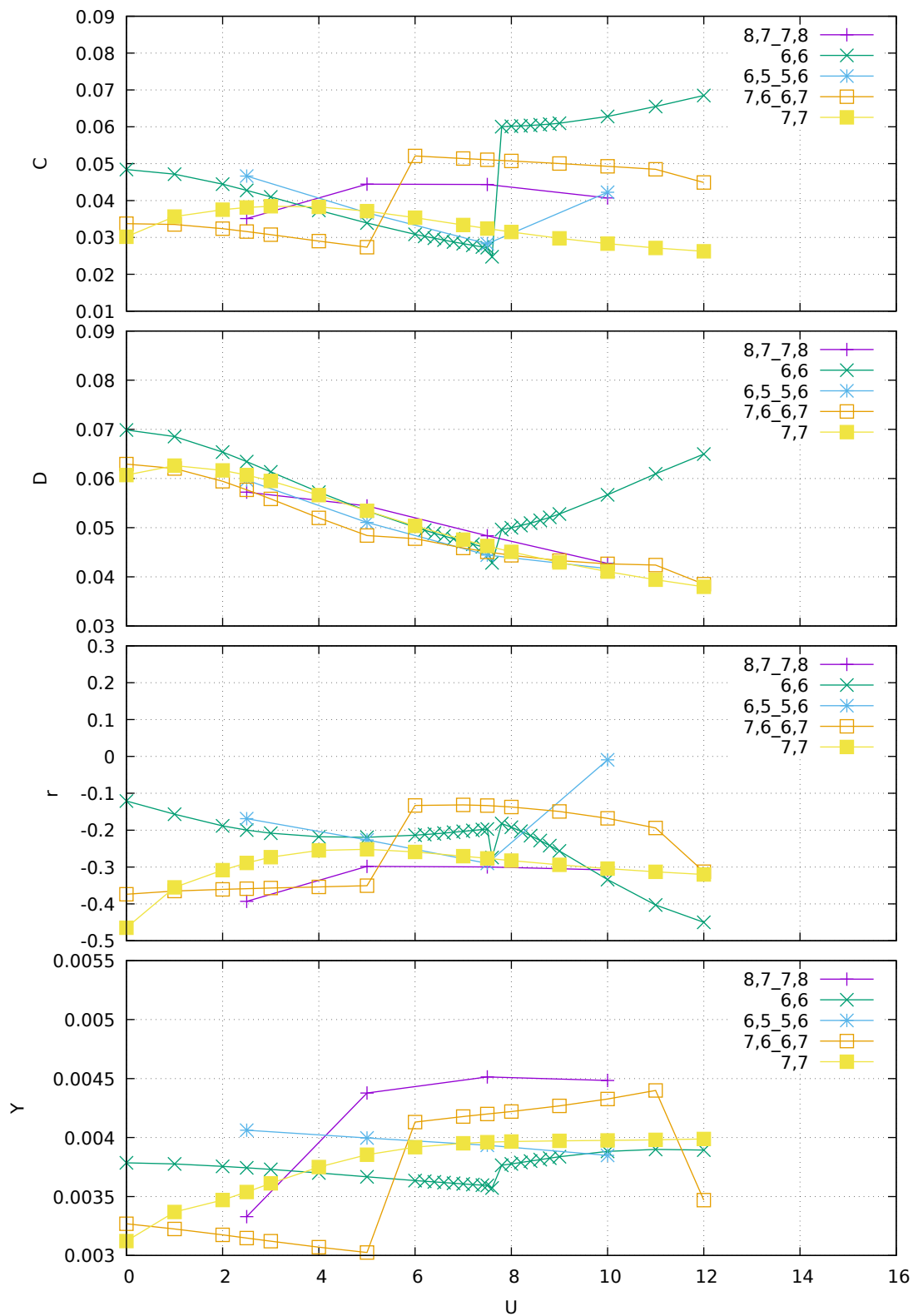
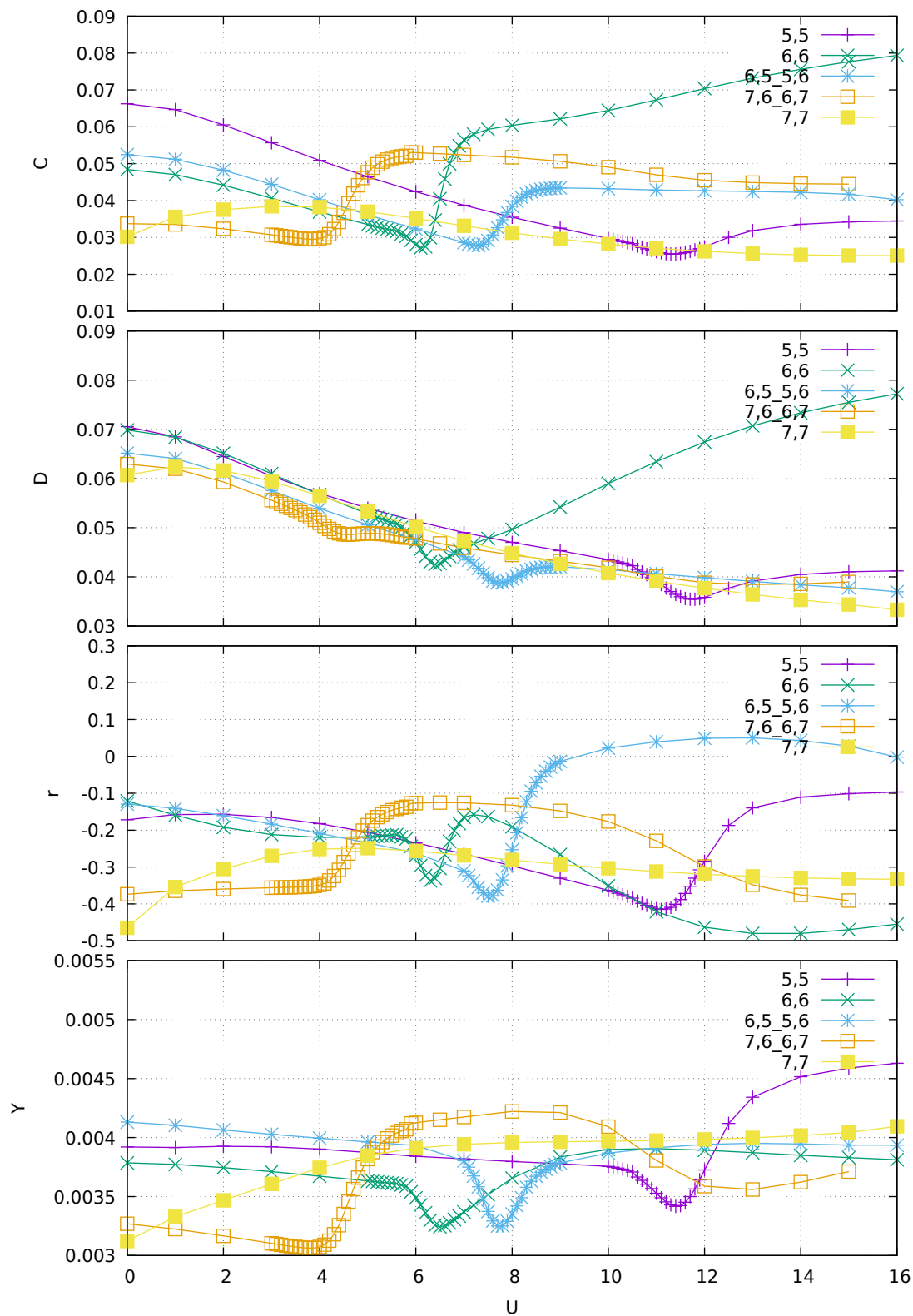
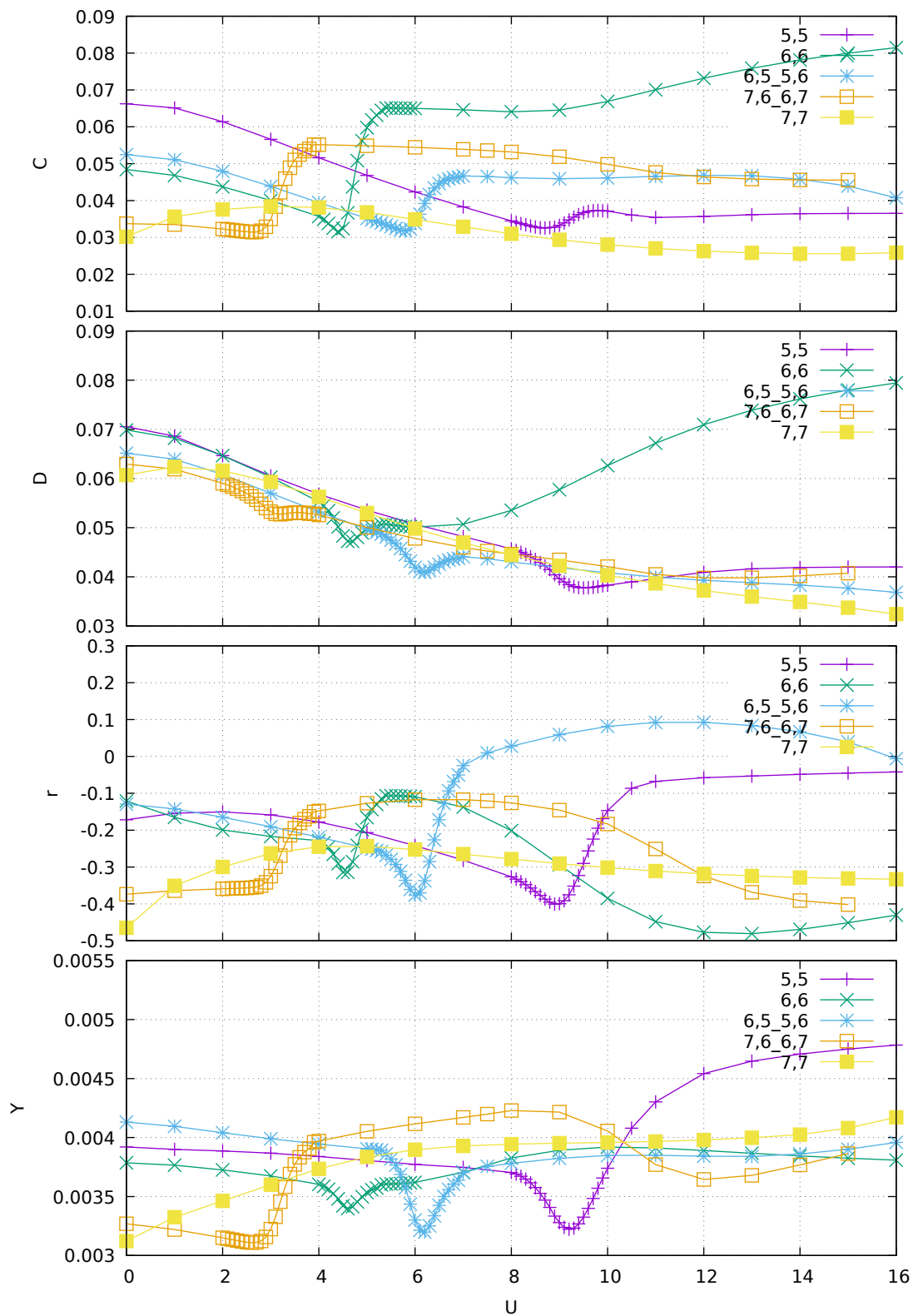
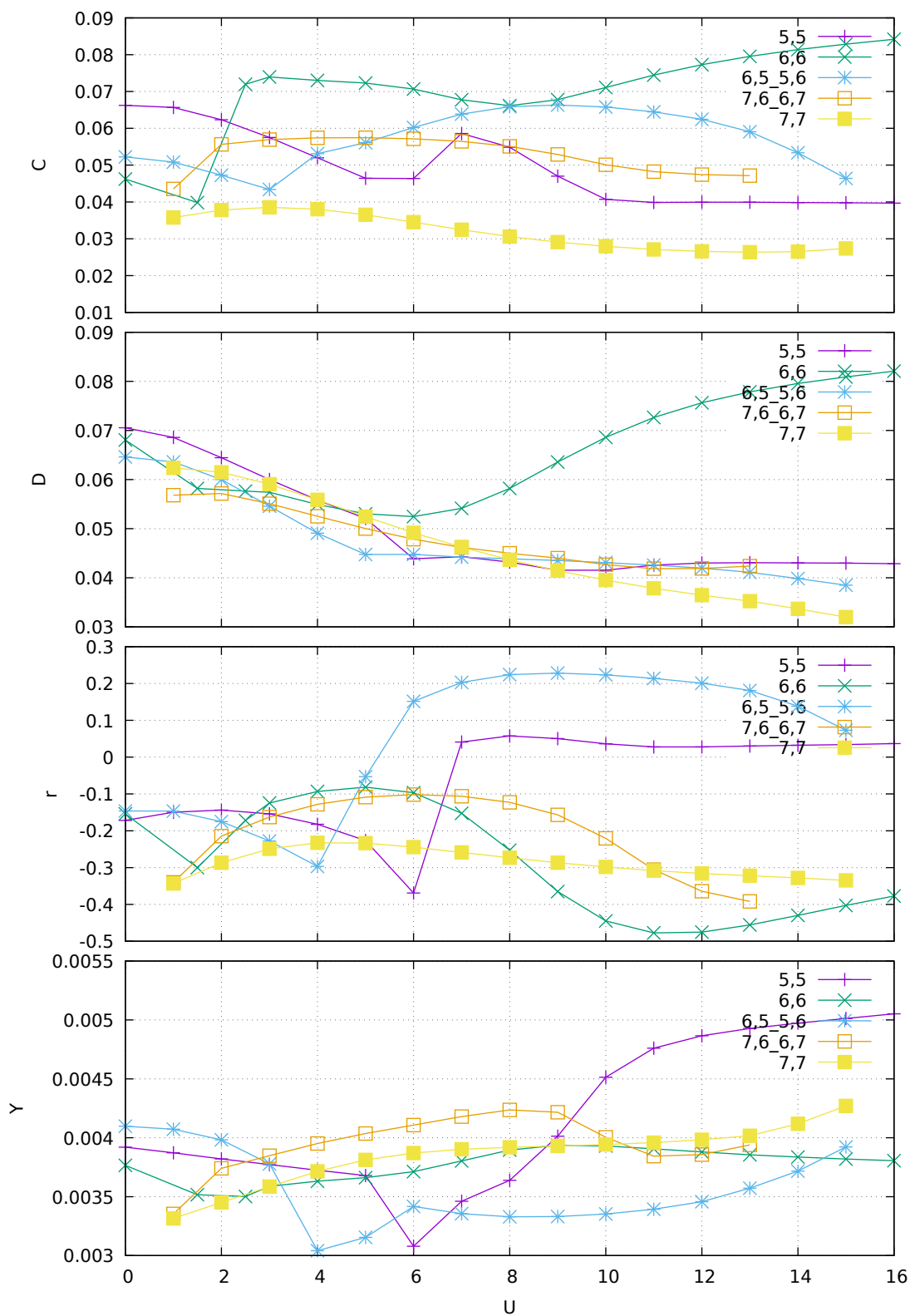


FIGURE 6.7: 6.5, continued: $t' = 0.3$, $\beta = 1000$.
 $t' = 0.3$ $\beta = 100$ is omitted here: see Fig. 6.2.

FIGURE 6.8: 6.5, continued: $t' = 0.32$, $\beta = 100$.

FIGURE 6.9: 6.5, continued: $t' = 0.35$, $\beta = 100$.

FIGURE 6.10: 6.5, continued: $t' = 0.4$, $\beta = 100$.

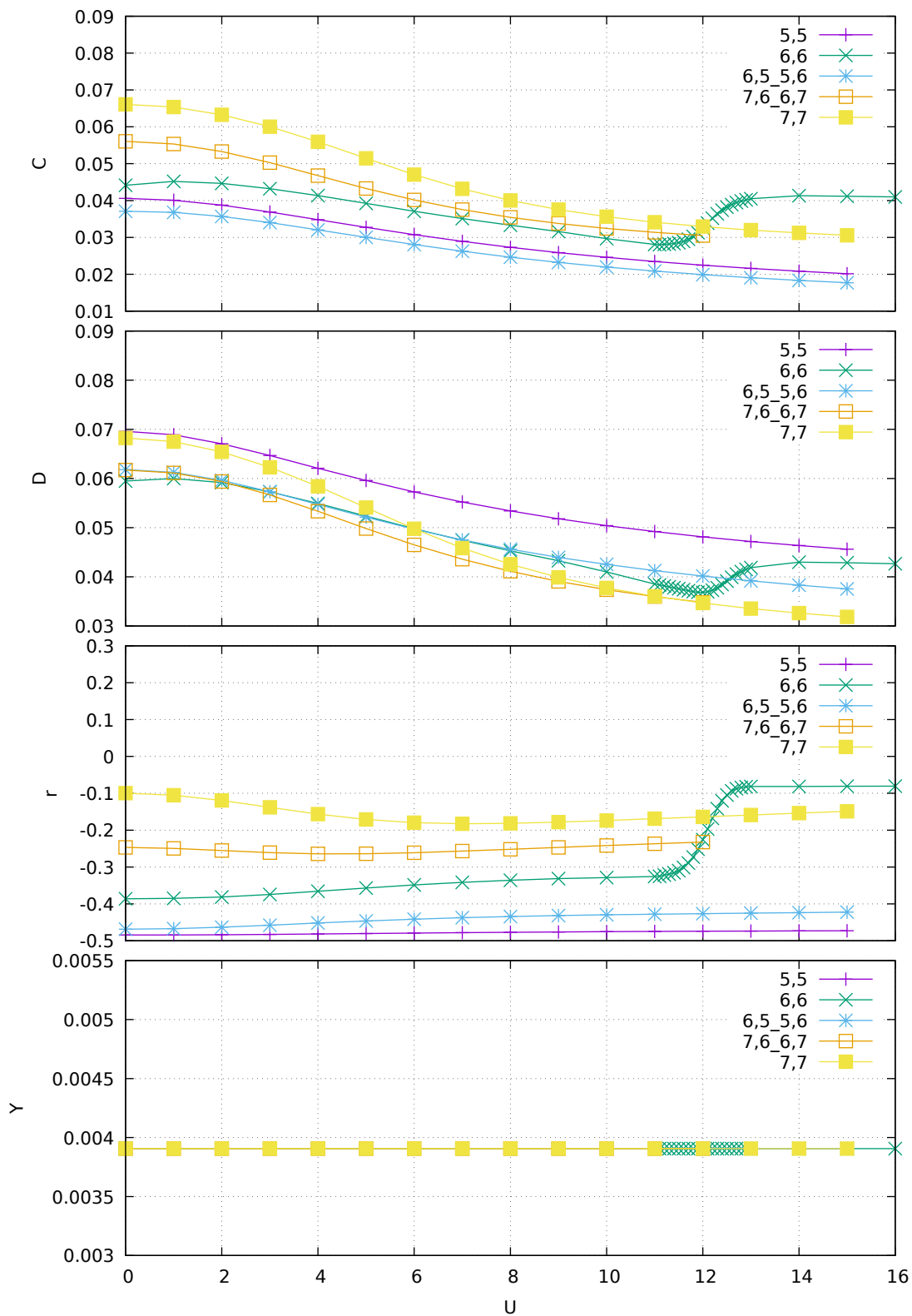


FIGURE 6.11: Characteristics of the mutual information complex network for periodic boundary conditions.
 $t' = 0.25$, $\beta = 100$.

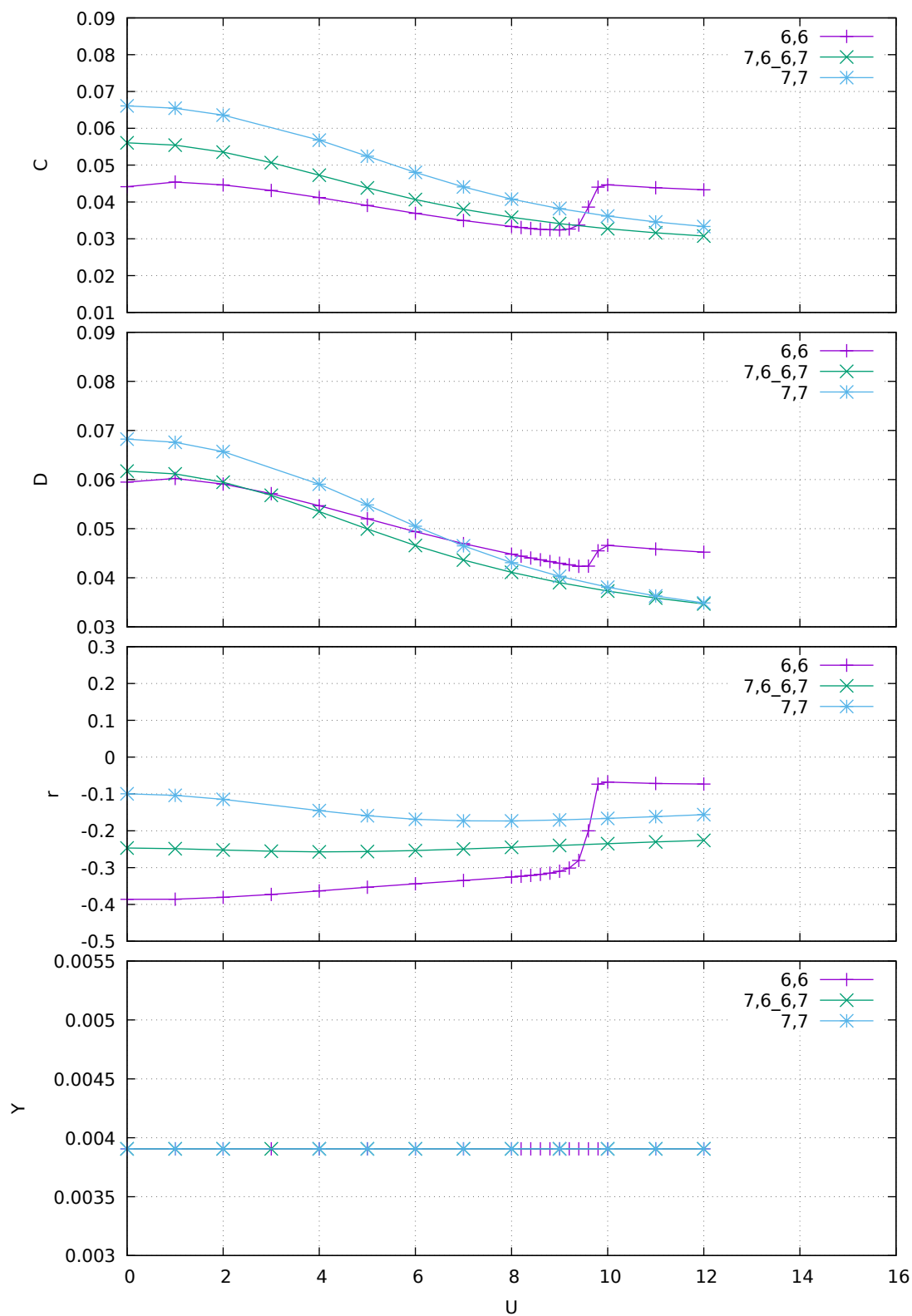


FIGURE 6.12: 6.11, continued: $t' = 0.3$, $\beta = 1000$. $t' = 0.3$ $\beta = 100$ is omitted here: see Fig. 6.3.

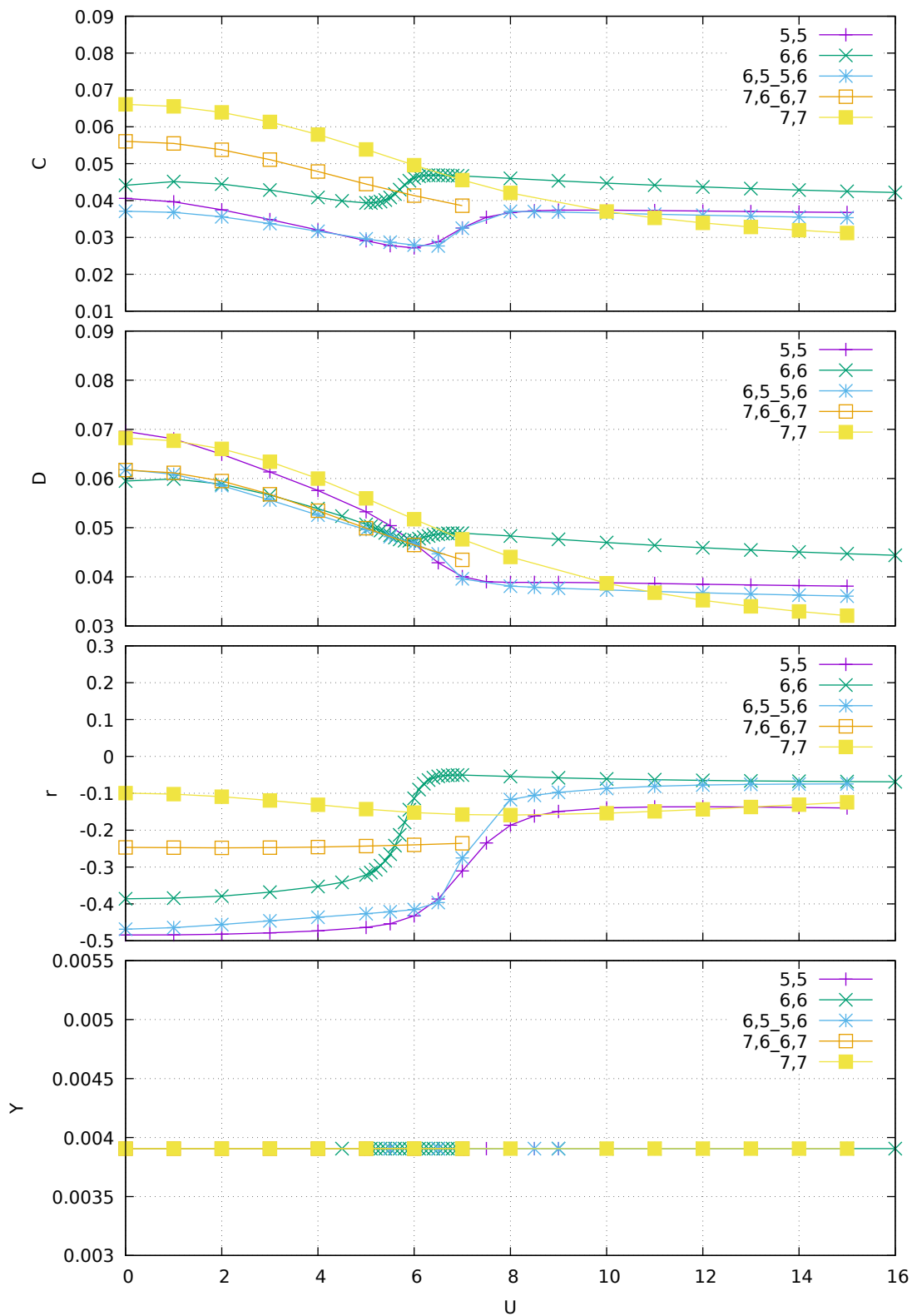


FIGURE 6.13: 6.11, concluded: $t' = 0.4$, $\beta = 100$.

Summary and outlook

The mainline of this thesis is the study of the hole-doped Hubbard model by means of Exact Diagonalization, Dual Fermion and Complex Network Theory approaches. By tuning the model's parameters we could observe the formation of a pseudogap, suppression of antiferromagnetism, a peak in hole pair binding energy and a shift in quantum entanglement, indicating the presence of a quantum critical point.

Below is a brief outline of the results.

- The following **methods** were used for this study. Exact Diagonalization is able to obtain many properties of a finite Hubbard model that takes into account electron-electron correlations important for the description of HTSC in cuprates. However, the standalone use of this approach is limited to relatively small systems which may introduce finite-size effects. Cluster Dual Fermion method approximates the solution of an infinite lattice with self-consistent diagrammatic expansion around the solution of a finite reference system, for example the one solved by Exact Diagonalization. The two schemes can thus be combined to build a powerful toolchain for the study of the Hubbard model. The methods are not affected by the fermionic sign problem, allowing for direct calculations on real frequencies, and do not experience and sizable numerical artifacts, making them robust and reproducible.

In cooperation with Isakov S.N. an efficient numerical scheme was developed for the Exact Diagonalization, allowing to study relatively large clusters on commonly available hardware, and both methods have been realized as extensible open source software packages [36, 103] that can be modified to solve other large models or calculate other properties. The thesis provides a concise explanation of the methods and all technical aspects necessary for their optimal use, which should allow the reader to understand existing software implementations or create their own.

- **Exact Diagonalization of 2×2 Hubbard plaquette** was the starting point of this research. The phase diagram of the number of electrons in its ground state versus t' , U and μ reproduces the diagram from [53], in particular the highly degenerate point at $t' = 0.15$, $U = 5.56$, $\mu = 0.479$, in which the input data for the Dual Fermion method was calculated. Additionally, the \mathbf{k} -resolved spectral density $A(\mathbf{k}, \omega)$ and momentum dependency of the self-energy $\Sigma(i\omega_0)$ of the plaquette were visualized in the degenerate point.

• **Dual Fermion study of 2×2 plaquette.** The physics of cuprate superconductors with the clear existence of a quantum critical point at $\delta_c \approx 0.24$ are closely related to the degeneracy of the plaquette in the strong-coupling regime. In this sense, the plaquette and not the single site can be considered the minimal building block for cuprate physics. The renormalized dual fermion perturbation starting from the plaquette reference system with $\delta = 0.25$ uncovers consequences of this degeneracy for the Green's function in the lattice and shows the basic mechanism of superconducting instability in cuprates via the Bethe-Salpeter equation.

• **Exact Diagonalization of 4×4 Hubbard cluster** – an interconnected system of 4 plaquettes with periodic boundary condition – supports strong pair-binding related with the next-nearest hoppings t' . and shows that both t' and U play an important role in the pairing energy gain, and that optimal value of U increases with t' . Given their large binding energy, these pairs should probably exist also at much higher temperatures than the superconducting critical temperature, remaining noncoherent. Static correlators show the suppression of antiferromagnetism by t' . Density of states calculated for different combinations of t' , U and δ is showing a pseudogap emerging for doping $\delta = 0.125$ and $U = 5.56$ when t' is increased from $t' = 0.15$ to $t' = 0.3$. With the increase of cluster size from 2×2 to 4×4 density of states changes from a peak at Fermi level to a pseudogap, which indicates the existence of effects with a longer range than the size of 2×2 plaquette. The formation of the pseudogap is related to a Fano-like effect originating from the sharply peaked DOS in the isolated plaquette embedded into the band of surrounding fermions, as was hypothesised in Ref. [53]. In the overdoped regime $\delta \geq 0.25$ the strong charge fluctuations restore formation of the normal metallic phase. The comparison of \mathbf{k} -resolved spectral density $A(\mathbf{k}, \omega)$ for 2×2 and 4×4 clusters which have the bandwidth $4t$ to the cuprate band structure Fig. 2 with the bandwidth of $8t = 4eV$ suggests that our unit of t corresponds to the energy $t = 0.5eV$. For more quantitative predictions of the theoretical phase diagram, the optimal dynamical embedding of the plaquette and the implications for the resulting perturbation theory need to be studied further.

• **Complex network theory study of 4×4 Hubbard cluster** supports the existence of quantum critical point and that a phase transition occurs on a two-dimensional manifold of δ , t' and U . The indicated optimal Coulomb for non-periodic boundary condition is $U \simeq 7 - 8$ for $t' = 0.3$, is greater than the expected optimal $U \simeq 5.56$ by $\sim 40\%$, and $U \simeq 9.5$ for periodic boundary, greater by $\sim 70\%$. Considering the fact that the complex network characteristics lose sensitivity due to the symmetries of periodic boundary condition, this level of agreement seems satisfactory.

• **Further research.** The approaches used in this thesis will be very useful for the interpretation of new experimental data on cuprate-based superconductors. Interesting possibilities exist for their future development, such as:

- implementing with EDLib the calculation of vertex function γ for the 4×4 Hubbard cluster, which would allow to study the cluster with the Dual Fermion approach;
- reconciling the results of complex network theory method by improving the handling of periodic boundary condition or establishing a mapping between the periodic and non-periodic clusters;
- the calculation of momentum-space charge and spin susceptibilities of BSCCO superconductors.

Bibliography

- [1] L.P. Gorkov A.A. Abrikosov and I.E. Dzialoshinski. *Methods of quantum field theory in statistical physics*. New York, NY: Dover, 1975.
- [2] Ferdinando Mancini Adolfo Avella. *Strongly Correlated Systems: Numerical Methods*. Berlin Heidelberg: Springer, 2013.
- [3] I Affleck. “Exact results on the dimerisation transition in SU(n) antiferromagnetic chains”. In: *Journal of Physics: Condensed Matter* 2.2 (Jan. 1990), pp. 405–415. DOI: [10.1088/0953-8984/2/2/016](https://doi.org/10.1088/0953-8984/2/2/016). URL: <https://doi.org/10.1088/0953-8984/2/2/016>.
- [4] Michael Danilov et. al. “Supplemental Materials”. In: (July 2021).
- [5] Ehud Altman and Assa Auerbach. “Plaquette boson-fermion model of cuprates”. In: *Phys. Rev. B* 65 (10 Feb. 2002), p. 104508. DOI: [10.1103/PhysRevB.65.104508](https://link.aps.org/doi/10.1103/PhysRevB.65.104508). URL: <https://link.aps.org/doi/10.1103/PhysRevB.65.104508>.
- [6] O. K. Andersen, O. Jepsen, A. I. Liechtenstein, and I. I. Mazin. “Plane dimpling and saddle-point bifurcation in the band structures of optimally doped high-temperature superconductors: A tight-binding model”. In: *Phys. Rev. B* 49 (6 Feb. 1994), pp. 4145–4157. DOI: [10.1103/PhysRevB.49.4145](https://link.aps.org/doi/10.1103/PhysRevB.49.4145). URL: <https://link.aps.org/doi/10.1103/PhysRevB.49.4145>.
- [7] O.K. Andersen, A.I. Liechtenstein, O. Jepsen, and F. Paulsen. “LDA energy bands, low-energy hamiltonians, t' , t'' , $t_{\perp}(k)$, and J_{\perp} ”. In: *Journal of Physics and Chemistry of Solids* 56.12 (1995). Proceedings of the Conference on Spectroscopies in Novel Superconductors, pp. 1573–1591. ISSN: 0022-3697. DOI: [https://doi.org/10.1016/0022-3697\(95\)00269-3](https://doi.org/10.1016/0022-3697(95)00269-3). URL: <https://www.sciencedirect.com/science/article/pii/0022369795002693>.
- [8] P. W. Anderson. “Localized Magnetic States in Metals”. In: *Phys. Rev.* 124 (1 Oct. 1961), pp. 41–53. DOI: [10.1103/PhysRev.124.41](https://link.aps.org/doi/10.1103/PhysRev.124.41). URL: [http://link.aps.org/doi/10.1103/PhysRev.124.41](https://link.aps.org/doi/10.1103/PhysRev.124.41).
- [9] P. W. Anderson. “The Resonating Valence Bond State in La_2CuO_4 and Superconductivity”. In: *Science* 235.4793 (1987), pp. 1196–1198. ISSN: 00368075, 10959203. URL: <http://www.jstor.org/stable/1698247>.

- [10] P.W. Anderson. *The Theory of Superconductivity in the High- T_c Cuprates*. Princeton: Princeton University Press, 2007.
- [11] *ARPACK-NG: A new generation of implicitly restarted Arnoldi library*. <https://github.com/opencollab/arpack-ng>. 2016. URL: <https://github.com/opencollab/arpack-ng>.
- [12] J. Ayres, M. Berben, M. Culo, Y. -T. Hsu, E. van Heumen, Y. Huang, J. Zaanen, T. Kondo, T. Takeuchi, J. R. Cooper, C. Putzke, S. Friedemann, A. Carrington, and N. E. Hussey. “Incoherent transport across the strange metal regime of highly overdoped cuprates”. In: *Nature* (2021). arXiv: [2012.01208](https://arxiv.org/abs/2012.01208) [[cond-mat.str-el](https://arxiv.org/abs/2012.01208)].
- [13] Andrey A. Bagrov, Mikhail Danilov, Sergey Brener, Malte Harland, Alexander I. Lichtenstein, and Mikhail I. Katsnelson. “Detecting quantum critical points in the $t - t'$ Fermi-Hubbard model via complex network theory”. In: *Scientific Reports* 10.1 (2020), p. 20470. DOI: [10.1038/s41598-020-77513-0](https://doi.org/10.1038/s41598-020-77513-0). URL: <https://doi.org/10.1038/s41598-020-77513-0>.
- [14] Z. Bai, J. Demmel, J. Dongarra, A. Ruhe, and H. van der Vorst. *Templates for the Solution of Algebraic Eigenvalue Problems: A Practical Guide*. Society for Industrial and Applied Mathematics, 2000. URL: <https://www.netlib.org/utk/people/JackDongarra/etemplates/book.html>.
- [15] T. Balashov, T. Schuh, A. F. Takács, A. Ernst, S. Ostanin, J. Henk, I. Mertig, P. Bruno, T. Miyamachi, S. Suga, and W. Wulfhekel. “Magnetic Anisotropy and Magnetization Dynamics of Individual Atoms and Clusters of Fe and Co on Pt(111)”. In: *Phys. Rev. Lett.* 102 (25 June 2009), p. 257203. DOI: [10.1103/PhysRevLett.102.257203](https://doi.org/10.1103/PhysRevLett.102.257203). URL: <http://link.aps.org/doi/10.1103/PhysRevLett.102.257203>.
- [16] Matthias Balzer, Nadine Gdaniec, and Michael Potthoff. “Krylov-space approach to the equilibrium and nonequilibrium single-particle Green’s function”. In: *Journal of Physics: Condensed Matter* 24.3 (Dec. 2011), p. 035603. DOI: [10.1088/0953-8984/24/3/035603](https://doi.org/10.1088/0953-8984/24/3/035603). URL: <https://doi.org/10.1088/0953-8984/24/3/035603>.
- [17] J. Bardeen, L. N. Cooper, and J. R. Schrieffer. “Theory of Superconductivity”. In: *Phys. Rev.* 108 (5 Dec. 1957), pp. 1175–1204. DOI: [10.1103/PhysRev.108.1175](https://doi.org/10.1103/PhysRev.108.1175). URL: <https://link.aps.org/doi/10.1103/PhysRev.108.1175>.
- [18] J. G. Bednorz and K. A. Müller. “Possible high T_c superconductivity in the BaLaCuO system”. In: *Zeitschrift für Physik B Condensed Matter* 64.2 (1986), pp. 189–193. DOI: [10.1007/BF01303701](https://doi.org/10.1007/BF01303701). URL: <https://doi.org/10.1007/BF01303701>.

- [19] S. Brener, H. Hafermann, A. N. Rubtsov, M. I. Katsnelson, and A. I. Lichtenstein. “Dual fermion approach to susceptibility of correlated lattice fermions”. In: *Phys. Rev. B* 77 (19 May 2008), p. 195105. DOI: [10.1103/PhysRevB.77.195105](https://doi.org/10.1103/PhysRevB.77.195105). URL: <https://link.aps.org/doi/10.1103/PhysRevB.77.195105>.
- [20] Sergey Brener, Evgeny A. Stepanov, Alexey N. Rubtsov, Mikhail I. Katsnelson, and Alexander I. Lichtenstein. “Dual fermion method as a prototype of generic reference-system approach for correlated fermions”. In: *Annals of Physics* 422 (2020), p. 168310. ISSN: 0003-4916. DOI: <https://doi.org/10.1016/j.aop.2020.168310>. URL: <http://www.sciencedirect.com/science/article/pii/S000349162030244X>.
- [21] Aydin Buluç, Jeremy T. Fineman, Matteo Frigo, John R. Gilbert, and Charles E. Leiserson. “Parallel Sparse Matrix-Vector and Matrix-Transpose-Vector Multiplication Using Compressed Sparse Blocks”. In: *Proceedings of the Twenty-First Annual Symposium on Parallelism in Algorithms and Architectures*. SPAA '09. Calgary, AB, Canada: Association for Computing Machinery, 2009, pp. 233–244. ISBN: 9781605586069. DOI: [10.1145/1583991.1584053](https://doi.org/10.1145/1583991.1584053). URL: <https://doi.org/10.1145/1583991.1584053>.
- [22] P. Chalupa, T. Schäfer, M. Reitner, D. Springer, S. Andergassen, and A. Toschi. “Fingerprints of the Local Moment Formation and its Kondo Screening in the Generalized Susceptibilities of Many-Electron Problems”. In: *Phys. Rev. Lett.* 126 (5 Feb. 2021), p. 056403. DOI: [10.1103/PhysRevLett.126.056403](https://doi.org/10.1103/PhysRevLett.126.056403). URL: <https://link.aps.org/doi/10.1103/PhysRevLett.126.056403>.
- [23] R.T. Clay and S. Mazumdar. “From charge- and spin-ordering to superconductivity in the organic charge-transfer solids”. In: *Physics Reports* 788 (Jan. 2019), pp. 1–89. ISSN: 0370-1573. DOI: [10.1016/j.physrep.2018.10.006](https://doi.org/10.1016/j.physrep.2018.10.006). URL: <http://dx.doi.org/10.1016/j.physrep.2018.10.006>.
- [24] C. Collignon, S. Badoux, S. A. A. Afshar, B. Michon, F. Laliberté, O. Cyr-Choinière, J.-S. Zhou, S. Licciardello, S. Wiedmann, N. Doiron-Leyraud, and Louis Taillefer. “Fermi-surface transformation across the pseudogap critical point of the cuprate superconductor $\text{La}_{1.6-x}\text{Nd}_{0.4}\text{Sr}_x\text{CuO}_4$ ”. In: *Phys. Rev. B* 95 (22 June 2017), p. 224517. DOI: [10.1103/PhysRevB.95.224517](https://doi.org/10.1103/PhysRevB.95.224517). URL: <https://link.aps.org/doi/10.1103/PhysRevB.95.224517>.
- [25] M. Culo, C. Duffy, J. Ayres, M. Berben, Y.-T. Hsu, R. D. H. Hinlopen, B. Bernath, and N. E. Hussey. “Possible superconductivity from incoherent carriers in overdoped cuprates”. In: *SciPost Phys.* 11 (1 2021), p. 12. DOI: [10.21468/SciPostPhys.11.1.012](https://doi.org/10.21468/SciPostPhys.11.1.012). URL: <https://scipost.org/10.21468/SciPostPhys.11.1.012>.

- [26] E. Dagotto, A. Moreo, F. Ortolani, D. Poilblanc, and J. Riera. “Static and dynamical properties of doped Hubbard clusters”. In: *Phys. Rev. B* 45 (18 May 1992), pp. 10741–10760. DOI: [10.1103/PhysRevB.45.10741](https://doi.org/10.1103/PhysRevB.45.10741). URL: <https://link.aps.org/doi/10.1103/PhysRevB.45.10741>.
- [27] E. Dagotto, F. Ortolani, and D. Scalapino. “Single-particle spectral weight of a two-dimensional Hubbard model”. In: *Phys. Rev. B* 46 (5 Aug. 1992), pp. 3183–3186. DOI: [10.1103/PhysRevB.46.3183](https://doi.org/10.1103/PhysRevB.46.3183). URL: <https://link.aps.org/doi/10.1103/PhysRevB.46.3183>.
- [28] Elbio Dagotto. “Correlated electrons in high-temperature superconductors”. In: *Rev. Mod. Phys.* 66 (3 July 1994), pp. 763–840. DOI: [10.1103/RevModPhys.66.763](https://doi.org/10.1103/RevModPhys.66.763). URL: <https://link.aps.org/doi/10.1103/RevModPhys.66.763>.
- [29] Elbio Dagotto, Robert Joynt, Adriana Moreo, Silvia Bacci, and Eduardo Gagliano. “Strongly correlated electronic systems with one hole: Dynamical properties”. In: *Phys. Rev. B* 41 (13 May 1990), pp. 9049–9073. DOI: [10.1103/PhysRevB.41.9049](https://doi.org/10.1103/PhysRevB.41.9049). URL: <https://link.aps.org/doi/10.1103/PhysRevB.41.9049>.
- [30] Andrea Damascelli, Zahid Hussain, and Zhi-Xun Shen. “Angle-resolved photoemission studies of the cuprate superconductors”. In: *Rev. Mod. Phys.* 75 (2 Apr. 2003), pp. 473–541. DOI: [10.1103/RevModPhys.75.473](https://doi.org/10.1103/RevModPhys.75.473). URL: <https://link.aps.org/doi/10.1103/RevModPhys.75.473>.
- [31] M. Danilov, E. G. C. P. van Loon, S. Brener, S. Isakov, M. I. Katsnelson, and A. I. Lichtenstein. *Local Plaquette Physics as Key Ingredient of High-Temperature Superconductivity in Cuprates*. 2021. arXiv: [2107.11344](https://arxiv.org/abs/2107.11344) [[cond-mat.str-el](https://arxiv.org/abs/2107.11344)].
- [32] Martin Dressel and Silvia Tomić. “Molecular quantum materials: electronic phases and charge dynamics in two-dimensional organic solids”. In: *Advances in Physics* 69.1 (2020), pp. 1–120. DOI: [10.1080/00018732.2020.1837833](https://doi.org/10.1080/00018732.2020.1837833). eprint: <https://doi.org/10.1080/00018732.2020.1837833>. URL: <https://doi.org/10.1080/00018732.2020.1837833>.
- [33] N. Dupuis. “A new approach to strongly correlated fermion systems: the spin–particle–hole coherent-state path integral”. In: *Nuclear Physics B* 618.3 (2001), pp. 617–649. ISSN: 0550-3213. DOI: [https://doi.org/10.1016/S0550-3213\(01\)00465-5](https://doi.org/10.1016/S0550-3213(01)00465-5). URL: <http://www.sciencedirect.com/science/article/pii/S0550321301004655>.

- [34] N. Dupuis and S. Pairault. “A STRONG-COUPLING EXPANSION FOR THE Hubbard MODEL”. In: *International Journal of Modern Physics B* 14.24 (2000), pp. 2529–2560. DOI: [10.1142/S0217979200002430](https://doi.org/10.1142/S0217979200002430). eprint: <https://doi.org/10.1142/S0217979200002430>. URL: <https://doi.org/10.1142/S0217979200002430>.
- [35] Andreas Eberlein and Walter Metzner. “Superconductivity in the two-dimensional t - t' -Hubbard model”. In: *Phys. Rev. B* 89 (3 Jan. 2014), p. 035126. DOI: [10.1103/PhysRevB.89.035126](https://doi.org/10.1103/PhysRevB.89.035126). URL: <https://link.aps.org/doi/10.1103/PhysRevB.89.035126>.
- [36] *EDLib: C++ template finite temperature Exact diagonalization solver*. <https://github.com/Q-solvers/EDLib>. URL: <https://github.com/Q-solvers/EDLib>.
- [37] I. Esterlis, S. A. Kivelson, and D. J. Scalapino. “A bound on the superconducting transition temperature”. In: *npj Quantum Materials* 3.1 (2018), p. 59. DOI: [10.1038/s41535-018-0133-0](https://doi.org/10.1038/s41535-018-0133-0). URL: <https://doi.org/10.1038/s41535-018-0133-0>.
- [38] C. Etz, J. Zabloudil, P. Weinberger, and E. Y. Vedmedenko. “Magnetic properties of single atoms of Fe and Co on Ir(111) and Pt(111)”. In: *Phys. Rev. B* 77 (18 May 2008), p. 184425. DOI: [10.1103/PhysRevB.77.184425](https://doi.org/10.1103/PhysRevB.77.184425). URL: <http://link.aps.org/doi/10.1103/PhysRevB.77.184425>.
- [39] Eduardo Fradkin, Steven A. Kivelson, and John M. Tranquada. “Colloquium: Theory of intertwined orders in high temperature superconductors”. In: *Rev. Mod. Phys.* 87 (2 May 2015), pp. 457–482. DOI: [10.1103/RevModPhys.87.457](https://doi.org/10.1103/RevModPhys.87.457). URL: <https://link.aps.org/doi/10.1103/RevModPhys.87.457>.
- [40] A. Gaenko, A.E. Antipov, G. Carcassi, T. Chen, X. Chen, Q. Dong, L. Gamper, J. Gukelberger, R. Igarashi, S. Isakov, M. Könz, J.P.F. LeBlanc, R. Levy, P.N. Ma, J.E. Paki, H. Shinaoka, S. Todo, M. Troyer, and E. Gull. “Updated core libraries of the {ALPS} project”. In: *Computer Physics Communications* (2016), pp. -. ISSN: 0010-4655. DOI: <http://dx.doi.org/10.1016/j.cpc.2016.12.009>. URL: <http://www.sciencedirect.com/science/article/pii/S0010465516303885>.
- [41] P. Gambardella, S. Rusponi, M. Veronese, S. S. Dhesi, C. Grazioli, A. Dallmeyer, I. Cabria, R. Zeller, P. H. Dederichs, K. Kern, C. Carbone, and H. Brune. “Giant Magnetic Anisotropy of Single Cobalt Atoms and Nanoparticles”. In: *Science* 300.5622 (2003), pp. 1130–1133. DOI: [10.1126/science.1082857](https://doi.org/10.1126/science.1082857). eprint: <http://www.sciencemag.org/content/300/5622/1130.full.pdf>. URL: <http://www.sciencemag.org/content/300/5622/1130.abstract>.

- [42] Antoine Georges, Gabriel Kotliar, Werner Krauth, and Marcelo J. Rozenberg. “Dynamical mean-field theory of strongly correlated fermion systems and the limit of infinite dimensions”. In: *Rev. Mod. Phys.* 68 (1 Jan. 1996), pp. 13–125. DOI: [10.1103/RevModPhys.68.13](https://doi.org/10.1103/RevModPhys.68.13). URL: <https://link.aps.org/doi/10.1103/RevModPhys.68.13>.
- [43] F. M. F. de Groot, J. C. Fuggle, B. T. Thole, and G. A. Sawatzky. “ $2p$ x-ray absorption of $3d$ transition-metal compounds: An atomic multiplet description including the crystal field”. In: *Phys. Rev. B* 42 (9 Sept. 1990), pp. 5459–5468. DOI: [10.1103/PhysRevB.42.5459](https://doi.org/10.1103/PhysRevB.42.5459). URL: <http://link.aps.org/doi/10.1103/PhysRevB.42.5459>.
- [44] Claudius Gros and Roser Valentí. “Cluster expansion for the self-energy: A simple many-body method for interpreting the photoemission spectra of correlated Fermi systems”. In: *Phys. Rev. B* 48 (1 July 1993), pp. 418–425. DOI: [10.1103/PhysRevB.48.418](https://doi.org/10.1103/PhysRevB.48.418). URL: <https://link.aps.org/doi/10.1103/PhysRevB.48.418>.
- [45] Jan Gukelberger, Evgeny Kozik, and Hartmut Hafermann. “Diagrammatic Monte Carlo approach for diagrammatic extensions of dynamical mean-field theory: Convergence analysis of the dual fermion technique”. In: *Phys. Rev. B* 96 (3 July 2017), p. 035152. DOI: [10.1103/PhysRevB.96.035152](https://doi.org/10.1103/PhysRevB.96.035152). URL: <https://link.aps.org/doi/10.1103/PhysRevB.96.035152>.
- [46] Emanuel Gull, Andrew J. Millis, Alexander I. Lichtenstein, Alexey N. Rubtsov, Matthias Troyer, and Philipp Werner. “Continuous-time Monte Carlo methods for quantum impurity models”. In: *Rev. Mod. Phys.* 83 (2 May 2011), pp. 349–404. DOI: [10.1103/RevModPhys.83.349](https://doi.org/10.1103/RevModPhys.83.349). URL: <https://link.aps.org/doi/10.1103/RevModPhys.83.349>.
- [47] H. Hafermann. “Numerical Approaches to Spatial Correlations in Strongly Interacting Fermion Systems”. PhD thesis. Universität Hamburg, 2009.
- [48] H. Hafermann, C. Jung, S. Brener, M. I. Katsnelson, A. N. Rubtsov, and A. I. Lichtenstein. “Superperturbation solver for quantum impurity models”. In: *EPL (Europhysics Letters)* 85.2 (Jan. 2009), p. 27007. DOI: [10.1209/0295-5075/85/27007](https://doi.org/10.1209/0295-5075/85/27007). URL: <https://doi.org/10.1209/0295-5075/85/27007>.
- [49] H. Hafermann, G. Li, A. N. Rubtsov, M. I. Katsnelson, A. I. Lichtenstein, and H. Monien. “Efficient Perturbation Theory for Quantum Lattice Models”. In: *Phys. Rev. Lett.* 102 (20 May 2009), p. 206401. DOI: [10.1103/PhysRevLett.102.206401](https://doi.org/10.1103/PhysRevLett.102.206401). URL: <https://link.aps.org/doi/10.1103/PhysRevLett.102.206401>.

- [50] Hartmut Hafermann, Frank Lechermann, Alexey N. Rubtsov, Mikhail I. Katsnelson, Antoine Georges, and Alexander I. Lichtenstein. “Strong electronic correlations: Dynamical Mean-Field Theory and Beyond”. In: *Modern theories of many-particle systems in condensed matter physics*. Ed. by Daniel C Cabra, Andreas Honecker, and Pierre Pujol. Vol. 843. Springer Science & Business Media, 2012. Chap. 4.
- [51] Urs R. Hähner, Sergei Isakov, Hanna Terletska, and Emanuel Gull. “Erratum: Momentum-space cluster dual-fermion method [Phys. Rev. B 97, 125114 (2018)]”. In: *Phys. Rev. B* 100 (16 Oct. 2019), p. 169906. DOI: [10.1103/PhysRevB.100.169906](https://doi.org/10.1103/PhysRevB.100.169906). URL: <https://link.aps.org/doi/10.1103/PhysRevB.100.169906>.
- [52] Malte Harland, Sergey Brener, Mikhail I. Katsnelson, and Alexander I. Lichtenstein. “Exactly solvable model of strongly correlated d -wave superconductivity”. In: *Phys. Rev. B* 101 (4 Jan. 2020), p. 045119. DOI: [10.1103/PhysRevB.101.045119](https://doi.org/10.1103/PhysRevB.101.045119). URL: <https://link.aps.org/doi/10.1103/PhysRevB.101.045119>.
- [53] Malte Harland, Mikhail I. Katsnelson, and Alexander I. Lichtenstein. “Plaquette valence bond theory of high-temperature superconductivity”. In: *Phys. Rev. B* 94 (12 Sept. 2016), p. 125133. DOI: [10.1103/PhysRevB.94.125133](https://doi.org/10.1103/PhysRevB.94.125133). URL: <https://link.aps.org/doi/10.1103/PhysRevB.94.125133>.
- [54] Makoto Hashimoto, Rui-Hua He, Kiyohisa Tanaka, Jean-Pierre Testaud, Worawat Meevasana, Rob G Moore, Donghui Lu, Hong Yao, Yoshiyuki Yoshida, Hiroshi Eisaki, et al. “Particle-hole symmetry breaking in the pseudogap state of Bi2201”. In: *Nature Physics* 6.6 (2010), p. 414.
- [55] Makoto Hashimoto, Elizabeth A Nowadnick, Rui-Hua He, Inna M Vishik, Brian Moritz, Yu He, Kiyohisa Tanaka, Robert G Moore, Donghui Lu, Yoshiyuki Yoshida, et al. “Direct spectroscopic evidence for phase competition between the pseudogap and superconductivity in $\text{Bi}_2\text{Sr}_2\text{CaCu}_2\text{O}_{8+\delta}$ ”. In: *Nature materials* 14.1 (2015), p. 37.
- [56] Patrick Hayden, Matthew Headrick, and Alexander Maloney. “Holographic mutual information is monogamous”. In: *Phys. Rev. D* 87 (4 Feb. 2013), p. 046003. DOI: [10.1103/PhysRevD.87.046003](https://doi.org/10.1103/PhysRevD.87.046003). URL: <https://link.aps.org/doi/10.1103/PhysRevD.87.046003>.
- [57] Alexander Cyril Hewson. *The Kondo Problem to Heavy Fermions*. Cambridge: Cambridge University Press, 1993. DOI: [10.1017/CB09780511470752](https://doi.org/10.1017/CB09780511470752).

- [58] Chisa Hotta. “Theories on Frustrated Electrons in Two-Dimensional Organic Solids”. In: *Crystals* 2.3 (2012), pp. 1155–1200. ISSN: 2073-4352. DOI: [10.3390/cryst2031155](https://doi.org/10.3390/cryst2031155). URL: <https://www.mdpi.com/2073-4352/2/3/1155>.
- [59] J. Hubbard. “Calculation of Partition Functions”. In: *Phys. Rev. Lett.* 3 (2 July 1959), pp. 77–78. DOI: [10.1103/PhysRevLett.3.77](https://doi.org/10.1103/PhysRevLett.3.77). URL: <https://link.aps.org/doi/10.1103/PhysRevLett.3.77>.
- [60] J. Hubbard. “Electron Correlations in Narrow Energy Bands”. In: *Proc. Roy. Soc. A*. Vol. 276. 1365. JSTOR, 1963, pp. 238–257.
- [61] N E Hussey, J Buhot, and S Licciardello. “A tale of two metals: contrasting criticalities in the pnictides and hole-doped cuprates”. In: *Reports on Progress in Physics* 81.5 (Mar. 2018), p. 052501. DOI: [10.1088/1361-6633/aaa97c](https://doi.org/10.1088/1361-6633/aaa97c). URL: <https://doi.org/10.1088/1361-6633/aaa97c>.
- [62] Masatoshi Imada, Atsushi Fujimori, and Yoshinori Tokura. “Metal-insulator transitions”. In: *Rev. Mod. Phys.* 70 (4 Oct. 1998), pp. 1039–1263. DOI: [10.1103/RevModPhys.70.1039](https://doi.org/10.1103/RevModPhys.70.1039). URL: <https://link.aps.org/doi/10.1103/RevModPhys.70.1039>.
- [63] Hiroshi Ishida and Ansgar Liebsch. “Fermi-liquid, non-Fermi-liquid, and Mott phases in iron pnictides and cuprates”. In: *Phys. Rev. B* 81 (5 Feb. 2010), p. 054513. DOI: [10.1103/PhysRevB.81.054513](https://doi.org/10.1103/PhysRevB.81.054513). URL: <http://link.aps.org/doi/10.1103/PhysRevB.81.054513>.
- [64] Sergei Isakov, Andrey E. Antipov, and Emanuel Gull. “Diagrammatic Monte Carlo for dual fermions”. In: *Phys. Rev. B* 94 (3 July 2016), p. 035102. DOI: [10.1103/PhysRevB.94.035102](https://doi.org/10.1103/PhysRevB.94.035102). URL: <https://link.aps.org/doi/10.1103/PhysRevB.94.035102>.
- [65] Sergei Isakov and Michael Danilov. “Exact diagonalization library for quantum electron models”. In: *Computer Physics Communications* 225 (2018), pp. 128–139. ISSN: 0010-4655. DOI: <https://doi.org/10.1016/j.cpc.2017.12.016>. URL: <https://www.sciencedirect.com/science/article/pii/S0010465517304216>.
- [66] Sergei Isakov, Hanna Terletska, and Emanuel Gull. “Momentum-space cluster dual-fermion method”. In: *Phys. Rev. B* 97 (12 Mar. 2018), p. 125114. DOI: [10.1103/PhysRevB.97.125114](https://doi.org/10.1103/PhysRevB.97.125114). URL: <https://link.aps.org/doi/10.1103/PhysRevB.97.125114>.

- [67] Hong-Chen Jiang and Thomas P. Devereaux. “Superconductivity in the doped Hubbard model and its interplay with next-nearest hopping t' ”. In: *Science* 365.6460 (2019), pp. 1424–1428. ISSN: 0036-8075. DOI: [10.1126/science.aal5304](https://doi.org/10.1126/science.aal5304). eprint: <https://science.sciencemag.org/content/365/6460/1424.full.pdf>. URL: <https://science.sciencemag.org/content/365/6460/1424>.
- [68] Marcus Kaiser. “Mean clustering coefficients: the role of isolated nodes and leafs on clustering measures for small-world networks”. In: *New Journal of Physics* 10.8 (Aug. 2008), p. 083042. DOI: [10.1088/1367-2630/10/8/083042](https://doi.org/10.1088/1367-2630/10/8/083042). URL: <https://doi.org/10.1088/1367-2630/10/8/083042>.
- [69] Kazushi Kanoda. “Metal–Insulator Transition in κ -(ET)₂X and (DCNQI)₂M: Two Contrasting Manifestation of Electron Correlation”. In: *Journal of the Physical Society of Japan* 75.5 (2006), p. 051007. DOI: [10.1143/JPSJ.75.051007](https://doi.org/10.1143/JPSJ.75.051007). eprint: <https://doi.org/10.1143/JPSJ.75.051007>. URL: <https://doi.org/10.1143/JPSJ.75.051007>.
- [70] B. Keimer, S. A. Kivelson, M. R. Norman, S. Uchida, and J. Zaanen. “From quantum matter to high-temperature superconductivity in copper oxides”. In: *Nature* 518.7538 (2015), pp. 179–186. DOI: [10.1038/nature14165](https://doi.org/10.1038/nature14165). URL: <https://doi.org/10.1038/nature14165>.
- [71] Takeshi Kondo, Rustem Khasanov, Tsunehiro Takeuchi, Jörg Schmalian, and Adam Kaminski. “Competition between the pseudogap and superconductivity in the high- T_c copper oxides”. In: *Nature* 457.7227 (2009), p. 296.
- [72] G. Kotliar, S. Y. Savrasov, K. Haule, V. S. Oudovenko, O. Parcollet, and C. A. Marianetti. “Electronic structure calculations with dynamical mean-field theory”. In: *Rev. Mod. Phys.* 78 (3 Aug. 2006), pp. 865–951. DOI: [10.1103/RevModPhys.78.865](https://doi.org/10.1103/RevModPhys.78.865). URL: <https://link.aps.org/doi/10.1103/RevModPhys.78.865>.
- [73] Evgeny Kozik, Michel Ferrero, and Antoine Georges. “Nonexistence of the Luttinger-Ward Functional and Misleading Convergence of Skeleton Diagrammatic Series for Hubbard-Like Models”. In: *Phys. Rev. Lett.* 114 (15 Apr. 2015), p. 156402. DOI: [10.1103/PhysRevLett.114.156402](https://doi.org/10.1103/PhysRevLett.114.156402). URL: <https://link.aps.org/doi/10.1103/PhysRevLett.114.156402>.
- [74] Friedrich Krien, Erik G. C. P. van Loon, Mikhail I. Katsnelson, Alexander I. Lichtenstein, and Massimo Capone. “Two-particle Fermi liquid parameters at the Mott transition: Vertex divergences, Landau parameters, and incoherent response in dynamical mean-field theory”. In: *Phys. Rev. B* 99 (24 June 2019), p. 245128. DOI: [10.1103/PhysRevB.99.245128](https://doi.org/10.1103/PhysRevB.99.245128). URL: <https://link.aps.org/doi/10.1103/PhysRevB.99.245128>.

- [75] Friedrich Krien, Angelo Valli, Patrick Chalupa, Massimo Capone, Alexander I. Lichtenstein, and Alessandro Toschi. “Boson-exchange parquet solver for dual fermions”. In: *Phys. Rev. B* 102 (19 Nov. 2020), p. 195131. DOI: [10.1103/PhysRevB.102.195131](https://doi.org/10.1103/PhysRevB.102.195131). URL: <https://link.aps.org/doi/10.1103/PhysRevB.102.195131>.
- [76] I. S. Krivenko, A. N. Rubtsov, M. I. Katsnelson, and A. I. Lichtenstein. “Analytical approximation for single-impurity Anderson model”. In: *JETP Letters* 91.6 (2010), pp. 319–325. DOI: [10.1134/S0021364010060123](https://doi.org/10.1134/S0021364010060123). URL: <https://doi.org/10.1134/S0021364010060123>.
- [77] R. Lehoucq, D. Sorensen, and C. Yang. *ARPACK Users’ Guide*. Society for Industrial and Applied Mathematics, 1998. DOI: [10.1137/1.9780898719628](https://doi.org/10.1137/1.9780898719628). eprint: <http://epubs.siam.org/doi/pdf/10.1137/1.9780898719628>. URL: <http://epubs.siam.org/doi/abs/10.1137/1.9780898719628>.
- [78] A. I. Lichtenstein and M. I. Katsnelson. “Antiferromagnetism and d-wave superconductivity in cuprates: A cluster dynamical mean-field theory”. In: *Phys. Rev. B* 62 (14 Oct. 2000), R9283–R9286. DOI: [10.1103/PhysRevB.62.R9283](https://doi.org/10.1103/PhysRevB.62.R9283). URL: <https://link.aps.org/doi/10.1103/PhysRevB.62.R9283>.
- [79] Elliott H. Lieb and F. Y. Wu. “Absence of Mott Transition in an Exact Solution of the Short-Range, One-Band Model in One Dimension”. In: *Phys. Rev. Lett.* 20 (25 June 1968), pp. 1445–1448. DOI: [10.1103/PhysRevLett.20.1445](https://doi.org/10.1103/PhysRevLett.20.1445). URL: <https://link.aps.org/doi/10.1103/PhysRevLett.20.1445>.
- [80] W. Lipski. Mir, 1988.
- [81] Erik G C P van Loon. “Second-order dual fermion for multi-orbital systems”. In: *Journal of Physics: Condensed Matter* 33.13 (Jan. 2021), p. 135601. DOI: [10.1088/1361-648x/abd9ed](https://doi.org/10.1088/1361-648x/abd9ed). URL: <https://doi.org/10.1088/1361-648x/abd9ed>.
- [82] Erik G. C. P. van Loon, Friedrich Krien, and Andrey A. Katanin. “Bethe-Salpeter Equation at the Critical End Point of the Mott Transition”. In: *Phys. Rev. Lett.* 125 (13 Sept. 2020), p. 136402. DOI: [10.1103/PhysRevLett.125.136402](https://doi.org/10.1103/PhysRevLett.125.136402). URL: <https://link.aps.org/doi/10.1103/PhysRevLett.125.136402>.
- [83] G.D. Mahan. *Many-Particle Physics, third edition*. New York, NY: Springer, 2000.

- [84] T. A. Maier, M. Jarrell, T. C. Schulthess, P. R. C. Kent, and J. B. White. “Systematic Study of d -Wave Superconductivity in the 2D Repulsive Hubbard Model”. In: *Phys. Rev. Lett.* 95 (23 Nov. 2005), p. 237001. DOI: [10.1103/PhysRevLett.95.237001](https://doi.org/10.1103/PhysRevLett.95.237001). URL: <https://link.aps.org/doi/10.1103/PhysRevLett.95.237001>.
- [85] T. A. Maier, M. S. Jarrell, and D. J. Scalapino. “Structure of the Pairing Interaction in the Two-Dimensional Hubbard Model”. In: *Phys. Rev. Lett.* 96 (4 Feb. 2006), p. 047005. DOI: [10.1103/PhysRevLett.96.047005](https://doi.org/10.1103/PhysRevLett.96.047005). URL: <https://link.aps.org/doi/10.1103/PhysRevLett.96.047005>.
- [86] Th. Maier, M. Jarrell, Th. Pruschke, and J. Keller. “ d -Wave Superconductivity in the Hubbard Model”. In: *Phys. Rev. Lett.* 85 (7 Aug. 2000), pp. 1524–1527. DOI: [10.1103/PhysRevLett.85.1524](https://doi.org/10.1103/PhysRevLett.85.1524). URL: <https://link.aps.org/doi/10.1103/PhysRevLett.85.1524>.
- [87] K. J. Maschhoff and D. C. Sorensen. “P_ARPACK: An efficient portable large scale eigenvalue package for distributed memory parallel architectures”. In: *Applied Parallel Computing Industrial Computation and Optimization*. Ed. by Jerzy Waśniewski, Jack Dongarra, Kaj Madsen, and Dorte Olesen. Berlin, Heidelberg: Springer Berlin Heidelberg, 1996, pp. 478–486. ISBN: 978-3-540-49643-4.
- [88] V. V. Mazurenko, S. N. Isakov, A. N. Rudenko, V. I. Anisimov, and A. I. Lichtenstein. “Renormalized spectral function for Co adatom on the Pt(111) surface”. In: *Phys. Rev. B* 82 (19 Nov. 2010), p. 193403. DOI: [10.1103/PhysRevB.82.193403](https://doi.org/10.1103/PhysRevB.82.193403). URL: <http://link.aps.org/doi/10.1103/PhysRevB.82.193403>.
- [89] V. V. Mazurenko, A. I. Lichtenstein, M. I. Katsnelson, I. Dasgupta, T. Saha-Dasgupta, and V. I. Anisimov. “Nature of insulating state in NaV_2O_5 above charge-ordering transition: A cluster dynamical mean-field study”. In: *Phys. Rev. B* 66 (8 Aug. 2002), p. 081104. DOI: [10.1103/PhysRevB.66.081104](https://doi.org/10.1103/PhysRevB.66.081104). URL: <http://link.aps.org/doi/10.1103/PhysRevB.66.081104>.
- [90] Darya Medvedeva, Sergei Isakov, Friedrich Krien, Vladimir V. Mazurenko, and Alexander I. Lichtenstein. “Exact diagonalization solver for extended dynamical mean-field theory”. In: *Phys. Rev. B* 96 (23 Dec. 2017), p. 235149. DOI: [10.1103/PhysRevB.96.235149](https://doi.org/10.1103/PhysRevB.96.235149). URL: <https://link.aps.org/doi/10.1103/PhysRevB.96.235149>.
- [91] Focko Karl Meier. “Co on Pt(111) studied by spin-polarized scanning tunneling microscopy and spectroscopy”. PhD thesis. Fachbereich Physik der Universität Hamburg, 2006.

- [92] Corey Melnick and Gabriel Kotliar. “Fermi-liquid theory and divergences of the two-particle irreducible vertex in the periodic Anderson lattice”. In: *Phys. Rev. B* 101 (16 Apr. 2020), p. 165105. DOI: [10.1103/PhysRevB.101.165105](https://doi.org/10.1103/PhysRevB.101.165105). URL: <https://link.aps.org/doi/10.1103/PhysRevB.101.165105>.
- [93] J. Merino and O. Gunnarsson. “Pseudogap and singlet formation in organic and cuprate superconductors”. In: *Phys. Rev. B* 89 (24 June 2014), p. 245130. DOI: [10.1103/PhysRevB.89.245130](https://doi.org/10.1103/PhysRevB.89.245130). URL: <https://link.aps.org/doi/10.1103/PhysRevB.89.245130>.
- [94] Walter Metzner and Dieter Vollhardt. “Correlated Lattice Fermions in $d = \infty$ Dimensions”. In: *Phys. Rev. Lett.* 62 (3 Jan. 1989), pp. 324–327. DOI: [10.1103/PhysRevLett.62.324](https://doi.org/10.1103/PhysRevLett.62.324). URL: <https://link.aps.org/doi/10.1103/PhysRevLett.62.324>.
- [95] Pierre Monceau. “Electronic crystals: an experimental overview”. In: *Advances in Physics* 61.4 (2012), pp. 325–581. DOI: [10.1080/00018732.2012.719674](https://doi.org/10.1080/00018732.2012.719674). eprint: <https://doi.org/10.1080/00018732.2012.719674>. URL: <https://doi.org/10.1080/00018732.2012.719674>.
- [96] Toru Moriya. *Spin Fluctuations in Itinerant Electron Magnetism*. New York: Springer Verlag, 1985.
- [97] Alexander F. Otte, Markus Ternes, Kirsten von Bergmann, Sebastian Loth, Harald Brune, Christopher P. Lutz, Cyrus F. Hirjibehedin, and Andreas J. Heinrich. “The role of magnetic anisotropy in the Kondo effect”. In: *Nature Physics* 4.11 (2008), p. 847.
- [98] Taisuke Ozaki. “Continued fraction representation of the Fermi-Dirac function for large-scale electronic structure calculations”. In: *Phys. Rev. B* 75 (3 Jan. 2007), p. 035123. DOI: [10.1103/PhysRevB.75.035123](https://doi.org/10.1103/PhysRevB.75.035123). URL: <https://link.aps.org/doi/10.1103/PhysRevB.75.035123>.
- [99] Stéphane Pairault, David Sénéchal, and A.-M. S. Tremblay. “Strong-Coupling Expansion for the Hubbard Model”. In: *Phys. Rev. Lett.* 80 (24 June 1998), pp. 5389–5392. DOI: [10.1103/PhysRevLett.80.5389](https://doi.org/10.1103/PhysRevLett.80.5389). URL: <https://link.aps.org/doi/10.1103/PhysRevLett.80.5389>.
- [100] Pairault, S., Sénéchal, D., and A.-M.S. Tremblay. “Strong-coupling perturbation theory of the Hubbard model”. In: *Eur. Phys. J. B* 16.1 (2000), pp. 85–105. DOI: [10.1007/s100510070253](https://doi.org/10.1007/s100510070253). URL: <https://doi.org/10.1007/s100510070253>.

- [101] E. Pavarini, I. Dasgupta, T. Saha-Dasgupta, O. Jepsen, and O. K. Andersen. “Band-Structure Trend in Hole-Doped Cuprates and Correlation with T_{cmax} ”. In: *Phys. Rev. Lett.* 87 (4 July 2001), p. 047003. DOI: [10.1103/PhysRevLett.87.047003](https://doi.org/10.1103/PhysRevLett.87.047003). URL: <https://link.aps.org/doi/10.1103/PhysRevLett.87.047003>.
- [102] Cyril Proust and Louis Taillefer. “The Remarkable Underlying Ground States of Cuprate Superconductors”. In: *Annual Review of Condensed Matter Physics* 10.1 (2019), pp. 409–429. DOI: [10.1146/annurev-conmatphys-031218-013210](https://doi.org/10.1146/annurev-conmatphys-031218-013210). eprint: <https://doi.org/10.1146/annurev-conmatphys-031218-013210>. URL: <https://doi.org/10.1146/annurev-conmatphys-031218-013210>.
- [103] *Q-solvers quantum solver development group*. <https://github.com/Q-solvers>. URL: <https://github.com/Q-solvers>.
- [104] Mingpu Qin, Chia-Min Chung, Hao Shi, Ettore Vitali, Claudius Hubig, Ulrich Schollwöck, Steven R. White, and Shiwei Zhang. “Absence of Superconductivity in the Pure Two-Dimensional Hubbard Model”. In: *Phys. Rev. X* 10 (3 July 2020), p. 031016. DOI: [10.1103/PhysRevX.10.031016](https://doi.org/10.1103/PhysRevX.10.031016). URL: <https://link.aps.org/doi/10.1103/PhysRevX.10.031016>.
- [105] M. Reitner, P. Chalupa, L. Del Re, D. Springer, S. Ciuchi, G. Sangiovanni, and A. Toschi. “Attractive Effect of a Strong Electronic Repulsion: The Physics of Vertex Divergences”. In: *Phys. Rev. Lett.* 125 (19 Nov. 2020), p. 196403. DOI: [10.1103/PhysRevLett.125.196403](https://doi.org/10.1103/PhysRevLett.125.196403). URL: <https://link.aps.org/doi/10.1103/PhysRevLett.125.196403>.
- [106] G. Rohringer, H. Hafermann, A. Toschi, A. A. Katanin, A. E. Antipov, M. I. Katsnelson, A. I. Lichtenstein, A. N. Rubtsov, and K. Held. “Diagrammatic routes to nonlocal correlations beyond dynamical mean field theory”. In: *Rev. Mod. Phys.* 90 (2 May 2018), p. 025003. DOI: [10.1103/RevModPhys.90.025003](https://doi.org/10.1103/RevModPhys.90.025003). URL: <https://link.aps.org/doi/10.1103/RevModPhys.90.025003>.
- [107] G. Rohringer, A. Valli, and A. Toschi. “Local electronic correlation at the two-particle level”. In: *Phys. Rev. B* 86 (12 Sept. 2012), p. 125114. DOI: [10.1103/PhysRevB.86.125114](https://doi.org/10.1103/PhysRevB.86.125114). URL: <https://link.aps.org/doi/10.1103/PhysRevB.86.125114>.
- [108] A. N. Rubtsov, M. I. Katsnelson, and A. I. Lichtenstein. “Dual fermion approach to nonlocal correlations in the Hubbard model”. In: *Phys. Rev. B* 77 (3 Jan. 2008), p. 033101. DOI: [10.1103/PhysRevB.77.033101](https://doi.org/10.1103/PhysRevB.77.033101). URL: [http://link.aps.org/doi/10.1103/PhysRevB.77.033101](https://link.aps.org/doi/10.1103/PhysRevB.77.033101).

- [109] Y. Saad. *Numerical Methods for Large Eigenvalue Problems: Revised Edition*. Classics in Applied Mathematics. Society for Industrial and Applied Mathematics, 2011. ISBN: 9781611970739. URL: <https://books.google.de/books?id=gViDLbUDjZ8C>.
- [110] Shiro Sakai, Marcello Civelli, and Masatoshi Imada. “Hidden Fermionic Excitation Boosting High-Temperature Superconductivity in Cuprates”. In: *Phys. Rev. Lett.* 116 (5 Feb. 2016), p. 057003. DOI: [10.1103/PhysRevLett.116.057003](https://doi.org/10.1103/PhysRevLett.116.057003). URL: <https://link.aps.org/doi/10.1103/PhysRevLett.116.057003>.
- [111] Shiro Sakai, Marcello Civelli, and Masatoshi Imada. “Hidden-fermion representation of self-energy in pseudogap and superconducting states of the two-dimensional Hubbard model”. In: *Phys. Rev. B* 94 (11 Sept. 2016), p. 115130. DOI: [10.1103/PhysRevB.94.115130](https://doi.org/10.1103/PhysRevB.94.115130). URL: <https://link.aps.org/doi/10.1103/PhysRevB.94.115130>.
- [112] S K Sarker. “A new functional integral formalism for strongly correlated Fermi systems”. In: *Journal of Physics C: Solid State Physics* 21.18 (June 1988), pp. L667–L672. DOI: [10.1088/0022-3719/21/18/002](https://doi.org/10.1088/0022-3719/21/18/002). URL: <https://doi.org/10.1088/0022-3719/21/18/002>.
- [113] Y. Sato, S. Kasahara, H. Murayama, Y. Kasahara, E.-G. Moon, T. Nishizaki, T. Loew, J. Porras, B. Keimer, T. Shibauchi, and Y. Matsuda. “Thermodynamic evidence for a nematic phase transition at the onset of the pseudogap in YBa₂Cu₃O_y”. In: *Nature Physics* 13.11 (Nov. 2017), pp. 1074–1078. ISSN: 1745-2481. DOI: [10.1038/nphys4205](https://doi.org/10.1038/nphys4205). URL: <https://doi.org/10.1038/nphys4205>.
- [114] D. J. Scalapino. “A common thread: The pairing interaction for unconventional superconductors”. In: *Rev. Mod. Phys.* 84 (4 Oct. 2012), pp. 1383–1417. DOI: [10.1103/RevModPhys.84.1383](https://doi.org/10.1103/RevModPhys.84.1383). URL: <https://link.aps.org/doi/10.1103/RevModPhys.84.1383>.
- [115] T. Schäfer, G. Rohringer, O. Gunnarsson, S. Ciuchi, G. Sangiovanni, and A. Toschi. “Divergent Precursors of the Mott-Hubbard Transition at the Two-Particle Level”. In: *Phys. Rev. Lett.* 110 (24 June 2013), p. 246405. DOI: [10.1103/PhysRevLett.110.246405](https://doi.org/10.1103/PhysRevLett.110.246405). URL: <http://link.aps.org/doi/10.1103/PhysRevLett.110.246405>.
- [116] David Sénéchal and A.-M. S. Tremblay. “Hot Spots and Pseudogaps for Hole- and Electron-Doped High-Temperature Superconductors”. In: *Phys. Rev. Lett.* 92 (12 Mar. 2004), p. 126401. DOI: [10.1103/PhysRevLett.92.126401](https://doi.org/10.1103/PhysRevLett.92.126401). URL: <https://link.aps.org/doi/10.1103/PhysRevLett.92.126401>.

- [117] J.C. Slater. *Quantum Theory of Atomic Structure, 1st edition*. McGraw Hill, 1960.
- [118] Jonathan A. Sobota, Yu He, and Zhi-Xun Shen. “Angle-resolved photoemission studies of quantum materials”. In: *Rev. Mod. Phys.* 93 (2 May 2021), p. 025006. DOI: [10.1103/RevModPhys.93.025006](https://doi.org/10.1103/RevModPhys.93.025006). URL: <https://link.aps.org/doi/10.1103/RevModPhys.93.025006>.
- [119] D. Springer, P. Chalupa, S. Ciuchi, G. Sangiovanni, and A. Toschi. “Interplay between local response and vertex divergences in many-fermion systems with on-site attraction”. In: *Phys. Rev. B* 101 (15 Apr. 2020), p. 155148. DOI: [10.1103/PhysRevB.101.155148](https://doi.org/10.1103/PhysRevB.101.155148). URL: <https://link.aps.org/doi/10.1103/PhysRevB.101.155148>.
- [120] R. L. Stratonovich. “On a method of calculating quantum distribution functions”. In: *Soviet Physics Doklady*. Vol. 2. 1957, p. 416.
- [121] Ping Sun and Gabriel Kotliar. “Extended dynamical mean-field theory and GW method”. In: *Phys. Rev. B* 66 (8 Aug. 2002), p. 085120. DOI: [10.1103/PhysRevB.66.085120](https://doi.org/10.1103/PhysRevB.66.085120). URL: <https://link.aps.org/doi/10.1103/PhysRevB.66.085120>.
- [122] Bhuvanesh Sundar, Marc Andrew Valdez, Lincoln D. Carr, and Kaden R. A. Hazzard. “Complex-network description of thermal quantum states in the Ising spin chain”. In: *Phys. Rev. A* 97 (5 May 2018), p. 052320. DOI: [10.1103/PhysRevA.97.052320](https://doi.org/10.1103/PhysRevA.97.052320). URL: <https://link.aps.org/doi/10.1103/PhysRevA.97.052320>.
- [123] Toshihiro Takahashi, Yoshio Nogami, and Kyuya Yakushi. “Charge Ordering in Organic Conductors”. In: *Journal of the Physical Society of Japan* 75.5 (2006), p. 051008. DOI: [10.1143/JPSJ.75.051008](https://doi.org/10.1143/JPSJ.75.051008). eprint: <https://doi.org/10.1143/JPSJ.75.051008>. URL: <https://doi.org/10.1143/JPSJ.75.051008>.
- [124] Nayuta Takemori, Akihisa Koga, and Hartmut Hafermann. *Intersite electron correlations on inhomogeneous lattices: a real-space dual fermion approach*. 2018. arXiv: [1801.02441](https://arxiv.org/abs/1801.02441) [[cond-mat.str-el](https://arxiv.org/abs/1801.02441)].
- [125] J. M. Tranquada, B. J. Sternlieb, J. D. Axe, Y. Nakamura, and S. Uchida. “Evidence for stripe correlations of spins and holes in copper oxide superconductors”. In: *Nature* 375.6532 (June 1995), pp. 561–563. ISSN: 1476-4687. DOI: [10.1038/375561a0](https://doi.org/10.1038/375561a0). URL: <https://doi.org/10.1038/375561a0>.

- [126] Wei-Feng Tsai, Hong Yao, Andreas Läuchli, and Steven A. Kivelson. “Optimal inhomogeneity for superconductivity: Finite-size studies”. In: *Phys. Rev. B* 77 (21 June 2008), p. 214502. DOI: [10.1103/PhysRevB.77.214502](https://doi.org/10.1103/PhysRevB.77.214502). URL: <https://link.aps.org/doi/10.1103/PhysRevB.77.214502>.
- [127] Marc Andrew Valdez, Daniel Jaschke, David L. Vargas, and Lincoln D. Carr. “Quantifying Complexity in Quantum Phase Transitions via Mutual Information Complex Networks”. In: *Phys. Rev. Lett.* 119 (22 Nov. 2017), p. 225301. DOI: [10.1103/PhysRevLett.119.225301](https://doi.org/10.1103/PhysRevLett.119.225301). URL: <https://link.aps.org/doi/10.1103/PhysRevLett.119.225301>.
- [128] M. Vandelli, V. Harkov, E. A. Stepanov, J. Gukelberger, E. Kozik, A. Rubio, and A. I. Lichtenstein. “Dual boson diagrammatic Monte Carlo approach applied to the extended Hubbard model”. In: *Phys. Rev. B* 102 (19 Nov. 2020), p. 195109. DOI: [10.1103/PhysRevB.102.195109](https://doi.org/10.1103/PhysRevB.102.195109). URL: <https://link.aps.org/doi/10.1103/PhysRevB.102.195109>.
- [129] Gideon Wachtel, Shirit Baruch, and Dror Orgad. “Optimal inhomogeneity for pairing in Hubbard systems with next-nearest-neighbor hopping”. In: *Phys. Rev. B* 96 (6 Aug. 2017), p. 064527. DOI: [10.1103/PhysRevB.96.064527](https://doi.org/10.1103/PhysRevB.96.064527). URL: <https://link.aps.org/doi/10.1103/PhysRevB.96.064527>.
- [130] C. Walsh, P. Sémon, D. Poulin, G. Sordi, and A.-M. S. Tremblay. “Local Entanglement Entropy and Mutual Information across the Mott Transition in the Two-Dimensional Hubbard Model”. In: *Phys. Rev. Lett.* 122 (6 Feb. 2019), p. 067203. DOI: [10.1103/PhysRevLett.122.067203](https://doi.org/10.1103/PhysRevLett.122.067203). URL: <https://link.aps.org/doi/10.1103/PhysRevLett.122.067203>.
- [131] C. Walsh, P. Sémon, G. Sordi, and A.-M. S. Tremblay. “Critical opalescence across the doping-driven Mott transition in optical lattices of ultracold atoms”. In: *Phys. Rev. B* 99 (16 Apr. 2019), p. 165151. DOI: [10.1103/PhysRevB.99.165151](https://doi.org/10.1103/PhysRevB.99.165151). URL: <https://link.aps.org/doi/10.1103/PhysRevB.99.165151>.
- [132] Wei Wu, Michel Ferrero, Antoine Georges, and Evgeny Kozik. “Controlling Feynman diagrammatic expansions: Physical nature of the pseudogap in the two-dimensional Hubbard model”. In: *Phys. Rev. B* 96 (4 July 2017), p. 041105. DOI: [10.1103/PhysRevB.96.041105](https://doi.org/10.1103/PhysRevB.96.041105). URL: <https://link.aps.org/doi/10.1103/PhysRevB.96.041105>.
- [133] Susumu Yamada, Toshiyuki Imamura, and Masahiko Machida. “16.14 TFLOPS Eigenvalue Solver on the Earth Simulator: Exact Diagonalization for Ultra Largescale Hamiltonian Matrix”. In: *High-Performance Computing*. Ed. by Jesús Labarta, Kazuki Joe, and Toshinori Sato. Berlin, Heidelberg: Springer Berlin Heidelberg, 2008, pp. 402–413. ISBN: 978-3-540-77704-5.

- [134] Susumu Yamada, Toshiyuki Imamura, and Masahiko Machida. “16.447 TFlops and 159-Billion-Dimensional Exact-Diagonalization for Trapped Fermion-Hubbard Model on the Earth Simulator”. In: *Proceedings of the 2005 ACM/IEEE Conference on Supercomputing*. SC '05. USA: IEEE Computer Society, 2005, p. 44. ISBN: 1595930612. DOI: [10.1109/SC.2005.1](https://doi.org/10.1109/SC.2005.1). URL: <https://doi.org/10.1109/SC.2005.1>.
- [135] Shuhui Yang, Tao Ying, Weiqi Li, Jianqun Yang, Xiudong Sun, and Xingji Li. “Quantum Monte Carlo study of the Hubbard model with next-nearest-neighbor hopping t' : pairing and magnetism”. In: *Journal of Physics: Condensed Matter* 33.11 (Dec. 2020), p. 115601. DOI: [10.1088/1361-648x/abd33a](https://doi.org/10.1088/1361-648x/abd33a). URL: <https://doi.org/10.1088/1361-648x/abd33a>.
- [136] R Žitko and Th Pruschke. “Many-particle effects in adsorbed magnetic atoms with easy-axis anisotropy: the case of Fe on the CuN/Cu(100) surface”. In: *New Journal of Physics* 12.6 (2010), p. 063040. URL: <http://stacks.iop.org/1367-2630/12/i=6/a=063040>.

List of Publications

Refereed publications

1. Andrey A. Bagrov, Mikhail Danilov, Sergey Brener, Malte Harland, Alexander I. Lichtenstein, and Mikhail I. Katsnelson. “Detecting quantum critical points in the $t - t'$ Fermi-Hubbard model via complex network theory”. In: *Scientific Reports* 10.1 (2020), p. 20470. DOI: [10.1038/s41598-020-77513-0](https://doi.org/10.1038/s41598-020-77513-0). URL: <https://doi.org/10.1038/s41598-020-77513-0>
2. Sergei Isakov and Michael Danilov. “Exact diagonalization library for quantum electron models”. In: *Computer Physics Communications* 225 (2018), pp. 128–139. ISSN: 0010-4655. DOI: <https://doi.org/10.1016/j.cpc.2017.12.016>. URL: <https://www.sciencedirect.com/science/article/pii/S0010465517304216>

Publications in preparation

1. M. Danilov, E. G. C. P. van Loon, S. Brener, S. Isakov, M. I. Katsnelson, and A. I. Lichtenstein. *Local Plaquette Physics as Key Ingredient of High-Temperature Superconductivity in Cuprates*. 2021. arXiv: [2107.11344](https://arxiv.org/abs/2107.11344) [[cond-mat.str-el](https://arxiv.org/abs/2107.11344)]

Conference contributions

1. M. Danilov, S. Isakov, M. Harland, A. Bagrov, A. Lichtenstein. Exact Diagonalization study of large Hubbard clusters. Kourovka-XXXVII international winter theoretical physics school, Yekaterinburg, Russia
2. M. Danilov, S. Isakov, S. Brener, M. Harland, A. Lichtenstein. Exact Diagonalization study of large Hubbard clusters. DPG Spring Meeting, Dresden, Germany
3. M.U. Danilov, S.N. Isakov. Solution of multi-site Hubbard model for V_{15} molecular magnet. Kourovka-XXXVI international winter theoretical physics school, Yekaterinburg, Russia

Eidesstattliche Versicherung / Declaration on oath

Hiermit versichere ich an Eides statt, die vorliegende Dissertationsschrift selbst verfasst und keine anderen als die angegebenen Hilfsmittel und Quellen benutzt zu haben.

Hamburg, den 29.07.2021

Unterschrift der Doktorandin / des Doktoranden

Acknowledgments

I would like to thank everyone who supported me during my work at the 1st Institute of Theoretical Physics.

First, I would like to thank my supervisor Prof. Dr. Alexander Lichtenstein and my second supervisor Prof. Dr. Michael Potthoff, for giving me the opportunity to work on such important and computationally challenging area of physics and for the helpful discussions and continuous encouragement throughout the study.

I would like to express my appreciation for the help with understanding programming and physics matters to my former Master's degree supervisor Dr. Sergei Isakov and our postdoctoral researchers Dr. Igor Krivenko and Dr. Sergey Brener.

I am profoudly thankful to Prof. Dr. Mikhail I. Katsnelson, Prof. Dr. Andrei Bagrov and Prof. Dr. Erik G. C. P. van Loon for fruitful collaboration in the investigation of properties of the 2×2 and 4×4 Hubbard clusters.

I acknowledge the kind help of the PHYSnet administrators Michael Vedmedenko, Bodo Krause-Kyora, the staff of European XFEL and DESY User Consulting Office in all computer-related questions and thank them for providing the computing resources necessary to run the hundreds of compute jobs that were crucial for this research. I am also thankful to the secretaries Sigrid Schmidtke and Gunda Sen for their organizational support.

I am very grateful to all members of our group: Yusuf Mohammed, Patryk Kubiczek, Igor Krivenko, Viktor Valmispild, Malte Harland, Daniel Hirschmeier, Viktor Harkov, Andrej Lehmann, Roberto Mozara, Arthur Huber, Sergey Brener, Friedrich Krien, Oleg Kristanovski, Aleksandr Propst, Matteo Vandelli, Maria Bandelmann, Evgeny Stepanov, who have always been available for discussions about all topics ranging from work-related to informal.

I thank mental health professionals Dr. Kristin Müller-Popkes, the staff of Universitätsklinikum Hamburg and other organizations that treated me, for helping me trust my mind again.

The work on this thesis would have been impossible without my family. I wish to thank my mum Irina M. Danilova and my aunt Marina M. Danilova for supporting me throughout my life and always being there to talk, and my late grandparents Michael B. Danilov and Zoe P. Danilova for sparking my interest in science and technology.